Experimental studies of a degenerate unitary Bose gas

by

Philip Makotyn

B.A., Elmhurst College, 2006

B.S., University of Illinois at Urbana-Champaign, 2006

A thesis submitted to the

Faculty of the Graduate School of the

University of Colorado in partial fulfillment

of the requirements for the degree of

Doctor of Philosophy

Department of Physics

2014

This thesis entitled:
Experimental studies of a degenerate unitary Bose gas
written by Philip Makotyn
has been approved for the Department of Physics

Dr. Deborah S. Jin

Dr. Eric A. Cornell

Date

The final copy of this thesis has been examined by the signatories, and we find that both the content and the form meet acceptable presentation standards of scholarly work in the above mentioned discipline.

Makotyn, Philip (Ph.D., Physics)

Experimental studies of a degenerate unitary Bose gas

Thesis directed by Dr. Deborah S. Jin

A dilute Bose-Einstein condensate (BEC) near a Feshbach resonance provides experimental physics with a clean and controllable system to investigate strongly interacting many-body systems. The ability to tune the scattering length allows BECs to be projected onto strong interactions from an initial weakly interacting state. However, historically, studying a bulk 3D strongly interacting BEC has been difficult, as these systems are inherently unstable due to three-body inelastic collisions. Thus, 2D, 1D, lattice confined, and two component Fermi gases were used to explore the strong interactions in an ultracold gas. In this thesis, I present the first measurement of a strongly interacting 3D ^{85}Rb BEC. I introduce our experimental system and the techniques we used to probe the BEC. I first report on probes of a BEC in the weakly interacting regime. To probe a spherical ^{85}Rb BEC with strong interactions we implemented a novel experimental technique that allowed us to quickly change the interactions, bypassing inelastic losses. We projected the BEC onto unitarity, where the scattering length diverges and the interactions are infinite, in order to observe dynamics and the unexpectedly long lifetime of the gas. Additionally, we observe a universality of the gas with respect to the length scale set by the interparticle spacing.

Dedication

To my grandmother, babcia

Acknowledgements

Working at JILA these past years has been an incredible delight. The fast pace of research, ease of collaboration, and intellectualism make it truly unlike any other place. The specialness of JILA comes from all the wonderful people that walk the halls.

First, and foremost, I would like to thank my advisors Debbie Jin and Eric Cornell. I'm grateful for them as they took me in as a lowly electrical engineer and allowed me to dress up and play as an experimental physicist. They are both paragon examples of physicists. Debbie continues to amaze me with her ability to dive exactly to the root of any scientific issue. I know no one else with Eric's ability to deeply understand a problem from multiple perspectives.

Much of the credit for the work in this thesis goes to my previous lab mates Juan Pino and Rob Wild. Juan drilled into me the power of data driven decision making. Rob showed me how think out of the box as he brought many creative solutions experimental problems. Recently, I've had the pleasure to work with Catherine Klauss. Cathy has been instrumental in our studies of the unitary Bose gas.

In addition, there are many people to thank for help in physics and distractions from physics. The greater JILA bi-group including Ruth Bloom, Tara Drake, Rabin Paudel, Matt Grau have done both. The JILA electronics shop and machine shop are a graduate students best friend. The electronics shop, especially Carl Sauer and Terry Brown, have been a great help with any electronics related issues, along with teaching me how little I actually know about electrical engineering. Hans Green in the machine shop deserves lots of thanks for answering my many random questions.

Many friends have helped me along the journey of grad school including Sara Fairchild, Sam

Berweger, Joanna Atkin, Craig Hogle, Will Kindel, Mike Foss-Feig, Jennifer Harlow, both the Absolute Zeros and the Moosecats softball teams and many others.

Lastly, this thesis would never had been written without the writing help of Joanna Atkin and Laura Nash. I'm deeply in indebted to them both.

Contents

Chapter

Tables

Table

Figures

Figure

Chapter 1

Introduction to this thesis

1.1 Introduction

Quantum mechanics provides a monumentally accurate description of the universe around us and is arguably the most successful theory of the physical world. Qualitatively, it describes many concepts that were previously unexplained (e.g. atomic spectra, black-body radiation, the electron work function, the double slit experiment, etc.). It is also hailed as the most quantitatively correct physical theory because the calculation of the fine-structure using the anomalous magnetic moment of the electron agrees with measurement to one part in 10^9 [1]. Recently, the 1995 creation of the first dilute gas Bose-Einstein condensation (BEC) [2] provided physicists with a new controllable macroscopic quantum mechanical system to study. This thesis describes studies of quantum mechanics using ^{85}Rb BECs.

Quantum mechanics offers a complete description of the physics for two-body systems. However, the calculations needed to describe strongly interacting systems with more degrees of freedom in the problem (e.g. more than two particles) quickly become impossible to do in a reasonable amount of time. And, even if one could calculate, for example, the ground state of an arbitrary quantum system, it's not clear how much insight into the physics of the system that gives. Thus, to gain any an understanding of many-body systems, the problem must be simplified and described by fewer parameters than the complete set of degrees of freedom [3]. Capturing a complete description of system by fewer degrees of freedom typically works when the system has weak interactions: For example, a weakly interacting BEC can be described using a single quantum mechanical wave-

function [4]. For a BEC, this approach is only valid for a dilute system, where the length scale of interactions is much smaller than the interparticle spacing, $na^3 \ll 1$, where n is the density and a is the scattering length.

So, Nature has played a cruel trick on us when making the most interesting systems exactly the ones not understood in a mean-field approach.[1] These are systems where the interactions are strong, the systems aren't dilute, and theoretical approaches are difficult. Since *ab initio* theory is intractable, physicists use experimental studies to build an understanding of strongly interacting many-body systems. Specifically, ^{85}Rb BEC has proved to be a particularly fruitful model system for exploring the transition from a weakly interacting mean-field description ($na^3 \ll 1$) to a strongly interacting system ($na^3 > 1$). The versatility of using ^{85}Rb BEC to study strongly interacting systems is due to the ability to tune the interactions by changing the scattering length, a. We typically start with a weakly interacting gas with $na^3 \ll 1$, evaporate to BEC, and then increase the interactions to the strongly interacting regime before probing the system. This thesis tells the story of our lab's studies of a BEC in the weakly interacting regime and of the first studies of a strongly interacting ($na^3 > 1$) BEC.

1.2 Thesis outline

I begin with a brief review of ultracold boson physics in chapter 2. I describe various physical phenomena of ultracold Bose gases relevant to our studies with ^{85}Rb BECs. I describe how we change the interactions, which are parameterized by the scattering length, with a Feshbach resonance. I also give an account of the first-order perturbations to mean-field theory for the energy density of a BEC. Lastly, I touch on three-body interactions in a BEC.

In chapter 3, I describe the apparatus and how we make a BEC. In our studies of strong interactions we wanted to change the magnetic field much faster than the apparatus was previously capable of. The approach we took was to add small additional coils that can change the field faster than the large trap coils. I describe these magnetic-field coils and the design challenges we solved

[1] It's possible physicists only find them interesting precisely because we don't understand them.

implementing them.

After discussing the apparatus, I describe in chapter 4 how we transitioned from studying weakly interacting to strongly interacting BECs. I include some background and context to the challenges associated with strong interactions in a BEC. Our work started by probing BECs in the weakly interacting regime, where we used two different probe techniques: Bragg spectroscopy and contact spectroscopy. Chapter 5 describes the Bragg spectroscopy measurement and chapter 6 describes the measurement of the contact. Lastly, I discuss unitarity, where the scattering length diverges. Our measurements of strongly interacting BECs are presented in chapters 6 and 7. I finish with my thoughts on future directions for the experiment in chapter 8.

Chapter 2

Ultracold bosons

Before I discuss our studies of a BEC in the strongly interacting regime ($na^3 > 1$), where mean-field and perturbation theory are not applicable, I will discuss the BEC physics we do understand.

In the weakly interacting regime ($na \ll 1$) a BEC is well described by mean-field theory. In this regime, three-body losses are small and evaporating to BEC is relatively easy. The weakly interacting dilute gas is accurately described by averaging over two-body interactions. Therefore, I discuss two-body scattering and our ability to tune the scattering length using a Feshbach resonance.

However, even for weak interactions, where the BEC is well described by mean-field theory, the interactions significantly affect the BEC. Last, even though three-body collisions are rare, three-body physics can play an important role. This chapter provides a brief overview to weakly interacting BECs, but is not intended to be an in-depth review. I give citations to many excellent review articles.

2.1 Two-body interactions and Feshbach resonances

Most of the time, atoms in an ultracold gas take turns interacting with each other; that is, they mostly undergo two-body collisions. When this is the case, we only have to understand the two-body scattering properties to describe the physics of the gas. We characterize the two-body interactions with a physical quantity called the scattering length, a, and use a Feshbach resonance to change the scattering length [5]. For ^{85}Rb, tuning the scattering length using a Feshbach resonance

has allowed the exploration of a BEC in the strongly interacting regime [6].

The scattering length characterizes the two-body scattering in ultracold gases [7]. Generally, the scattering cross section between atoms is dependent on short-range atomic potentials. To understand the scattering properties of the gas, the complicated short-range potentials would have to be considered; however, this calculation can be simplified by replacing the short-range atomic physics with a delta-function pseudopotential with an associated length scale – the scattering length. [1] The interactions are then completely characterized by the scattering length, rather than described by the atomic potentials.

The remarkable thing about ^{85}Rb is our ability to conveniently change the scattering length using a magnetic-field Feshbach resonance. The Feshbach resonance couples free atoms to a bound molecular state at a specific magnetic field (we use the ^{85}Rb 155 G resonance [9]). To change the scattering length, we tune the bound state energy relative to the free atom energy by changing the magnetic field. The scattering length is given by

$$a = a_{bg}\left(1 - \frac{\Delta}{B - B_0}\right), \tag{2.1}$$

where a_{bg} is the background scattering length, B is the magnetic field, B_0 is resonance location, and Δ is the width of the resonance. The binding energy of the Feshbach molecule, E_{mol} is

$$E_{mol} = \frac{\hbar^2}{ma^2}, \tag{2.2}$$

were m is the mass of an atom. At the resonance location, $B = B_0$, the scattering length diverges $|a| \to \infty$ and the molecule binding energy vanishes, $E_{mol} = 0$.

The Feshbach resonance parameters for ^{85}Rb were precisely measured by Claussen *et al.* [10], allowing precise control over the interaction. The scattering length for ^{85}Rb is shown in figure 2.1 as a function of magnetic field. Also, we plot the energy of a Feshbach molecule as a function of magnetic field in blue in figure 2.2. The 155 G ^{85}Rb Feshbach resonance is convenient because it is a wide resonance, with $\Delta = 10.71$ G [10]. The convenience of a wide Feshbach is countered

[1] Fermi was the first person to use a pseudo-potential when considering low energy electron scattering on ground-state atoms in 1934 [8].

by the negative background scattering length $a_{bg} = -443\,a_0$, which makes evaporating ^{85}Rb very challenging. A large BEC is unstable for negative scattering length [11]. In order to evaporate ^{85}Rb to BEC, we must precisely control the magnetic field and set the scattering length to a small positive value.

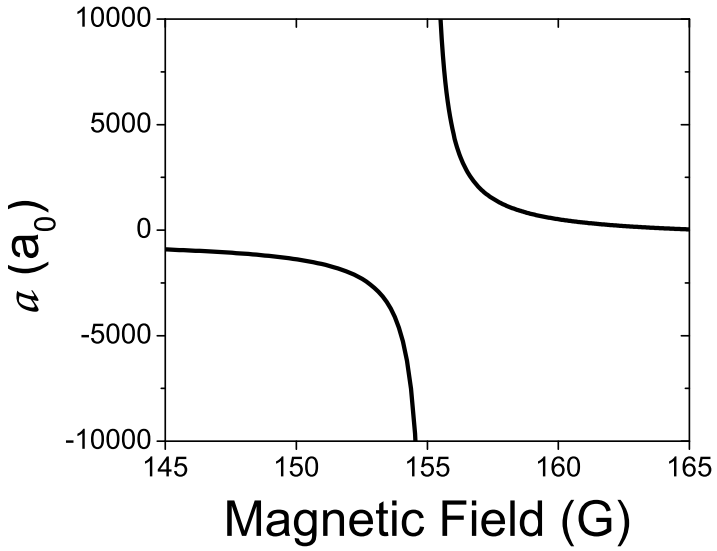

Figure 2.1: The ^{85}Rb 155 G Feshbach resonance. The x-axis is the magnetic field. The y-axis shows the scattering length in units of the Bohr radius. By changing the magnetic field, the scattering length can be tuned to any value. For this resonance $a_{bg} = -443(3)\,a_0$, $\Delta = 10.71(2)$ G, and $B_0 = 155.051(18)$ G [10].

2.2 Bose-Einstein Condensation

An atomic Bose-Einstein condensation was first made in 1995 [2] and quickly became a model macroscopic quantum system. Since it is a clean controllable system, many discussions of macroscopic quantum systems now begin with BEC. The small length scale of interactions compared to the interparticle spacing allows physicists to successfully describe a BEC with the Gross-Pitaevskii (GP) equation. The GP equation was derived in 1965 (well before the experimental observation of BEC) by Gross and Pitaevskii [12, 13] and describes the zero-temperature wave function of bosons. However, the GP equation is only valid for a dilute BEC, where $na^3 \ll 1$. The

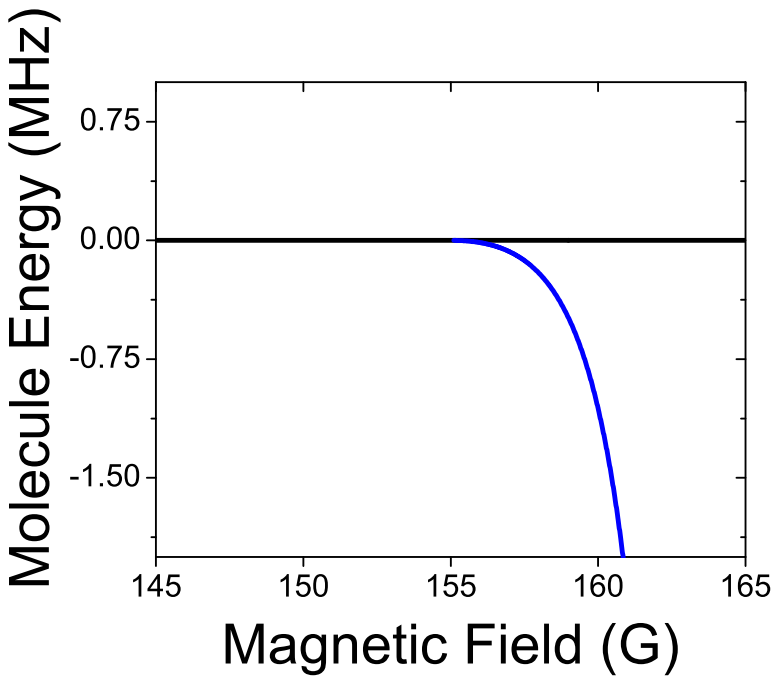

Figure 2.2: The binding energy of a Feshbach molecule. The x-axis is the magnetic field. The y-axis is the energy of the Feshbach molecule. The black line is the energy of two free atoms. The blue line is the energy of a Feshbach molecule. At the Feshbach resonance, the binding energy vanishes.

time-dependent GP equation is

$$i\hbar\frac{\partial}{\partial t}\Phi(\mathbf{r},t) = \left(-\frac{\hbar^2\nabla^2}{2m} + V_{\text{ext}}(\mathbf{r}) + g|\Phi(\mathbf{r},t)|^2\right)\Phi(\mathbf{r},t), \tag{2.3}$$

where $\Phi(\mathbf{r},t)$ is the order parameter of the condensate, $V_{\text{ext}}(\mathbf{r})$ is the external potential, and g is the coupling constant, which is given by

$$g = \frac{4\pi\hbar^2 a}{m}. \tag{2.4}$$

The time-independent GP equation is

$$\mu\phi(\mathbf{r}) = \left(-\frac{\hbar^2\nabla^2}{2m} + V_{\text{ext}}(\mathbf{r}) + g\phi(\mathbf{r})^2\right)\phi(\mathbf{r}), \tag{2.5}$$

where $\phi(\mathbf{r})$ is the order parameter of the BEC and μ is the chemical potential.

2.3 Interactions in a BEC and the LHY correction

Even for a weakly interacting dilute BEC, interactions modify the properties of the system. Perhaps the most striking modification of a BEC is the shape of the condensate. With no interactions, the BEC wave function is the ground-state wave function of the trap. With finite interactions and a large number of atoms in the BEC, even for $na^3 \ll 1$, the interaction energy term is much larger than the kinetic energy term in the GP equation (equation 2.5). When neglecting the kinetic energy term in equation 2.5 (this is called the Thomas-Fermi approximation), the BEC takes on the shape of the external potential:

$$n(\mathbf{r}) = \phi(\mathbf{r})^2 = g^{-1}\left[\mu - V_{\text{ext}}(\mathbf{r})\right]. \tag{2.6}$$

If we increase na^3, the GP equation becomes less valid because the approximation of $na^3 \ll 1$ was used to derive the GP equation. For a small but finite value na^3, a perturbation approach can be used to describe the gas. The Lee, Huang, and Yang (LHY) correction [14] famously gives the first beyond-mean-field correction to the energy density of a BEC. The energy density of a BEC is

$$\mathcal{E} = \frac{gn^2}{2}\left(1 + \frac{128}{15\sqrt{\pi}}\sqrt{na^3} + ...\right). \tag{2.7}$$

The first term in the equation is the mean-field contribution to the energy, while the $\sqrt{na^3}$ term is the LHY correction. There have been many beyond-mean-field studies of a BEC [15, 16, 17, 18, 19, 20, 21] and recently the LHY correction was precisely measured in a BEC [17].

2.4 Three-body recombination

In a Bose gas, the collisions mostly involve two bosons, but sometimes three collide. [2] When three bosons collide, they have a chance to undergo a three-body recombination event. Three-body recombination occurs when two free atoms form a molecule, with the binding energy converted into kinetic energy. A third atom must be part of the collision to satisfy momentum and energy

[2] In contrast, in a two-component Fermi gas three-body collisions are suppressed due to the Pauli exclusion principle.

conservation. The binding energy of a molecule is typically much larger than the energy per atom in the BEC. The dimer and free atom then fly away from each other with much more energy than the chemical potential of the BEC. The fast moving atoms are typically lost from the trap, and if they collide with other atoms on the way out the remaining cloud is heated. Additionally, three-body losses selectively removes more atoms from the coldest, most dense, part of the cloud, which overall heats the cloud and is referred to as anti-evaporation.

An ultracold Bose cloud in a trap will experience three-body recombination events that manifest as loss of atoms from the cloud. The loss rate is described by the three-body loss coefficient L_3, where the density and number of atoms in the cloud are given by

$$\dot{n} = -L_3 n^3 \tag{2.8}$$

$$\frac{\dot{N}}{N} = -L_3 \langle n^2 \rangle, \tag{2.9}$$

where N is the total number of atoms in the cloud and $< n^2 >= \int n^3 d^3x/N$. We obtain equation 2.9 by integrating equation 2.8 over all space. The three-body loss coefficient L_3 scales as

$$L_3 \sim \hbar a^4/m, \tag{2.10}$$

where a is the scattering length [22, 23]. The three-body losses increase as a^4 in a cloud of ultracold bosons [24, 25, 6]. The increase of three-body losses with scattering length has historically been the limiting factor in studying strongly interacting Bose gases.

2.5 Efimov resonance and trimers

In addition to the Feshbach two-body bound state, shallow three-atom bound states exist for ultracold bosons. In 1970, Efimov derived [26] an infinite series of trimer bound states for particles with two-body interactions. These Efimov trimers result from the two-body interactions in the context of nuclear physics. Remarkably, even when all two-body interactions between atoms are repulsive, a trimer bound state still exists. Recently, Efimov physics has been extensively explored in the context of ultracold gases [27]. To observe Efimov physics in our ultracold gas system, we

measure the three-body loss rates of the cloud. Efimov physics modifies the a^4 loss rate with a log-periodic structure. We discovered an Efimov resonance in ^{85}Rb by observing enhanced loss where the Efimov trimer state is degenerate with the free atom energy; we describe our measurement of Efimov trimers in chapter 6.

Chapter 3

The Apparatus

This chapter presents an overview of the apparatus and our procedure to make ^{85}Rb BECs, along with details about my technical contributions to the apparatus. I am now the fourth graduate student to do my Ph.D. work with the machine and the third student to make ^{85}Rb BECs in our 10 Hz spherical magnetic trap. Because the experiment has been excellently documented by my predecessors in previous theses [28, 29, 30], I will give here a brief introduction to the experiment rather than many technical details. The majority of the chapter will focus on the latest improvement we've made to the apparatus: the fast magnetic-field system.

The experiment was built to reliably make ^{87}Rb and ^{85}Rb BECs. In addition, we control the interactions of ^{85}Rb atoms via a magnetic-field Feshbach resonance. BECs are made with a 90 s cycle time. The machine has been quite reliable over the years, daily cooling to BEC for months at a time. There have been with brief moments (of terror) when the experiment was out of order, but most maintenance has involved minor trap alignments or tweaks of the laser system.[1]

3.1 How to make a ^{85}Rb BEC

Our experimental sequence is similar to many other ultracold atomic gas experiments [31, 32, 33]. We initially collect as many atoms as we can in a magneto-optical trap (MOT), move the atoms to a higher vacuum region, then evaporatively cool the cloud. Our experimental sequence is as follows: We start by trapping and laser cooling ^{85}Rb and ^{87}Rb from a room temperature

[1] Examples of more challenging problems to fix include steam coming out of the cart coils, flaky transfer coil servo grounding, and a broken motorized flipper spring.

vapor in a magneto-optical trap (MOT). We then use a moving magnetic potential to move the atoms from the MOT chamber, where the vacuum-limited lifetime (lifetime of the trapped gas) is only 5 s, to the science cell, which has a vacuum-limited lifetime of 500 s. Once in the science cell, ^{85}Rb is cooled sympathetically while ^{87}Rb is evaporatively cooled. We evaporate ^{87}Rb first in a magnetic Ioffe-Pritchard trap [34], then a hybrid optical-magnetic trap, and finally in a 10 Hz spherical Ioffe-Pritchard magnetic trap. We set a small ($\sim 100\, a_0$) scattering length in the 10 Hz trap by tuning the magnetic-field near the Feshbach resonance location. We end with a pure ^{85}Rb BEC by evaporating ^{87}Rb completely until no ^{87}Rb atoms remain trapped.

We use absorption imaging on a cycling transition to measure the number and temperature of either the ^{87}Rb or ^{85}Rb cloud. First, we transfer the atoms to a state with a cycling transition (for ^{87}Rb $|F = 2\ \mathrm{m_F} = -2\rangle$ and for ^{85}Rb $|F = 3\ \mathrm{m_F} = -3\rangle$) using either optical pumping or RF techniques. Then, to measure the 2D optical density profile of the cloud, we pulse on a laser resonant with the cycling transition and use absorption imaging techniques [35]. Because of the high optical density of the BEC, we use a high-intensity imaging pulse to increase the dynamic range the imaging [36]. During my tenure in lab we regularly made ^{85}Rb BECs of 7×10^4 atoms.[2]

3.2 Changing the magnetic field quickly

3.2.1 Fast-B system

Since making BEC was a repeatable and reliable process, I was able to turn my attention to developing new techniques to probe a BEC. We were motivated to change the interactions of a BEC very quickly to study a strongly interacting gas, as described in chapter 2. The previous method of changing the total magnetic-field magnitude was to tune the current flowing through the bias coils of the Ioffe-Pritchard trap. However, the bias coil step response time is $\sim 100\ \mu$s, and we empirically found these ramps were too slow for our purposes. To change the field faster, we used small low-inductance coils very close to the atoms, following the example of other labs [37, 31, 38].

[2] The number of ^{85}Rb BEC atoms quoted in theses has increased from 4×10^4 in Juan's thesis [29] to 6×10^4 in Rob's thesis [30] to now 7×10^4. I'm confident my successors will quote an even higher number after their improvements and optimizations to the apparatus.

To change the magnetic field, we developed a system we call the fast-B system. To be "quick" with respect to the atoms, the magnetic-field ramp time has to be much faster than the fastest timescale the atoms interact on. We can estimate a fastest timescale for any dynamics in the gas by considering the timescale set by the distance between atoms, which is 60 μs; $t = 2m/(\hbar(6\pi^2 n)^{2/3})$, where $n = 5 \times 10^{12}\text{cm}^{-3}$ is a typical density for our ^{85}Rb BEC. (A complete discussion of the timescales of our experiment is given in chapter 4.) I next describe the coils, our motivations, and our design.

Our goal in designing the fast-B coils was to change the magnetic field as fast as possible (or at least much faster than 60 μs). The coils are coaxial with the bias magnetic-field direction so that they generate a magnetic field that adds linearly to the magnitude of the larger field. The coils are essentially inductors with series resistance, so, in order to change the magnetic field as fast as possible, we need to maximize dI/dt. The current, I, inductance, L, and voltage, V, for an inductor are related by

$$V = L\frac{dI}{dt}. \tag{3.1}$$

It's clear from equation 3.1 that we should maximize V and minimize L to design the fastest coils. Other labs in JILA have maximized V by charging capacitors to hundreds of volts (dangerous) and minimized L by only using a single loop of wire for the coil. However, this approach is flawed since it only considers the coils and ignores the rest of the system. With only one loop as the coil, the wire leads from the power supply have the same (or more!) inductance than the coil itself; therefore, this is clearly is not the ideal design strategy. And indeed, these systems are typically limited by the inductance through the relations of equation 3.1. However, the speed of change of the magnetic field isn't maximized, even though the slew rate of the current is. The disadvantage of a system limited by the slew rate is understood by considering a single turn coil whose leads have more inductance than the coil. If we add one more loop in the coil the inductance stays about the same, but the magnetic-field contribution and thus the magnetic-field ramp rate will double.

Instead, we designed the fast-B system by considering the coils as part of a larger feedback

system, shown in figure 3.1. We designed the coils to be limited by the feedback system rather than by equation 3.1. The two coils have 10 turns, a radius of 0.5 cm (an inductance of ~ 1 μH), and are 2 cm apart. We require ~ 10 G to change the interactions in the BEC from the mean field regime to unitarity. Assuming a 5 μs ramp time, the required voltage to drive these coils is 1.7 V, which is small compared to the 30 V we use to power the system. The specifications for the fast-B coils compared to the bias coils are listed in table 3.1. The 10 - 90 % step response of the coils is $t_r = 2.1$ μs, as shown in figure 3.2. This corresponds to a system bandwidth of 860 kHz (using $\omega_n \cong 1.8/t_r$, equation 3.49 in [39]), which is approximately a two order of magnitude improvement over our previous ramps. However, with these new and improved fast-B coils, we are too fast in changing the magnetic field! Induced currents in other coils and eddy currents in surrounding conductors cause a transient magnetic field that opposes any fast change. These induced currents limit our overall control of the atoms interactions and we have to correct for them.

Table 3.1: Fast-B coil parameters compared to bias coils.

	Bias coil	Fast-b coil
Coil separation	4.76 cm	2 cm
Coil radius	3.8 cm	0.5 cm
Coil inductance	37 μH	~ 1 μH
Magnetic field per amp	1.609 G/A	1.109 G/A
Magnetic field curvature	0.087 G/A/cm^2	7.83 G/A/cm^2
Current required for 10 G	6.2 A	9.1 A
Voltage required for 10 G / 5 μs	45.6 V	1.7 V
Number of turns	8	10

3.2.2 Pre-correcting for Faraday's law

The quick magnetic pulse from the fast-B coils creates a large change in magnetic flux close to the atoms. Faraday's law tells us that a changing magnetic field induces an orthogonal electric field. If the induced electric field is in a conductor, it causes a current to flow, which generates a

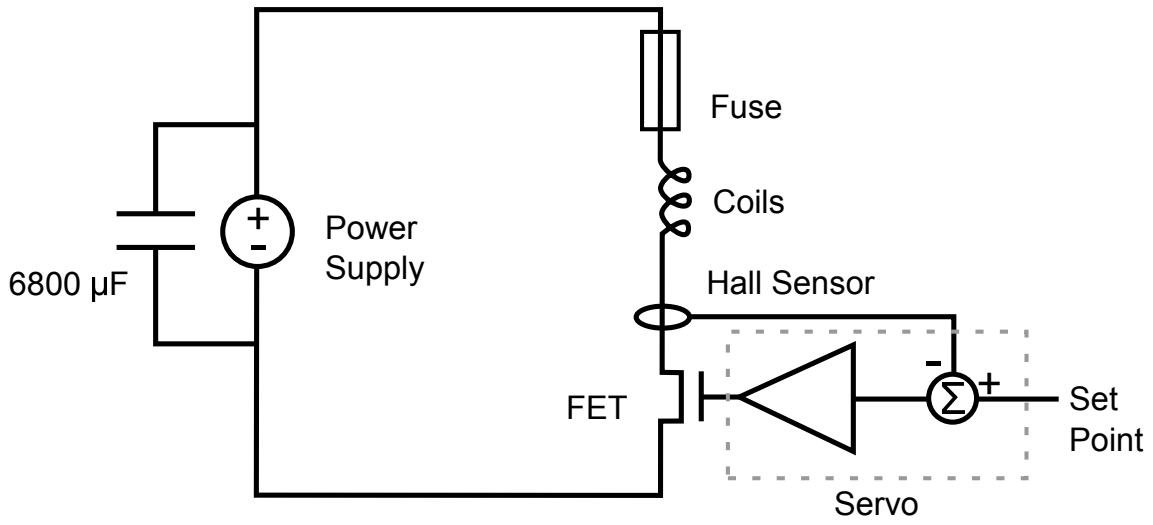

Figure 3.1: A schematic of the fast-B system. The fast-B coils are part of a simple PID feedback loop. We supply current through the coils from a power supply and control the flow using a FET. We measure the current using a Hall effect current sensor. The set point and measured current are subtracted to create an error signal.

magnetic field that opposes the original field. We found that two things happen when we ramp the field quickly with the fast-B coils. First, the fast-B coils induce small transient currents in two pairs of coils in the Ioffe-Pritchard trap: the bias coils and the pinch coils. Second, we see a discrepancy between the measured currents in all the coils and the measured magnetic field. The fast-B ramp and three sources of inductive coupling in our system are demonstrated in figure 3.3. The fast-B magnetic-field ramp is shown in figure 3.3 (a). We ramp the field very quickly in order to measure eddy currents and induce currents in the other coils. The induced currents in the bias (green) and pinch (blue) coils are shown in figure 3.3 (b), where I have converted the currents into magnetic field using measured calibrations of these coils. We subtract the bias and pinch current offset values. Figure 3.3 (c) shows the sum of all the coils compared to measurements of the total magnetic field. The total magnetic field was measured using RF spectroscopy on atomic Zeeman levels. We attribute the difference between the measured field and the expected total field from the currents due to eddy currents. So, although we control the current though the fast-B coils exquisitely, we need to account and correct for the induced fields to control the magnetic field with

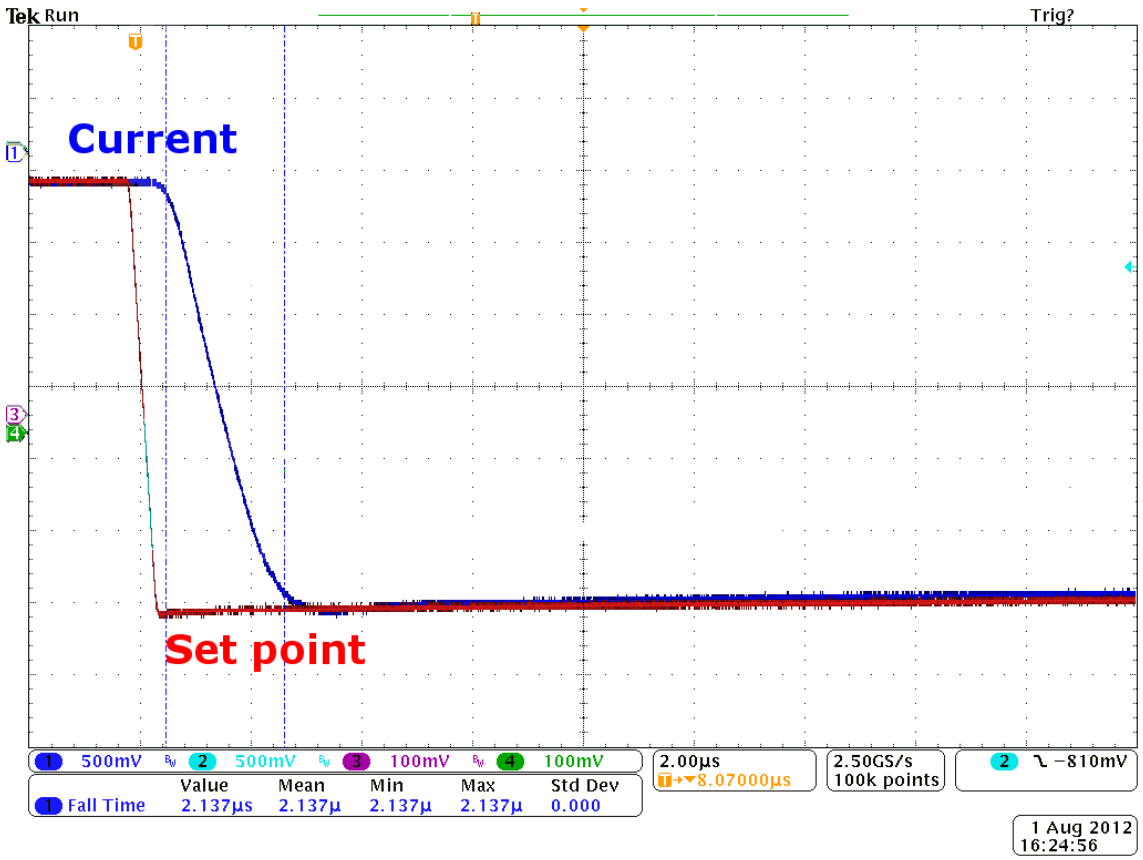

Figure 3.2: A scope trace of the step response of the fast-B coil. We plot the current set point (red) and measured current (blue). We observe the system response after the set point is jumped from one value to another. The 10% - 90% step response time is 2.1 μs. We characterize the bandwidth of the system using this step response time.

the same precision.

To pre-correct for the eddy currents, we need to understand how they behave; we have made a mathematical model to predict the induced currents. Our model is a simple circuit lumped-element model, shown in figure 3.4. The coupling between the fast-B coils and other elements is treated as mutual inductances between inductors. The fast-B coils are modeled as an ideal current source flowing through an inductor. The eddy currents in surrounding conductors are modeled as an LR circuit while the bias and pinch coils are modeled as LRC circuits. The eddy currents are physically a current circulating in a conductor somewhere near the magnetic trap. The current path in the inductor has an inductance and resistance. Thus, we model the eddy currents as a lumped-element

LR circuit. However, the bias and pinch coils are under an active feedback loop during the fast-B jump. Empirically, a second order differential-equation LRC model fits the measured current well. Also, any complicated many-order feedback system can be approximated by a second order system. In feedback systems theory this is known as the dominant pole approximation [40]. The system of coupled differential equations then is

$$M_e\frac{dI_f}{dt} + L_e\frac{dI_e}{dt} \quad + R_eI_e \qquad\qquad = 0 \tag{3.2}$$

$$M_b\frac{d^2I_f}{dt^2} + L_b\frac{d^2I_b}{dt^2} \quad + R_b\frac{dI_b}{dt} + \frac{1}{C_b}B_b \quad = 0 \tag{3.3}$$

$$M_p\frac{d^2I_f}{dt^2} + L_p\frac{d^2B_p}{dt^2} + R_p\frac{dB_p}{dt} + \frac{1}{C_p}B_p = 0, \tag{3.4}$$

where M is the mutual inductance, L is inductance, R is the resistance, and C is the capacitance. The subscripts f, e, b, and p corresponds to the fast-B, eddy currents, bias coils, and pinch coils.

We can cast these equations into a more convenient form. Assuming $B \propto I$ the equations are written as a function of magnetic field B, the coupling between the coils α, a characteristic decay time τ, and a second-order parameter X. These equation are

$$-\alpha_e\frac{dB_f}{dt} = \frac{dB_e}{dt} + \frac{1}{\tau_e}B_e \tag{3.5}$$

$$-\alpha_b\frac{d^2B_f}{dt^2} = \frac{d^2B_b}{dt^2} + \frac{1}{\tau_b}\frac{dB_b}{dt} + \frac{1}{X_b}B_b \tag{3.6}$$

$$-\alpha_p\frac{d^2B_f}{dt^2} = \frac{d^2B_p}{dt^2} + \frac{1}{\tau_p}\frac{dB_p}{dt} + \frac{1}{X_p}B_p. \tag{3.7}$$

To find the constants α, τ, and X we compare our measurements to the model. We change the parameters till the model agrees with the measurements. The final constants are shown in table 3.2. The comparison between the bias and pinch coil currents and the model is shown in figure 3.5. To calibrate the eddy current model we compare the currents through the coils and the total magnetic field. After finding the appropriate eddy current parameters, we can put all the pieces together. Figure 3.6 shows the comparison between the measured magnetic field (black circles), the field contribution from the fast-B coils (blue), and the full model (red). After our calibrations, the model agrees excellently with the data. The total magnetic-field jump was about 10 G and we

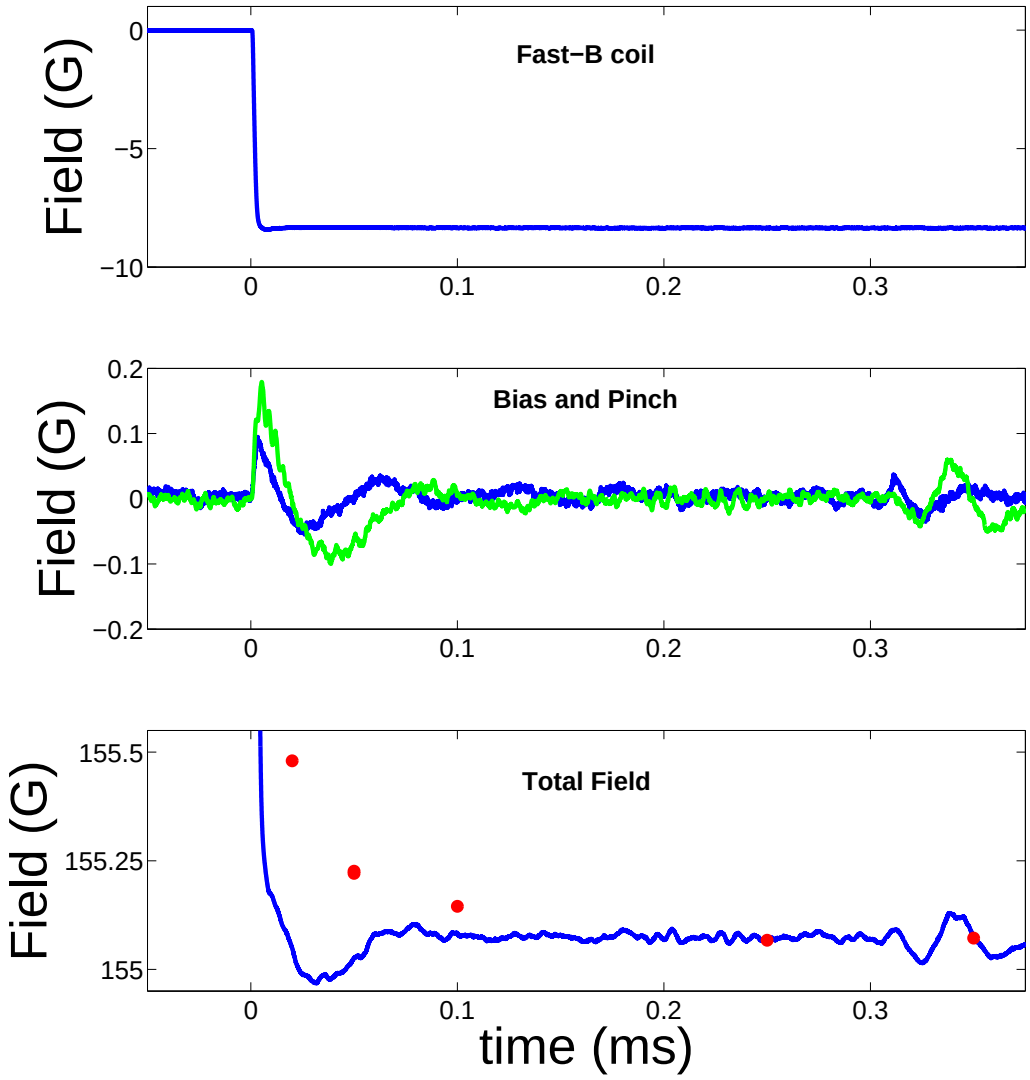

Figure 3.3: The transient magnetic field and the contributions from the fast-B coils, the bias coils, and the pinch coils when jumping the field from an initial value of approximately 163 G to the Feshbach resonance location at 155 G. The magnetic-field contribution of the fast-B coil is plotted in part (a). The contribution to the magnetic from the bias and pinch coils is shown in part (b). The steady-state values of the magnetic-field contributions from the bias and pinch coils have been subtracted. Part (c) shows the sum of the magnetic-field contributions from all the coils (blue) compared to measurements of the field (red). We attribute the disagreement between the data and curve to eddy currents.

find the agreement better than 10 mG, except for one data point. The corrections we made for

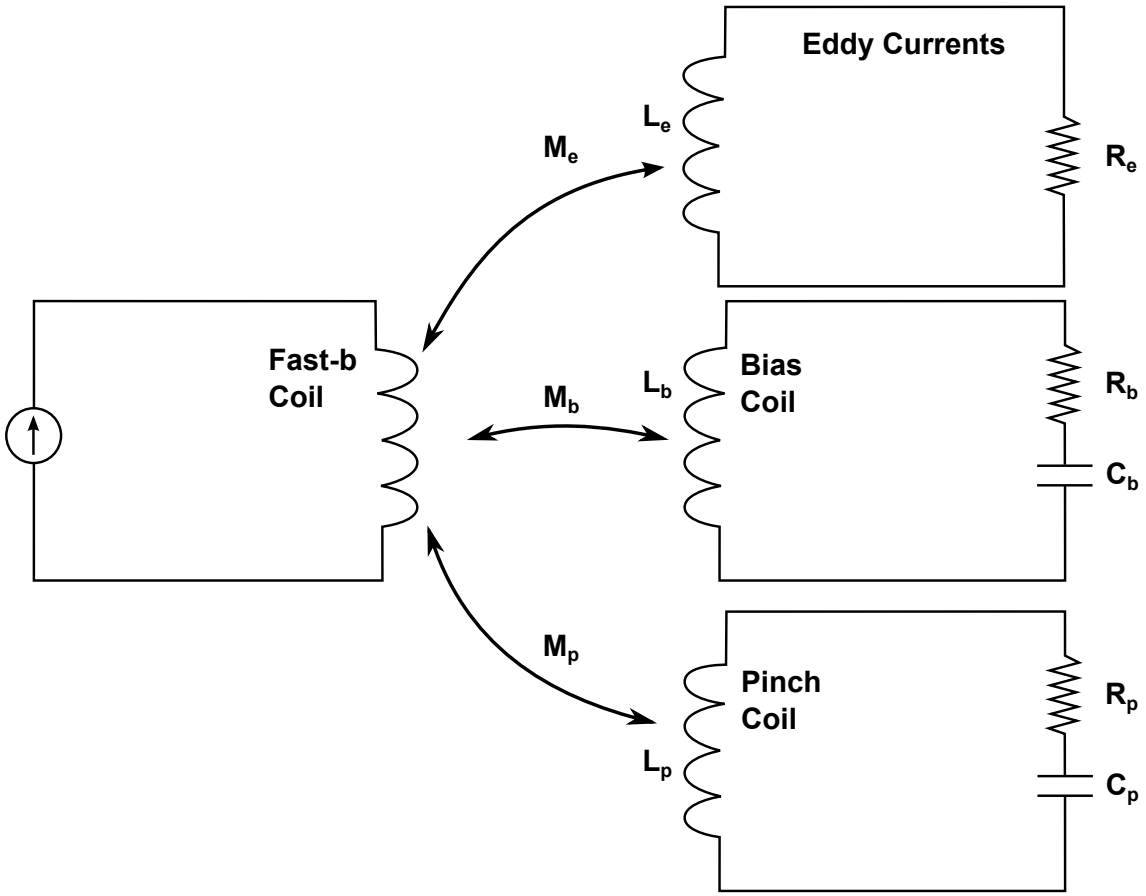

Figure 3.4: The lumped-element circuit model of the inductive coupling. The fast-B coils inductively couple to eddy current, bias coil, and pinch coil inductances. The mutual inductances are shown as arrows. The eddy currents are modeled as an LR circuit. The transient bias and pinch currents are LRC circuits.

this specific data were on the order of 500 mG, shown in figure 3.7. Further calibrations with more measured magnetic-field points would allow us to find better agreement.

Table 3.2: The inductive current model constants.

	α	τ	X
Eddy currents	0.068	45 μs	
Bias coil	0.0269	13 μs	$2.0787 \times 10^{-}10$ s^{-2}
Pinch coil	0.016	17.5 μs	$1.0731 \times 10^{-}10$ s^{-2}

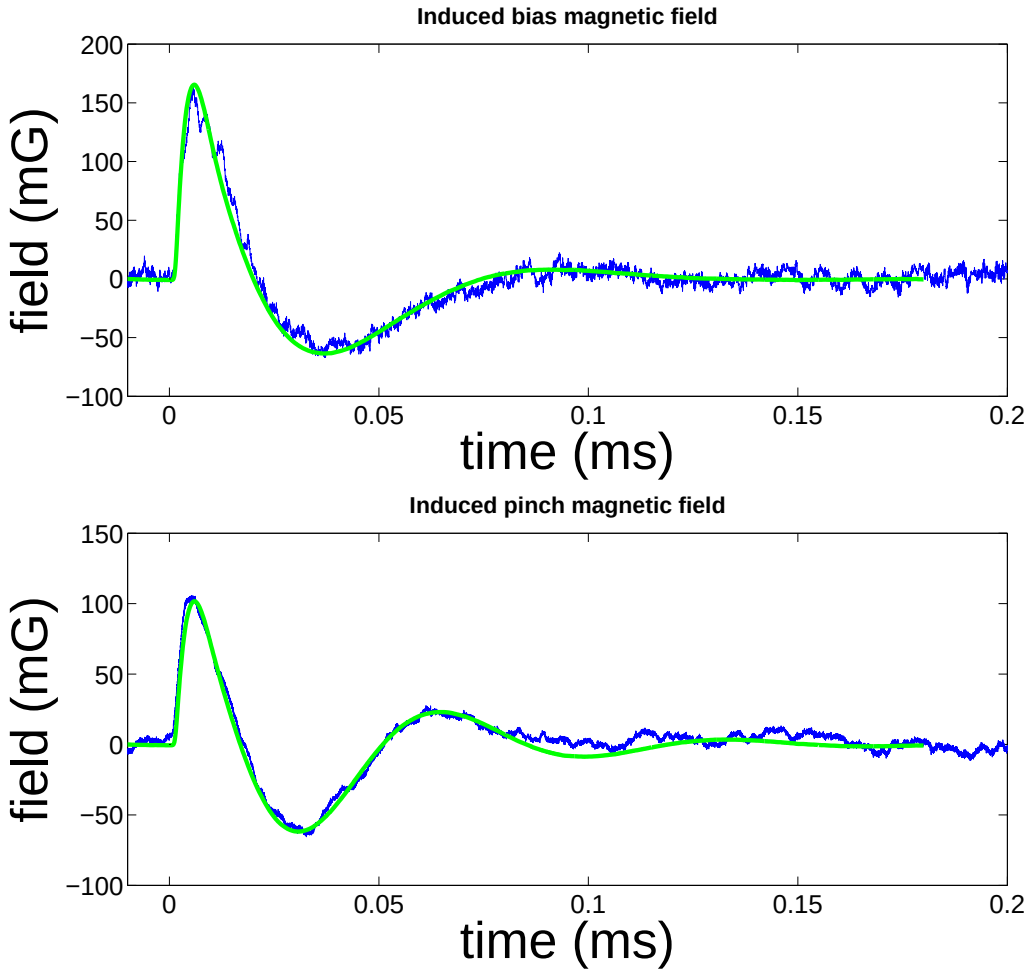

Figure 3.5: The magnetic-field contribution from the bias and pinch currents are shown in (a) and (b), respectively. The blue lines are measurements of the current through the coils and the green lines are the models based on LRC components. The model and measured currents agree excellently.

At the end of the day, we are very happy with the performance of the fast-B magnetic-field control system. We step the magnetic field in less than 5 μs. We can control the absolute magnetic field within 10s of mG by pre-compensating for eddy currents. The fast-B system is reliable and repeatable and doesn't interfere with the rest of the apparatus.

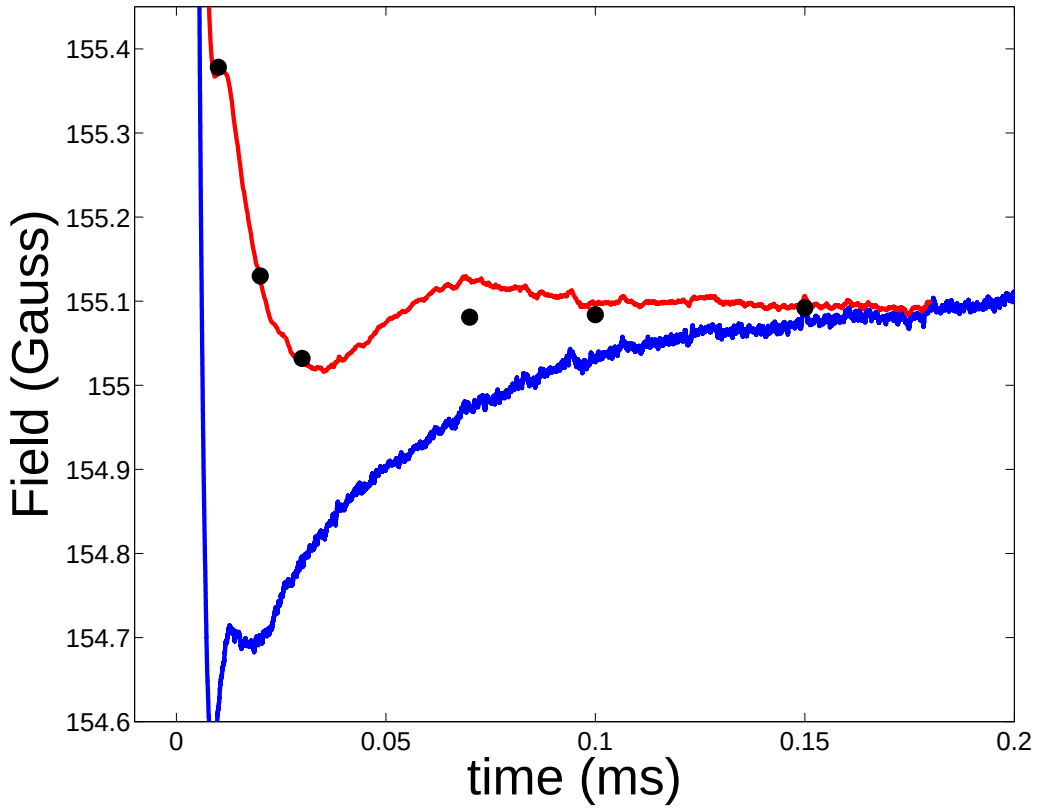

Figure 3.6: The full model compared to magnetic-field measurements. The magnetic-field contribution from the fast-B coils, calculated directly from the measured current in the fast-B coils, is shown in blue. The red curve is the total magnetic field, after adding the calculated contributions from the eddy currents, bias coils, and pinch coils. The black points are measurements of the field using RF spectroscopy. The measurements differ from the model by less than 0.05 G, while differing from only the fast-B magnetic field contribution by more than 0.5 G.

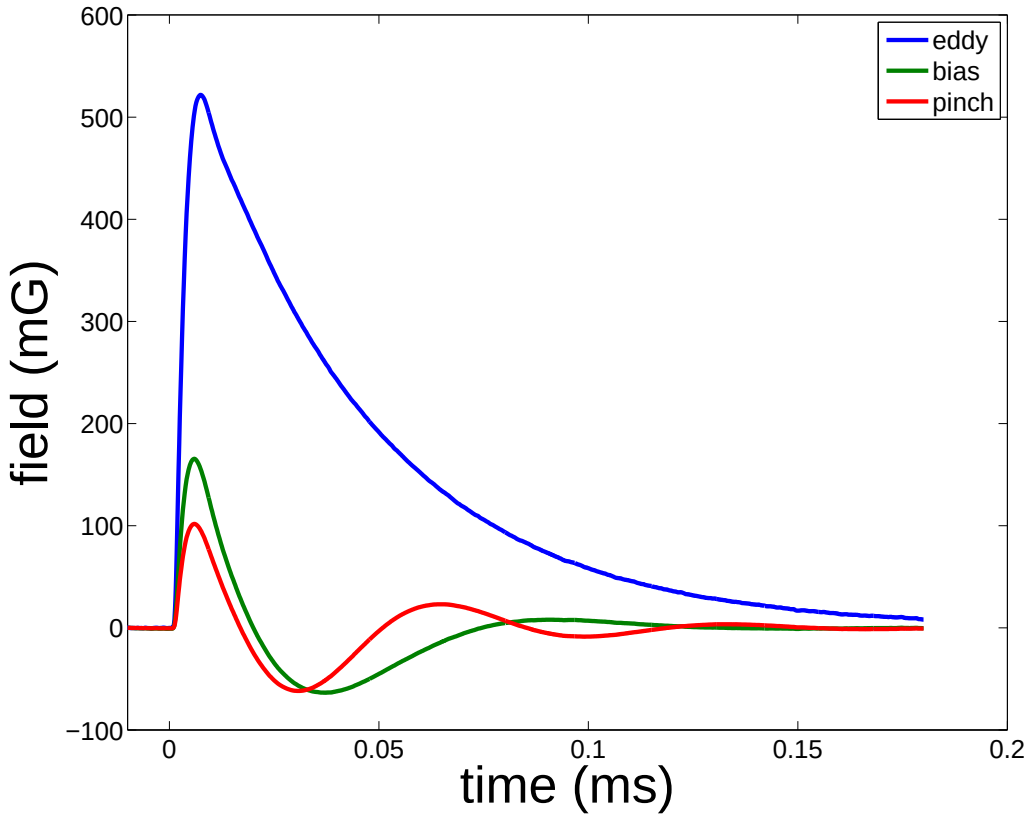

Figure 3.7: A plot of the calculated magnetic-field contributions from the eddy currents, bias coils, and pinch coils. We jump the fast-B coil approximately 10 G in 5 μs and calculated the induced currents. The largest contribution is due to the eddy currents.

Chapter 4

The story of probing strongly interacting systems

An open problem in physics is understanding how complex behavior emerges in systems made up of many interacting constituents. The physical world is made up of large many-body quantum systems and, although the microscopic behavior may be known for two particles, the many-body system can be "more than the sum of its parts." That is, many-body systems have complicated behavior that is not intuitive only from their two-body interactions. When the interactions are weak, many-body systems can be understood by averaging over the contributions from other particles; this averaging over all other particles is called a mean-field approach. However, this mean-field approach fails when the interactions are strong. Thus, understanding these strongly interacting many-body systems remains an exciting frontier of physics. Using a ^{85}Rb BEC we tune a many-body system from weak to strong interactions. We change the scattering length in a ^{85}Rb BEC and then probe the system to build an understanding of how strongly interacting many-body systems behave.

The behavior of two isolated interacting particles compared to two particles imbedded in a many-body system can be fundamentally very different. A prototypical example of this difference is the behaviour of electrons in a metal. Isolated electrons are charged particles that interact through the Coulomb interaction. When in a metal, surrounded by a sea of electrons, electrons are instead described by Landau-Fermi liquid theory. This transition from few to many is a current hot topic of research in ultracold gases [41, 42].

Dilute weakly interacting many-body systems can be understood in a mean-field approach,

but mean-field theories break down for strongly interacting many-body systems, which lie at the frontier of understanding in physics. To makes strides in understanding these systems, experimental investigations of strongly interacting systems are essential.

One particular approach is to use ultracold gases to study strongly interacting systems. Ultracold atomic gases are proving to be excellent model systems for the study of few and many-body physics. In particular, nearly all the aspects of an ultracold gas can be controlled: the particle number, the density, the geometry of the system, the interactions, and the dimensionality. Using this freedom of control, atomic physicists are beginning to create quantum systems using both a bottom up or top down approach. For example, experimentalists are beginning to build quantum systems from the bottom up, placing atoms one by one and coupling them together arbitrarily [43, 44]. Also, efforts to make quantum computing gates, study quantum information, or to investigate quantum metrology take advantage of coupling trapped atomic ions [45, 46, 47]. Rather than building the systems from the bottom up, the top down approach is to tune the interactions of bulk 3D, 2D, or 1D systems or to make artificial crystals of atoms in optical lattices [48]. Our particular experiment takes a top down approach by tuning the interactions in a bulk 3D BEC from weak to strong interactions.

The use of Feshbach resonances to change the scattering length is an incredibly powerful tool to tune interactions in a BEC. However, there is no free lunch for our BEC. Three-body inelastic collisions begin to dominate the system as we increase the scattering length, since the three-body recombination loss rate increases as a^4. As we try to access a strongly interacting regime (i.e. where a is large), three-body recombination thwarts the study of an equilibrium 3D Bose gas. The gas decays away during the ramp to large scattering length and an equilibrium is never reached. Various experiments have side stepped this problem by putting bosons in a lattice and limiting the site occupation to fewer than three atoms or reducing the dimensionality of the system to 2D or 1D systems, where inelastic losses are less prevalent. These approaches lead to interesting physics (Bose-Hubbard Hamiltonians, Tonk-Girardeau gases, etc.), but these systems give up degrees of freedom in order to limit losses. Perhaps the most radical work around of inelastic losses is to

study fermions instead of bosons.[1] As we mentioned though, fermions don't undergo three-body inelastic processes in a two-component Fermi gas because of the Pauli exclusion principle.

This chapter outlines how we transitioned from studying BECs with $na^3 \ll 1$ to BECs with $na^3 > 1$. We introduce our motivation for studying strongly interacting many-body systems. In our studies, we first probed a BEC with $na^3 \ll 1$ using Bragg spectroscopy and contact spectroscopy. Then, we increased the interactions in the BEC to $na^3 > 1$ by tuning the magnetic field to the Feshbach resonance so that the BEC is at unitarity where $|a| \to \infty$. However, at unitarity the gas is metastable and thus we needed to understand on what timescale it decays. We have performed two measurements of this system: (1) measuring the evolution of the momentum distribution $n(k)$ and (2) measuring the contact.

4.1 Liquid helium

The ubiquitous motivation for studying strongly interacting quantum liquids is superfluid liquid Helium. In 1937, Kapitza and Allen discovered that liquid ^{4}He undergoes a phase transition at 2.2 K [49, 50]. Below the phase transition temperature, ^{4}He becomes a superfluid, which is a liquid with zero viscosity. The desire to explain the properties of this quantum liquid has inspired much of the theoretical work that was later used to describe Bose-Einstein condensation. However, because ^{4}He is a stongly interacting quantum fluid, the theories were inadequate: Most theories assume only pair-wise interactions between particles, but, for ^{4}He, the distance between particles is roughly the same as the distance that characterizes the interactions. The assumption of only two-body interactions breaks down for this system and therefore the theories don't apply to liquid ^{4}He. The ability to tune ^{85}Rb BEC from dilute to strong interactions makes it a model system to explore the physics of quantum liquids.

[1] Not that fermions aren't very interesting in their own right.

4.2 Metastablity and local equilibrium

Although a BEC is in the motional ground state of an external potential, it can decay to a lower energy state (molecules and eventually a solid) and thus has a finite lifetime. If we are to experimentally probe the BEC, we must probe faster than this lifetime of the gas. In addition to the loss mechanism above, there are technical reasons the BEC will have a finite lifetime. The dullest reason for the BEC's finite lifetime are collisions with background gas in the vacuum chamber. We measured the vacuum-limited lifetime, or the lifetime due to background collisions, in our science cell to be 500 s, which is longer than our experiment cycle time. Thus, the vacuum-limited lifetime is not a concern for the lifetime of the BEC, but three-body inelastic loss can occur on time scale that is much faster. The process of three-body recombination converts atoms in the dilute gas into tightly bound molecules. The lifetime due to three-body recombination during the evaporation to BEC is long compared to the timescale of BEC measurements, but the three-body losses increase as a^4. As a gets large, this lifetime can be shorter than the timescale of our measurements. In addition, if we increase the scattering length quickly, interaction pressure excites a collective density breathe mode of the cloud. This causes the density to begin decreasing and thus also reduces na^3. This density breathe mode has a period of half the trap period. Since our trap has a 100 ms period, we must probe the cloud faster than approximately 5 ms if we want the change in n to be small.

After we evaporate to degeneracy, the BEC is in thermal equilibrium (although not in the true ground state of ^{85}Rb). To probe larger na^3, we quickly increase the scattering length a using the Feshbach resonance. Due to interaction pressure, the cloud will begin to "breathe" out, lowering n, and reducing na^3. After the quick change in a, the cloud is not in a *global* equilibrium; however, the gas can be in equilibrium *locally*. That is, locally in the BEC, the atoms can behave as if they are in equilibrium at the larger scattering length but with the local density unchanged from the initial local density before the fast change in a. While locally the gas might be described with a temperature, this "temperature" varies across the trapped cloud. A minimum requirement for the system to stay locally in equilibrium is that the change in scattering length be slow compared the

two-body timescale, which is characterized by the molecule binding energy.

The idea of a local equilibrium was important for our experiments that probed the BEC using Bragg spectroscopy and contact spectroscopy. We changed the interactions to a region where the LHY correction was small compared to one, but not insignificant. We changed a on a timescale that was much shorter than the trap period, so that the cloud was out of equilibrium globally; however, $\dot{a}/a$ was much smaller than $\hbar/E_b$, where E_b is the binding energy of a two-body Feshbach molecule. The breathe excitation and three-body losses caused na^3 to decay by 50% within about 10 ms after the change in a. Thus, it was important that our probes were faster than this decay time. However, at large enough scattering lengths the breathe and losses occurred during the ramps and the BEC decayed before we reached the final scattering length. We found that three-body losses and breathe limited us to $na^3 \approx 0.006$.

4.3 Studies in the perturbative regime of interactions

We developed two probes to study the interacting BEC in the perturbative regime: Bragg spectroscopy (the results are described in chapter 5) and contact spectroscopy (the results are described in chapter 6). For both experiments, we started with a dilute BEC where $na^3 < 10^{-6}$, then ramped a (we reached a max value of $na^3 \approx 0.006$), and probed the BEC before any significant losses occurred. Here, we tried to ramp slowly enough that the gas remains in a *local* equilibrium.

4.3.1 Bragg spectroscopy

Bragg spectroscopy is a useful tool for probing ultracold quantum gases that has been applied by many experimental groups to study BEC [51, 52, 53, 15]. A simple picture of Bragg spectroscopy is the absorption of a photon from one laser beam and then stimulated emission into another. The momentum difference of the two photons is imparted to the ultracold gas. For counter-propagating beams, the Bragg scattering imparts twice the momentum of a single photon. For momentum and energy conservation to hold, the energy and momentum difference between the two photons must satisfy the dispersion relation for excitations of the BEC. By varying the energy, or frequency

difference, of the two laser beams and measuring the response of the atoms, Bragg scattering can be used to measure the energy of excitations of the gas at a specific momentum. The Bragg signal will have two peaks: one when the frequency difference of the lasers is positive and one where the difference is negative. The positive and negative detunings correspond to a photon being either added to or subtracted from a particular laser beam. To change the momentum imparted to the gas, we can change the angle between the lasers, which sets what fraction of a photon's momentum is transferred to the cloud.

Papp *et al.* used Bragg spectroscopy to probe a ^{85}Rb BEC at various interaction strengths using counter-propagating beams [15]. However, counter-propagating laser beams impart relatively large-momentum excitations to the BEC. A Bragg excitation with twice the momentum of a photon excites atoms in the BEC to free-particle states with $E = \hbar^2 k^2/(2m)$, but much of the interesting many-body physics (such as phonon excitations, or perhaps a roton, in the BEC) show up at low momentum. So, to create low-momentum Bragg excitations, we reduced the angle between our laser beams from 180° to 12°. To measure high-momentum Bragg excitations, one can measure atoms kicked out of the cloud or, alternatively, if the interactions are strong enough that atoms don't escape the cloud, the total momentum transfer to the cloud. However, with smaller momentum kicks, atoms that undergo a Bragg excitation can no longer be differentiated in time-of-flight expansion and the total momentum transferred to the cloud is much smaller and also very difficult to measure.

Therefore, we needed another technique to count the number of Bragg excitations, and so we looked at the light. The number of Bragg excitations is equal to the number of photons lost or gained by a Bragg beam. For our BEC of 50,000 atoms and for the small excitation regime, this signal is at most 10^4 photons, which corresponds to an optical power on the order of a pW. Measuring a small change in the power of an intense laser beam is technically challenging. Chapter 5 describes our shot-noise-limited photon counting technique for measuring the change in power of a laser beam due to Bragg excitations.

The photon counting technique was successful as a proof of principle, but there were a few

issues when we applied it to measuring low-momentum Bragg spectroscopy of a strongly interacting BEC. When performing Bragg spectroscopy, it is preferred to keep the number of excitations in the BEC small compared to the total number of particles and the number of absorbed photons from the beam small compared to the total number of photons. Neither of these conditions were true, though, if we maintained reasonable signal to noise in our measurement. Second, it was technically very difficult to control the pointing stability of the laser beam well enough. Lastly, a more fundamental problem was that the spectral width of the positive- and negative-going Bragg peaks were comparable to the separation of the signals. Thus, the two peaks would destructively interfere with each other, which stopped us from accurately measuring the peak position and width. This problem, unlike the previous challenges, was a fundamental challenge to this measurement and was going to be difficult to overcome. For these reasons we moved on to contact spectroscopy as a different probe of the interacting BEC.

4.3.2 Contact Spectroscopy and three-body contact

After developing the photon-counting Bragg-spectroscopy technique, we turned our attention to a new probe of interacting BECs and measured the contact (our measurement of the contact is in presented chapter 6). In 2008, Shina Tan published a number of seminal papers [54, 55, 56] describing a quantity called the contact. Tan showed that the contact is an extensive thermodynamic quantity of a Fermi gas that relates microscopic physics to thermodynamic quantities of the gas. The contact is related to a number of thermodynamic quantities, such as the pressure, the total energy, the momentum distribution, and the virial theorem, and to a number of microscopic quantities, such as the probability of two particles to be within a certain volume. Braaten *et al.* later extended the contact to bosons and to considering three particles instead of two [57]. To measure the contact in our lab, we used the fact that the contact is related to the amplitude of a long tail on one side of a RF lineshape [58, 59, 60].

We measured the contact for atomic bosons using RF spectroscopy and related it back to the total energy of the gas [19]. Our measurement of the contact is the first for atomic bosons

and we showed how the contact changes with scattering length. We explored the contact from the mean-field regime to the regime of beyond-mean-field interactions. Measuring the contact uses RF spectroscopy and allows us to quickly probe the BEC before losses occur. We apply an RF pulse for the contact measurement as soon as the magnetic fields are stable after changing a. We can pulse the RF field on for very short durations since we have large RF power and good coupling to the atoms. For very fast measurements, we are limited by the spectral Fourier width of the short pulse; however, the contact comes from the relative amplitude of the signal in the tail, which is less sensitive to broadening than a frequency measurement.

We made successful measurements of the contact due to two-body interactions. Braaten also predicted a contact signal proportional to three-body interactions in a BEC [57]. This three-body contact signal would be more apparent at smaller detunings on the excitation tail. So, to measure the three-body contact, we repeated the RF spectroscopy measurements, but with smaller detunings. Although we increased the interactions to as large as $na^3 = 0.002$, we saw no evidence of a three-body contact [19]. This was the largest na^3 we were able to ramp to before inelastic losses and density increases limited us. However, we can tune the scattering length to unitarity, where we saw preliminary evidence for a finite three-body contact.

4.4 Infinite interactions

4.4.1 Unitarity

Our Bragg spectroscopy and contact spectroscopy measurements were performed on a interacting BEC in the beyond-mean-field regime, but with na^3 still much less than one. The goal of studying strongly interacting BECs was stymied, since three-body losses caused the BEC to decay during the ramp from a weakly interacting BEC to a $na^3 > 1$ regime. Experiments studying interacting BECs could only reach "modestly strong" interactions [17, 15, 18, 61] with $na^3 < 0.008$. Alternatively, experimentalists used thermal Bose gases to explore $na^3 > 1$ with measurements of the three-body losses at unitarity [62, 63]. However, thermal gases aren't macroscopic quantum

systems where quantum mechanics and interactions determine the behavior of the gas.

We took a different approach to probe a strongly interacting BEC with $na^3 > 1$. Instead of ramping slowly compared to molecule binding energy, which is a minimum requirement for *local* equilibrium in the gas, we forsake equilibrium and quickly "jump" the scattering length. Our quick jump bypasses losses and projects the BEC on strong interactions. We measured the loss timescale and probed the dynamics of the system for short times compared to the timescale of the losses. To jump the interaction strength, we installed two small coils that quickly change the magnetic field. Chapter 3 described these fast-B coils.

Projecting a BEC onto unitarity raises many questions. If we consider the *local* physics, is an equilibrium of the many-body system reached before there is significant number loss? Does the system evolve coherently? Do losses dominate the system? *A priori* we don't know either the loss or many-body dynamics timescales. It becomes an experimental question to answer. We describe our measurements after fast projection of a BEC onto a strongly interacting state in chapter 6 and chapter 7.

4.4.2 Universality of physics at unitarity

As we increase the scattering length to where a diverges ($a \to \infty$), it can no longer be a physically relevant length scale. In the mean-field regime, the scattering length is an essential parameter in describing the gas. When $a \to \infty$, another physical length scale must effectively replace a. For a thermal gas, this could be the thermal de Broglie wavelength, but the de Broglie wavelength is not a relevant length scale for a BEC at zero temperature. The only length scale that remains is the distance between particles, which can be written in terms of the density as $n^{-1/3}$. The size of the cloud or the trap parameters can also provide a length scale; however, these are not intrinsic to a BEC. The length scale that remains is the distance between particles, so the degenerate Bose gas is universal in the sense all the physics is captured by the interparticle spacing. This means that energies scale as $n^{2/3}$, momenta as $n^{1/3}$, rates as $n^{2/3}$, and timescales as $n^{-2/3}$. We note that here we are ignoring any length scales due to three-body interactions (for example, the

size of an Efimov trimer could provide another length scale). Deviations from universal dependence of n due to three-body physics would be very interesting to observe.

The expected universality of the gas gives us reason to hope the losses may not dominate the system at unitarity. Naively, if the loss and equilibration rates scale as $\Gamma_{loss} \propto a^4$ and $\Gamma_{equilibrium} \propto a^2$, respectively, one would expect that the losses always dominate as $a \to \infty$. Instead, when we replace a with the interparticle spacing, all rates must scale as $\Gamma \propto n^{2/3}$. It is then an experimental question as to whether loss or equilibration is faster. For ^{85}Rb atoms, the previous experimental observation (figure 6.3 in chapter 6) of a relatively narrow, and therefore long-lived, Efimov resonance (characterized by a dimensionless width, $\eta \sim .06 \ll 1$) [19] is indicative that atoms close together do not decay instantaneously to deeply bound molecular states. As we see in chapter 7, equilibrium (or at least saturation of the dynamics) indeed appears to be faster by a factor of ten compared to the loss rate at unitarity.

Chapter 5

Photon counting for Bragg spectroscopy of quantum gases[1]

In this chapter we demonstrate a photon-counting technique for detecting Bragg excitation of an ultracold gas of atoms. As we explained in chapter 4, we use Bragg spectroscopy to probe a weakly interacting BEC. By measuring the response of the light field to the atoms, we derive a signal independent of traditional time-of-flight atom-imaging techniques. With heterodyne detection we achieve photon shot-noise limited detection of the amplification or depletion of one of the Bragg laser beams. Photon counting for Bragg spectroscopy is useful for strongly interacting gases where atom-imaging detection fails. In addition, this technique provides the ability to resolve the evolution of excitations as a function of pulse duration. However, we found probing low momentum excitations posed a challenge due to the positive and negative branches of the Bragg spectrum interfering with each other.

5.1 Introduction

Ultracold quantum gases provide clean, controllable model systems for exploring quantum many-body physics [3], and a powerful probe of these interacting quantum systems is the spectroscopy of low-energy excitations. For example, intriguing behaviors such as superfluidity, fermion pairing, and exotic weakly bound molecules can be revealed in their characteristic excitation spectra. In many cases, measured spectra can be directly compared with many-body theory to test our understanding of these rich systems.

[1] This chapter is an expanded version of a previously published paper [64]

Any experiment designed to probe excitations requires the same essential components: a way to excite the sample and a way to measure the response. To drive the excitations one applies a field to perturb the gas, and spectra are obtained by measuring the response of the ultracold gas as a function of the driving-field frequency. In ultracold atom experiments, this response is measured by imaging the atom cloud after the perturbation, and observing the response as some change in the density distribution of the imaged cloud.

There exists in any excitation spectroscopy, however, an alternative way to measure the response of the quantum gas to a driving field. Just as the quantum gas has responded to the probe field, the probe field must have an equivalent response to the quantum gas. In this chapter, we present a technique to measure this complementary information in Bragg spectroscopy by measuring the change in the number of photons in one of the laser fields used to drive the Bragg excitations. While in this work we use Bragg spectroscopy, this technique may more generally be applicable to other excitation spectroscopies as well [65]. For ultracold atoms where the number of atoms is typically small ($\sim 10^5$), the challenge, of course, is to have adequate signal-to-noise in measuring photon number to detect the Bragg response. For smallish atom samples, this will typically require a photon shot-noise limited measurement. To that end, we detail the experimental setup and the techniques of a heterodyne-based detection scheme used to realize shot-noise-limited photon counting. We also explore the advantages and limitations of this technique.

To motivate tackling the challenge of photon counting, we point out that this technique avoids some of the pitfalls inherent to spectroscopy measurements where the cloud is imaged. For example, strong interactions, which complicate the response seen in the density distribution of a Bose-Einstein condensate (BEC) [15], provide no additional complications for the photon counting approach. Indeed, a primary motivation for this work is our desire to extend Bragg spectroscopy of BEC to the case where we have both strong interactions and low momentum excitations. Finally, we present a powerful new feature of our technique, which is that we can directly probe the time evolution of the excitation process, even during the course of a single laser pulse.

5.2 Bragg Spectroscopy

Conceptually, a Bragg excitation can be thought of as a coherent scattering process involving absorption of a photon from one of the Bragg beams and stimulated emission into the other: a two-photon transition. It is this process of either absorption or emission that we aim to measure with our photon-counting technique. The process leaves the excited atoms in the same internal state, but with a new momentum, $\mathbf{k}$, determined by the geometry and wavelength of the Bragg beams. The two lasers have slightly different frequencies, to account for the energy of the excitation, and we vary this frequency difference, ω, for our spectroscopy.

Typically, the Bragg response is measured by looking at the cloud using time-of-flight atom imaging, where the gas is suddenly released from the trap and allowed to expand before imaging. Bragg excitations in a weakly interacting BEC then appear as atoms in a distinct cloud outside of the main cloud. The position of the new cloud, which is seen after the expansion from the trap, reflects the momentum of the excitation. This new cloud's density reflects the strength of the excitation. Pioneering studies of weakly interacting BECs have been done with such measurements [66, 67, 68], but, there are limitations. In particular, in the case of strong interparticle interactions [15, 69] or low-momentum excitations [68], the excitations no longer appear as a clearly distinguishable second cloud in the momentum-space image and the response becomes more difficult to quantify.

We show a measured Bragg lineshape for a weakly interacting ^{85}Rb BEC in figure 5.1. On the horizontal axis, we have the frequency difference between the two Bragg beams, which sets the energy of the Bragg excitation. On the vertical axis, we have the Bragg signal, namely, the number of excitations due to the Bragg process. We define this signal such that it can be either positive or negative, reflecting the direction of the momentum transfer. The number of excitations due to the Bragg pulse are counted in two different ways, and one can see that the photon counting and the time-of-flight imaging signals agree well with each other. The two sets of data were acquired simultaneously, with each cycle of the experiment providing both a photon-counting and an atom-imaging data point. This demonstrates the complementary nature of the two techniques. The lines

in figure 5.1 are individual fits of the Bragg spectrum to two Gaussian functions. These fits can be used to extract a center frequency and an RMS width. In the rest of this chapter we describe in detail the photon-counting technique demonstrated here.

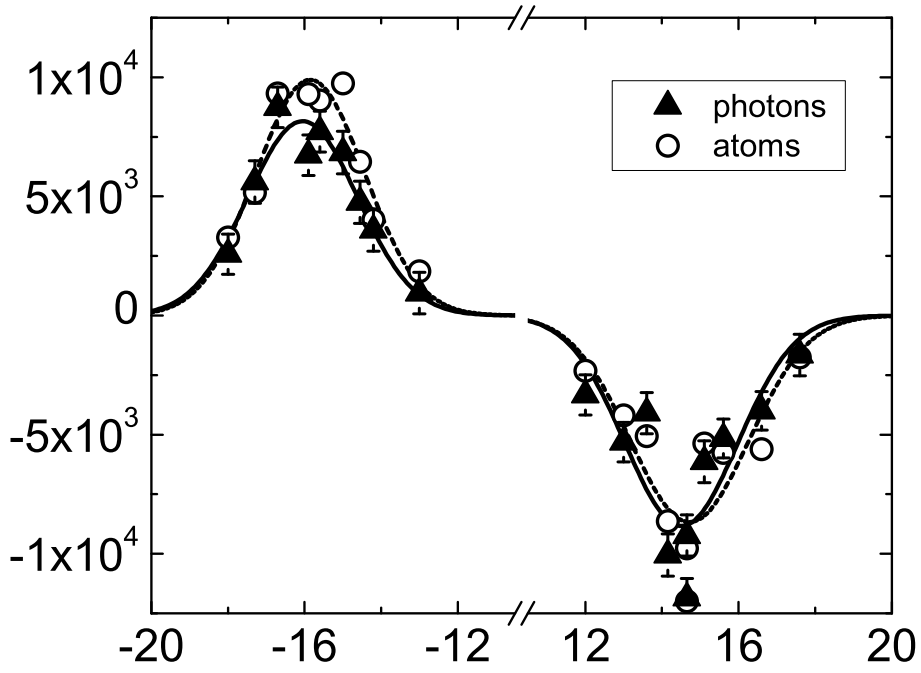

Figure 5.1: Bragg spectrum of a ^{85}Rb BEC of 5.5×10^4 atoms at $|\mathbf{k}| = 16\ \mu\text{m}^{-1}$, measured in two different ways. The horizontal axis shows the frequency difference between the Bragg beams. The vertical scale shows the number of excitations, which is measured using traditional absorption imaging of ejected atoms (hollow circles), as well as with the photon-counting technique presented here (black triangles). The error bars on black points represent the shot noise in the photon counting measurements. The photon counting measurements used three pulses of equal length. The first and the third pulses used only a single weak beam to make an average background measurement, with no Bragg excitation. During the second pulse, both Bragg beams illuminate the condensate to induce Bragg scattering and we subtract the averaged background to count the number of photons gained or lost in the weak beam due to the Bragg excitation.

A two-photon Rabi frequency characterizes the Bragg response and gives us an understanding of how the excitation rate will scale with the various experimental parameters. The two-photon

Rabi frequency is given by

$$\Omega_{\text{Bragg}} = \frac{\Omega_{\text{weak}}\Omega_{\text{strong}}}{2\Delta_{\text{int}}} \tag{5.1}$$

where Ω_{weak} and Ω_{strong} refer to the individual Rabi frequencies associated with each laser field, labeled here as weak and strong (the Bragg beam to be measured is the weak beam, for reasons that will be clear later). The detuning, Δ_{int}, in rad/s, refers to the detuning of the beams from the atomic transition, and is much larger than ω, the small frequency difference between the two beams. Using the Rabi frequency, we can define an excitation rate, $\Gamma(\omega)$ where

$$\int \Gamma(\omega)d\omega = \frac{\pi}{2}S(\mathbf{k})\Omega^2_{\text{Bragg}} \tag{5.2}$$

here $S(\mathbf{k})$ is the static structure factor, and gives the strength of the Bragg resonance for a particular $\mathbf{k}$. [70, 71].

In this paper, we describe photon counting detection for Bragg spectroscopy of BECs of Rb atoms. In our experiment, we can create nearly pure BECs of either ^{85}Rb or ^{87}Rb atoms, with a final number of roughly 4×10^4 or 4×10^5, respectively, in a roughly 10 Hz spherical magnetic trap. Thanks to a magnetic-field Feshbach resonance at 155 G, we can study strongly interacting condensates using ^{85}Rb atoms. The ^{87}Rb condensates, on the other hand, have far greater atom number and give us a robust tool for characterizing the photon-counting technique with an increased signal-to-noise ratio.

Regardless of the method used to measure a Bragg response, adequate signal-to-noise will always be a prerequisite. The signal is set by the number of Bragg excitations, which is typically less than 10% of the total atoms in the sample in order to probe the linear response. For our ^{85}Rb condensates, that would be some 4,000 excitations. If we allow for 10^5 photons in the weak beam, this corresponds to a signal-to-noise ratio (SNR) of only 9 on resonance. This assumes a detector with perfect quantum efficiency as well as a shot-noise limited detection scheme.

For the best signal-to-noise ratio, assuming that a shot-noise limited measurement is available, we look to minimize the total number of photons in the weak beam. Keeping the excitation rate (and hence the signal) constant when decreasing the intensity of the weak beam necessitates increasing

the intensity of the strong beam (see equation 5.2). However, single-photon processes, namely off-resonant scattering of the stronger beam, limit the maximum permissible intensity in the strong beam, and this, in turn, limits the minimum intensity in the weak beam for a desired excitation rate. Note that having a large mismatch between the two Bragg beam intensities is a distinct requirement for photon counting compared to the usual atom-response detection, where there is no reason not to have equal intensities in the two beams.

Another limit to the minimum photon number in the weak beam is set by the spatial profile of the weak beam at the atoms. We tailor this spatial profile by focussing the weak beam onto the atoms, attempting to match the transverse spatial profile of the weak beam to that of the condensate in order to minimize the number of photons that would never interact with the condensate, and only add to the shot-noise of the measurement. In minimizing the number of weak beam photons, one could easily enter a regime where the number of Bragg photons scattered is a significant fraction of the weak beam photons themselves. In this regime, the transverse spatial profile of the weak beam intensity would be modified due to the scattering of Bragg photons out of (or into) the weak beam; this could, in effect, burn a "hole" in the probe. We describe these as propagation effects and, to simplify the interpretation of the Bragg response, we keep the total number of photons in the region of overlap between the weak beam and the BEC large compared to the number of excitations. This provides another limit on the minimum number of weak beam photons and, therefore, the maximum signal-to-noise ratio for the measurement.

In order to then make shot-noise limited measurements of the weak light, one could consider using detectors with integrated cascading amplification, such as avalanche photodiodes and photo multiplier tubes. However, in considering this option for our purposes, we found that avalanche photodetectors suffer from pulse-pileup for the powers we use, while photo multiplier tubes suffer from low quantum efficiencies in the IR, which at 5% or so are too low to be useful. Therefore we consider the alternative of using detectors in their linear mode of detection. Silicon photodetectors have quantum efficiencies as high as 90% and capacitances on the order of 3 pF. However, for the pulse lengths we seek ($\sim$ 1 ms) the Johnson noise associated with the necessary feedback resistor

corresponds to the shot noise of a 1 μW beam at 780 nm and therefore makes direct shot-noise-limited measurements impossible for the powers used in these experiments. Our solution to these challenges is one as old as the AM radio: heterodyning.

5.3 Heterodyne detection

To motivate heterodyne detection, we consider the following scheme. We direct the weak Bragg beam onto a photodiode, and after some stages of amplification, directly measure a voltage, S_{direct}, proportional to the number of photons per second incident on the detector. To illustrate the role of shot-noise, we consider our signal to be proportional to the number of photons, N_{weak}, that hit the detector in some time τ. In terms of an average voltage, the signal is $S_{\text{direct}} = eR\eta N_{\text{weak}}/\tau$, where η is the quantum efficiency of the detector, e is the charge of an electron, and R is the transimpedance gain of the amplifier.

The signal-to-noise ratio, SNR_{direct}, on this direct weak beam detection is given by

$$SNR_{\text{direct}} = \frac{eR\eta N_{\text{weak}}/\tau}{\sqrt{\delta_{\text{S}}^2 + \delta_{\text{e}}^2}} \tag{5.3}$$

where the shot-noise associated with the photocurrent is $\delta_S = (eR/\tau)\sqrt{\eta N_{\text{weak}}}$. Other sources of noise (dark noise from the detector, Johnson noise introduced in the amplification stages, noise on background light incident on the detector, etc.) will be referred to as electronic noise, and are represented by δ_e. Shot-noise limited detection is defined as the regime where δ_e is an insignificant contribution to the total noise ($\delta_e \ll \delta_S$). In this case,

$$SNR_{\text{shot-noise}} = \sqrt{\eta N_{\text{weak}}}. \tag{5.4}$$

This is difficult to achieve in direct detection, where for typical experimental values of $\tau = 1$ ms, $N_{\text{weak}} = 10^5$, $\eta = 85$ %, we might expect $\delta_e = 1000 \times \delta_S$ for a silicon photodetectors with a high bandwidth, low-noise transimpedance preamplifier.

We use a heterodyne scheme to overcome these difficulties. The idea of heterodyne detection is to amplify the signal *optically* before detection, so that electronic noise is of no consequence. We

do this by measuring the beat of the weak beam against another, more intense beam, which we will refer to as the local oscillator (LO). Because the beat signal, S_{beat}, goes as the square root of the product of the intensities of the weak and the LO beam, we are left with a signal that is much stronger than that of the original, weak beam signal.

The advantage heterodyne offers is that one may arbitrarily increase the intensity of the LO beam, so that the shot-noise from the LO photons dominates the electronic noise, and the total noise is given by

$$\sqrt{\delta_S^2 + \delta_e^2} \simeq \delta_S = (eR/\tau)\sqrt{\eta N_{\text{LO}}} \tag{5.5}$$

where N_{LO} is the number of photons from the LO beam during a time τ. Because increasing the LO beam intensity also increases the optical gain, we are left with a SNR on N_{weak} using heterodyne detection as

$$SNR_{\text{hetero}} = \mathcal{C}\sqrt{\eta N_{\text{weak}}} \tag{5.6}$$

where the contrast, $\mathcal{C}$, is a number between zero and one that describes the quality of the mode-matching between the two heterodyne beams. One notes that for perfect contrast ($\mathcal{C} = 1$), SNR_{hetero} is our stated goal for a shot-noise limited measurement as in equation 5.4. These principles of optical heterodyning are well established, and we refer the reader to Refs. [72, 73, 74] for a more thorough discussion.

Measurements of the LO shot-noise, δ_s, also serves to calibrate the overall gain of our system, R. Provided one knows η (which is readily available from the photodiode's datasheet) and has a calibration for N_{LO} (which is straightforward for the relatively high power of the LO beam), one can rewrite equation 5.5 as

$$R = \delta_S \frac{(\tau/e)}{\sqrt{\eta N_{\text{LO}}}}. \tag{5.7}$$

5.4 Optical Layout and Electronics

While the principle behind shot-noise limited heterodyne detection is straightforward, the implementation of such a technique has a number of subtleties, which we lay out here. We illustrate both the optical and the RF design in figure 5.2. We begin our discussion on the optical side of things, and then consider the RF.

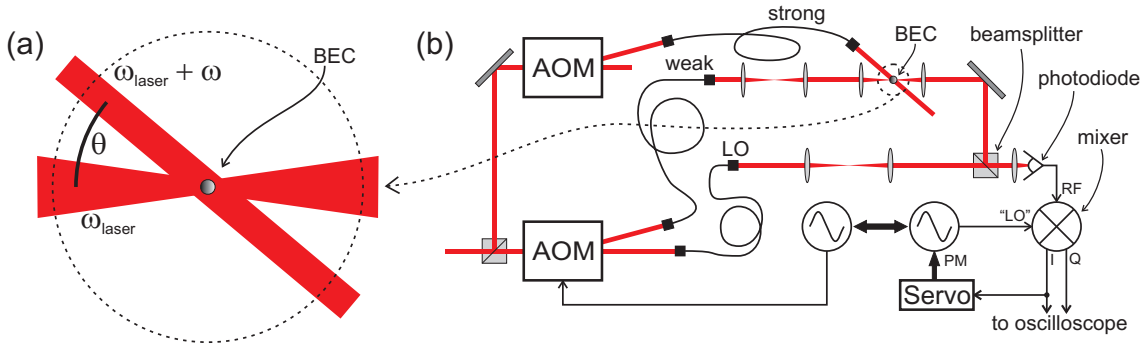

Figure 5.2: Diagram of the Bragg beams (a) and the heterodyne setup for Bragg scattering via photon counting (b). The Bragg beam frequencies ($\omega_{\text{laser}}, \omega_{\text{laser}} + \omega$) are offset by ω, and create excitations at momentum $\hbar k = 2\hbar k_{\text{laser}} \sin(\theta/2)$, where θ is the angle between the Bragg beams and $k_{\text{laser}} = 2\pi/780$ nm in our case. In (b) the three beams (labeled weak, LO and strong) are derived from the same laser source and individually fiber coupled. The optics for the LO beam are chosen to give the same spatial mode as that of the weak beam. After being combined on a beamsplitter, the weak and LO beams illuminate a photodiode and the beat signal is sent to a demodulating mixer. The two quadrature outputs of the demodulator, I and Q, are sent to an oscilloscope for the measurement. Also illustrated in the figure is a servo loop that functions to minimize the phase fluctuations of the RF input with respect to the "LO" drive of the mixer. The servo minimizes the demodulator output, I, by feeding back to a phase modulation input on the synthesizer that drives the "LO" port of the mixer. This synthesizer is phase-locked to the synthesizer driving the weak beam acousto-optic modulator (AOM), illustrated with a double-headed arrow. Not shown in the schematic is the synthesizer driving the strong-beam AOM, which is also phase referenced to the synthesizer driving the weak-beam AOM.

In figure 5.2(a), we show the two Bragg beams intersecting at the location of the BEC. The third, much more intense LO beam, shown in figure 5.2(b), functions only to amplify the weak beam for our heterodyne detection, and avoids the atoms altogether. All three beams are derived from the same laser, and are offset in frequency after passing through acousto-optical modulators (AOM). For these experiments we use a diode laser at 780 nm with a coherence length on order of

100 m. Each AOM has a dedicated synthesizer, with an additional synthesizer driving the mixer as well. All three of these synthesizers are phase-locked to each other to ensure coherence between the Bragg beams.

There are two challenges in optimizing this heterodyne interferometer for shot-noise limited detection. The first is achieving a contrast, $\mathcal{C}$, as close to unity as possible. In equation 5.6, we see that the signal-to-noise ratio scales linearly with the contrast. Therefore, we would like the best possible mode-matching between the two beams, both spatially as well as in terms of polarization. In light of these two requirements, we launch the two beams into polarization-maintaining fibers identical in both core sizes and output couplers. The weak and the LO beams subsequently pass through different sets of lenses, which serve to match the focussed size of the weak beam to the size of the BEC, as well as to match the spatial mode of the LO beam to that of the weak when they recombine on the beamsplitter. To avoid interactions between the intense LO light and the atoms, the LO beam has its own optical path that avoids the vacuum chamber and the atoms. In addition, we have an optical isolator (not shown in figure) in between the beamsplitter and the photodiode to extinguish LO light backreflections off of the photodiode that interact with the atoms.

The second challenge is to minimize any jitter in the relative phase (ϕ) between the two beams. As we will see later, this phase jitter introduces noise that limits us from achieving shot-noise limited detection for longer Bragg pulses. We find that the biggest source of instability in the relative phase is due to the optical fibers. These fibers are sensitive to mechanical vibrations and acoustical noise. We thus use relatively short fibers (1 m) to minimize phase jitter between the two beams, while still providing the necessary filtering of the spatial mode.

Combining the two beams with a beamsplitter provides good spatial overlap, at the cost of weak beam attenuation from light lost at the unused beamsplitter port. This can be included in equation 5.6, by simply replacing η with a lower effective quantum efficiency for the detection system. For the best signal-to-noise ratio, we would like to measure as much of the weak beam as possible. This must be balanced, however, with our need for large enough LO power to overwhelm the electronic noise. Typically, we work with 90% reflection of the weak beam and 10% transmission

of the LO beam, corresponding to 250 μW of LO power on the photodiode. This 90/10 ratio is achieved with a partially reflective, gold-coated piece of glass.

To measure and maximize the contrast, we replace the light launched into the weak beam fiber with light at the same frequency and intensity as the LO. With this homodyne interferometer, one can easily assess the quality of the contrast by eye, by looking at the pattern of the interference fringes at the photodiode. Our procedure is to first align the beam such that the fringes (seen using a temporary lens to expand the beam) are a circular pattern of rings. We then optimize the collimation of the LO beam by minimizing the total number of rings seen. We found this to be an essential step in getting good contrast. Once the beams are closely mode matched by eye, we perform the final steps of alignment by directly monitoring the DC output of the photodetector. We found it useful to modulate the phase of one of the beams (achieved via a moving plate of glass in one of the beam paths), enough to wrap around 2π, so that the DC output swings between fully constructive ($\mathrm{DC_{max}}$) and fully destructive ($\mathrm{DC_{min}}$) interference. We are able to quantify the contrast through

$$\mathcal{C} = \frac{\mathrm{DC_{max}} - \mathrm{DC_{min}}}{\mathrm{DC_{max}} + \mathrm{DC_{min}}}, \tag{5.8}$$

true when the intensities of the two beams are the same.

We also take steps to minimize the electronic noise (δ_e) that the LO's shot-noise must overcome. The relevant noise for the heterodyne measurement is that at the frequency of the beat note, Δ_{LO}. Our photodiode circuit is designed to minimize the effects of inherent voltage noise at the op-amp input at this frequency ($2\pi \times 70$ MHz) by way of a standard "tank" circuit. The tank circuit consists of an inductor between the op-amp input and ground. The inductance is chosen so that when the photodiodes's internal capacitance is also considered the two make a resonant LC circuit at Δ_{LO}. We are able to reduce the receiver (photodiode plus amplifier [75]) dark noise to 2 pA/$\sqrt{\mathrm{Hz}}$ which is typical for most commercially available transimpedance amplifiers. The subsequent stages of amplification are chosen so that the noise they add is small compared to that introduced in this first stage of amplification.

The voltage from the photodetector then goes to an RF mixer. As shown in figure 5.2(b), the mixer is a four-terminal device, called an I,Q-Demodulator; this is essentially two mixers in one, with the RF input split between the two. Port I is the same as the IF (intermediate frequency) output of a standard mixer, while the Q port is the output of a second mixer whose "LO" drive has a phase offset 90 degrees with respect to the phase of the I port's "LO" drive. In our application, the outputs of the demodulator have the form

$$S_I = (2\mathcal{C}eR\eta/\tau)\sqrt{N_{\rm LO}N_{\rm weak}}\cos\phi \tag{5.9}$$

$$S_Q = (2\mathcal{C}eR\eta/\tau)\sqrt{N_{\rm LO}N_{\rm weak}}\sin\phi \tag{5.10}$$

By summing the squares of S_I and S_Q, we are able to measure the amplitude of the beat signal, regardless of the relative phase ϕ. For a known LO beam power, $\propto N_{\rm LO}/\tau$, our signal is directly proportional to the rate of weak beam photons, $\dot{n} = N_{\rm weak}/\tau$. We measure S_I and S_Q with a digitizing oscilloscope and perform the sum in subsequent software analysis.

While we now have a signal that in principle is insensitive to the relative phase ϕ between the weak beam and the LO beam, the demodulator is imperfect, due to non-linearities and voltage offsets in the I and Q outputs as well as deviations from perfect 90 degree phase offset. We therefore servo the phase of the RF driving the "LO" port of the demodulator, as illustrated in figure 5.2(b). The servo minimizes S_I by actively feeding back to the phase-modulation input of the relevant synthesizer, and this reduces the sensitivity of the quadrature sum to demodulation imperfections.

5.5 Noise performance and Bragg dynamics

In figure 5.3, we present data illustrating the shot-noise limited performance of our heterodyne detection. We calculate the noise by measuring the standard deviation, σ_Δ, of the difference in photon number, Δ_i, for M consecutive Bragg pulses of equal length,

$$\sigma_\Delta = \sqrt{\sum_{i=1}^{M-1}\frac{(\Delta_i - \bar{\Delta})^2}{M-1}} \tag{5.11}$$

where $\Delta_i = N_{\mathrm{weak}_{i+1}} - N_{\mathrm{weak}_i}$, and N_{weak_i} is the measured number of photons in the weak beam for pulse i. Since on average the difference should be zero ($\bar{\Delta} = 0$), and we know that the standard deviation in photon number, $\sigma = \sigma_\Delta/\sqrt{2}$, we are left with

$$\sigma = \frac{1}{\sqrt{2}}\sqrt{\sum_{i=1}^{M-1} \frac{\left(N_{\mathrm{weak}_{i+1}} - N_{\mathrm{weak}_i}\right)^2}{M-1}}. \tag{5.12}$$

We plot the noise on our measurements of weak beam photon number, normalized to the expected shot-noise ($\delta_{\mathrm{shot}} = \sqrt{\eta N_{\mathrm{weak}}}$) for that particular pulse duration and laser power, as a function of the duration of a fixed intensity pulse. In the inset of the figure, we plot the same noise measurement for the case where the weak beam intensity is varied to keep the total number of photons fixed at a constant 10^5.

For a large range of pulse durations, the measurement is at, or within a factor of two of, the shot-noise limit. For pulses shorter than 1 μs the noise is artificially low due to an inline, low-pass filter. The increased noise at longer timescales sets an upper limit to the time available for our Bragg measurements and is probably caused by residual phase drift in our system. Servoing the laser power provided no significant improvement in the noise performance of our heterodyne detection.

A potentially useful feature of a photon-counting measurement is the ability to measure the dynamics of Bragg excitations during a single laser pulse. We demonstrate this capability in figure 5.4, where we plot the number of excitations, N_{exc}, as a function of time, τ. The data were taken using a condensate of 400,000 ^{87}Rb atoms, with the Bragg detuning set to be on resonance with the measured Bragg transition at $\omega = 2\pi \times 250$ Hz for a momentum transfer given by $k = 1.5\ \mu\mathrm{m}^{-1}$. For Fourier-limited pulses we expect $N_{\mathrm{exc}}(\tau)$ to go initially as τ^2, however an interesting feature illustrated in figure 5.4 is the suppression of $N_{\mathrm{exc}}(\tau)$ for pulses short compared to the inverse Bragg resonance, $\tau < \omega^{-1} = 0.3$ ms. For these short pulses, the associated energy uncertainty makes it impossible to resolve a $+k$ excitation from a $-k$ excitation. Photon emission from the one process cancels photon absorption from the other process. In our experiments, we did not observe Rabi flopping in the time-dependent data, which may be due to dephasing. For the measurements here,

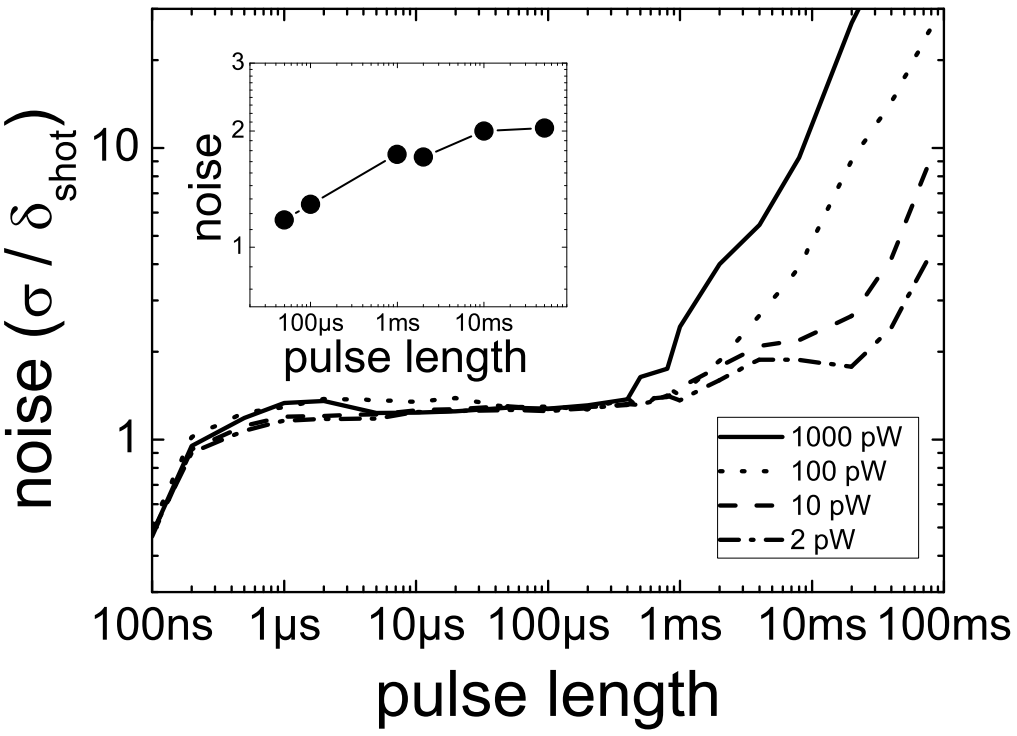

Figure 5.3: Noise performance of heterodyne detection for a LO power of 250 μW. Vertical scale is normalized to the shot-noise expected for the relevant pulse length and laser power. The legend shows the different weak beam powers used. Low-frequency drifts make our heterodyne scheme no longer shot-noise limited at long timescales. Inset has the same normalized vertical units, with the data shown at different weak beam intensities, corresponding to a constant 10^5 photons.

the weak beam profile used was much smaller (7 μm $1/e^2$ waist) than that of the BEC (22 μm Thomas-Fermi radius), which complicates the Bragg response. We present this data, however, to illustrate a promising feature only available with a photon-counting approach.

5.6 Conclusion

We have demonstrated photon counting as a viable technique for Bragg spectroscopy in ultracold atoms. By measuring the response of the driving field to the atoms, one has a measurement independent of, and complementary to, the traditional atom cloud time-of-flight imaging. Our

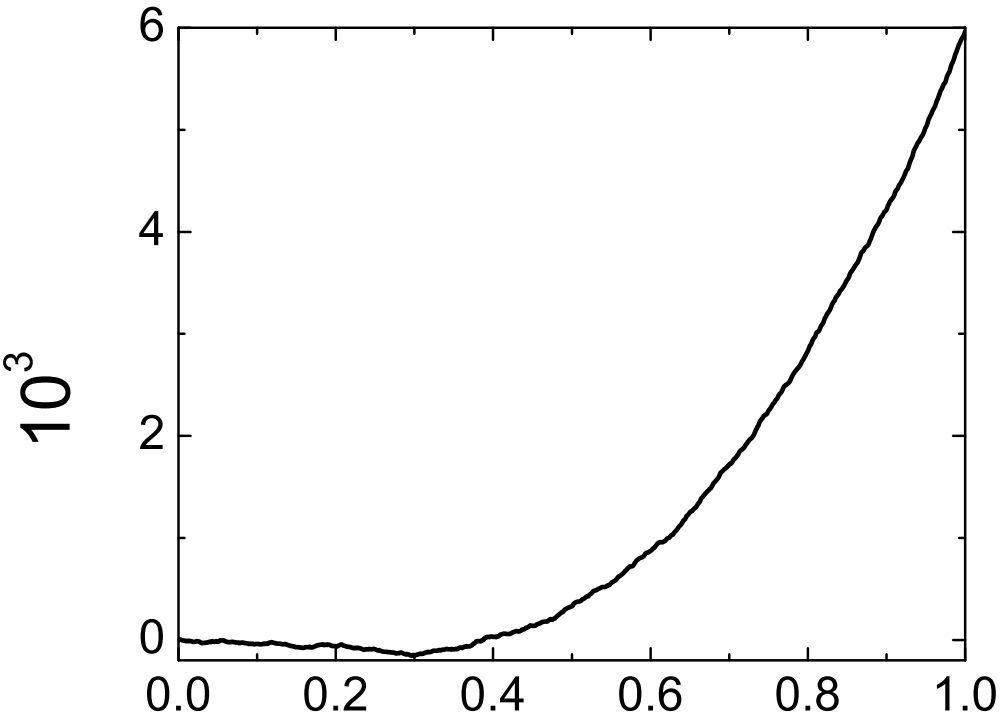

Figure 5.4: Bragg excitations as a function of time, measured with photon counting. The number of Bragg excitations is given by $N_{\rm exc}(\tau) = \int_0^\tau (\dot{n}(t) - \dot{n}_{\rm avg})dt$, where $\dot{n}_{\rm avg}$ is the average rate of weak beam photons measured when no strong light is present. The Bragg pulse begins at 0 ms. The deviation from expected τ^2 behavior (for small τ) is discussed in the text. These measurements were performed on resonance, with a BEC of 400,000 ^{87}Rb atoms.

heterodyne scheme approaches shot-noise limited detection of a weak Bragg beam, which then allows us to measure the number of photons added to, or depleted from, that beam. We have shown that this measurement technique can be used simultaneously with time-of-flight imaging, and that it can probe the time dependence of the excitation process.

There are several issues to consider in applying photon-counting for Bragg spectroscopy of a BEC. Because the weak Bragg beam waist needs to be roughly matched to the transverse profile of the condensate, careful alignment must be maintained for the photon counting approach. In

addition, Bragg spectroscopy for small momentum transfers can be complicated by the fact that the upward and downward portions of the lineshapes (see in figure 5.1) can begin to merge for Bragg frequencies near zero. Determining a resonant frequency from fits to these slightly merged lineshapes is nontrivial (in particular the fitting parameters, line widths and line center, are no longer orthogonal), and, as a result, greater signal-to-noise is needed. We have also observed asymmetries between the upward and downward portions of Bragg lineshapes taken with photon counting, which we attribute to the relatively small number of N_{weak} photons necessitated by the photon counting approach. We speculate that these asymmetries are related to the propagation effects (for instance difficult-to-model effects associated with spatial variations in the Rabi frequency as the beam propagates through the sample), or nonlinearities, inherent in a weak beam that has been significantly enhanced or depleted by the Bragg process. These effects will be strongest when the number of Bragg photons is a significant fraction of N_{weak}, or of the number of atoms in the condensate. These issues may limit the usefulness of this technique to systems whose atom number is larger than the 40,000 atoms in our ^{85}Rb BECs.

Measurements of the scattered Bragg photons could open the doors to new investigations of the temperature-dependent structure factor, as proposed by Stamper-Kurn [76]. More generally, this technique of measuring the probe in order to detect atom-light interactions could be applied to other types of ultracold atom spectroscopy as well, and it seems that the two technologies, photon counting and time-of-flight imaging, marry nicely.

Chapter 6

The contact [1]

A powerful set of universal relations, centered on a quantity called the contact, connects the strength of short-range two-body correlations to the thermodynamics of a many-body system with zero-range interactions. In this chapter we discuss measurements of the contact for an ^{85}Rb atomic Bose-Einstein condensate (BEC) using RF spectroscopy and loss measurements of the BEC. For bosons, the fact that contact spectroscopy can be used to probe the gas on short timescales is useful given the decreasing stability of BECs with increasing interactions. A complication is the added possibility, for bosons, of three-body interactions. The different functional form predicted for the RF lineshape due to two-body interactions compared to three-body interactions allowed us to differentiate between the two. In our investigations, we also located an Efimov resonance for ^{85}Rb atoms with loss measurements and thus determined the three-body interaction parameter.

Systems with strong quantum correlations represent a frontier in our understanding of the complex quantum systems found in nature. Atomic Bose-Einstein condensates (BEC) provide a versatile system in which to explore beyond mean-field physics. Ultracold atoms experience two-body, short-range interactions that are well described theoretically by a delta-function pseudopotential characterized by an s-wave scattering length a. In the simplest BEC experiments the values of a and of the density n are such that interactions are too weak, compared to the kinetic energy cost of correlations, to take the gas out of the mean-field regime. In many experiments an additional lattice potential is applied to suppress the kinetic costs and thus turn on interesting correlations.

[1] Much of this chapter appeared in a previously published paper[19]

The external lattice, however, imposes an artificial orderliness not found in bosons in the wild. To explore strong interactions in a more naturalistic bulk three-dimensional gas, one can increase a by means of a magnetic-field-tunable Feshbach scattering resonance [5]. Such efforts are motivated for instance by a desire to make better conceptual connections to the iconic strongly correlated fluid, liquid helium.

In practice it has proven difficult to study atomic BEC with increasing a and only a few experiments have measured beyond-mean-field interaction effects [15, 17, 18]. The problem is that higher a is accompanied by a dramatic increase in the rate of inelastic three-body processes [23, 22]. This leads to large losses and significant heating of the trapped gas on a timescale similar to that for global equilibrium of the trapped cloud. Probes of the gas that require global equilibrium, such as measurements of the density distribution or the amplitude or frequency of collective density oscillations in a trap, are therefore limited to systems that are only modestly out of the mean-field regime. Our strategy for exploring BEC with larger interaction strengths is to start from an equilibrated weakly interacting gas, change the interaction strength relatively quickly, forsaking global equilibrium, and then use a fast probing technique to look at *local* many-body equilibrium (as described in chapter 4) in the trapped gas [15]. We show how RF contact spectroscopy is a fast probe of short-range correlations in a weakly interacting BEC, before presenting measurements of the contact for a strongly interacting BEC at unitarity.

6.1 Introduction to the contact

A central challenge in many-body physics lies in elucidating the dependence of an interacting many-body system on the strength of the few-body interactions. For ultracold Fermi gases, it has been shown that the dependence of the energy on a can be connected to the strength of two-particle short-range correlations through a set of universal relations that were introduced by Shina Tan [54, 55, 56]. These universal relations, which involve a quantity termed the "contact" hold true for any locally equilibrated gas regardless of the temperature, interaction strength, or number of particles. Tan's predictions have been explored theoretically [77, 78, 79, 80, 81, 82] and verified

experimentally [83, 84] for strongly interacting Fermi gasses. Recently, a number of theoretical papers have discussed extending the ideas of the "contact" to bosons [85, 57, 86, 87]. We now address experimentally whether contact spectroscopy can be used to probe interacting bosons.

The derivation of Tan's universal relations does not depend directly on the quantum statistics of the particles, however, it does assume that the interactions are fully described by a single parameter, a. While this is true for an ultracold two-component (spin-up and spin-down) Fermi gas, it is in general not true for a Bose gas, where three-body interactions give rise to Efimov resonances [26]. A number of recent experiments probing few-body physics in ultracold Bose gases have observed Efimov resonances [88, 89, 90, 16, 91], however, many-body effects of the three-body interactions have not been observed. To explore contact spectroscopy for bosons, we begin by examining RF spectroscopy assuming that three-body interactions do not significantly affect this measurement. Following this, we present a measurement of the three-body parameter for ^{85}Rb using trap loss rates for a non-condensed gas, and then look for many-body effects manifested in a three-body contact for a BEC, C_3 [57, 92].

The two-body contact, C_2, is an extensive thermodynamic variable that is connected to the derivative of the total energy of the system, E, with respect to a [55, 85, 86].

$$\left.\frac{dE}{da}\right|_s = \frac{\hbar^2}{8\pi m a^2} C_2. \tag{6.1}$$

Combining this with the energy density of a BEC (equation 2.7) in the perturbative beyond-mean-field regime the predicted contact for a condensate is

$$C_2 = 16\pi^2 n a^2 \left(1 + \frac{5}{2}\frac{128}{15\sqrt{\pi}}\sqrt{na^3} + ...\right) N_0, \tag{6.2}$$

where n is the atom number density, m is the atomic mass, and N_0 is the number of atoms in the BEC.

To measure C_2 using RF spectroscopy [58, 59], an RF pulse drives a Zeeman transition and transfers a small fraction of spin-polarized bosonic atoms into another spin state. Interactions give rise to an asymmetric tail in the RF spectrum, which can be thought as RF "dissociation"

of pairs of atoms that happen to be very close to each other. Ignoring C_3, and assuming that the measurement is done in the linear regime, the rate for transferring atoms to the final spin state in this tail is given by [60]

$$\lim_{\omega\to\infty}\Gamma(\omega) = \frac{\Omega^2}{4\pi}\sqrt{\frac{\hbar}{m}}\frac{\alpha(a)}{\beta(\omega)}\frac{C_2}{\omega^{3/2}}, \tag{6.3}$$

where $\int_{-\infty}^{\infty}\Gamma(\omega)d\omega = \pi\Omega^2 N$, Ω is the Rabi frequency, and N is the total number of atoms. In Eqn. 6.3, $\alpha(a)/\beta(\omega)$ describe final-state effects; the a-dependent part is $\alpha(a) = (a'/a - 1)^2$, where a' is the scattering length for interactions between atoms in the final spin state and atoms in the initial spin state, while the frequency-dependent part is $\beta(\omega) = 1 + \hbar|\omega|/E'$, where $E' = \hbar^2/ma'^2$.

Our experiments probed 4-8$\times 10^4$ Bose-condensed ^{85}Rb atoms in a gas with a 60% condensate fraction. The atoms are in the $|F = 2, m_F = -2\rangle$ state, where F is the total atomic spin and m_F is the spin projection. They are confined magnetically in a 10 Hz spherical harmonic trap with a variable magnetic bias field. We work at magnetic-field values near a Feshbach resonance at 155.04 G [10], and during the final stages of evaporation, the field is set to give $a \sim$100 a_0. After evaporation, we ramp the bias field in order to change a on a timescale that is fast compared to the trap period, but adiabatic with respect to two-body timescales, with $\dot{a}/a$ never reaching more than $0.01\hbar/(ma^2)$ ($\dot{a}$ being the time derivative of a) [93].

An example of RF contact spectroscopy at $a = 497 \pm 5$ a_0, where a_0 is the Bohr radius, is shown in figure 6.1a. Roughly 1 ms after the magnetic-field ramps, we probe the BEC using a Gaussian envelope RF pulse to drive the $|2, -2\rangle$ to $|2, -1\rangle$ transition. We determine $\Gamma(\omega)$ from the number of atoms transferred to the $|2, -1\rangle$ spin state divided by the RF pulse duration. We then define our signal, $S(\omega)$, as $\Gamma(\omega)$ normalized by the integrated lineshape. We fit $S(\omega)$ to a Gaussian lineshape (dashed black line in figure 6.1a) and take the center to be the single-particle transition frequency ω_0. The center of the RF lineshape will be shifted due to mean-field interactions by an amount typically less than $2\pi \times 0.5$ kHz. For the main lineshape, we use short RF pulses with a Gaussian rms width for the field amplitude, τ, of 5 μs; this sets the observed width of the lineshape. At larger detunings, we use longer pulses, with an rms width of 25 to 200 μs, and an increased RF

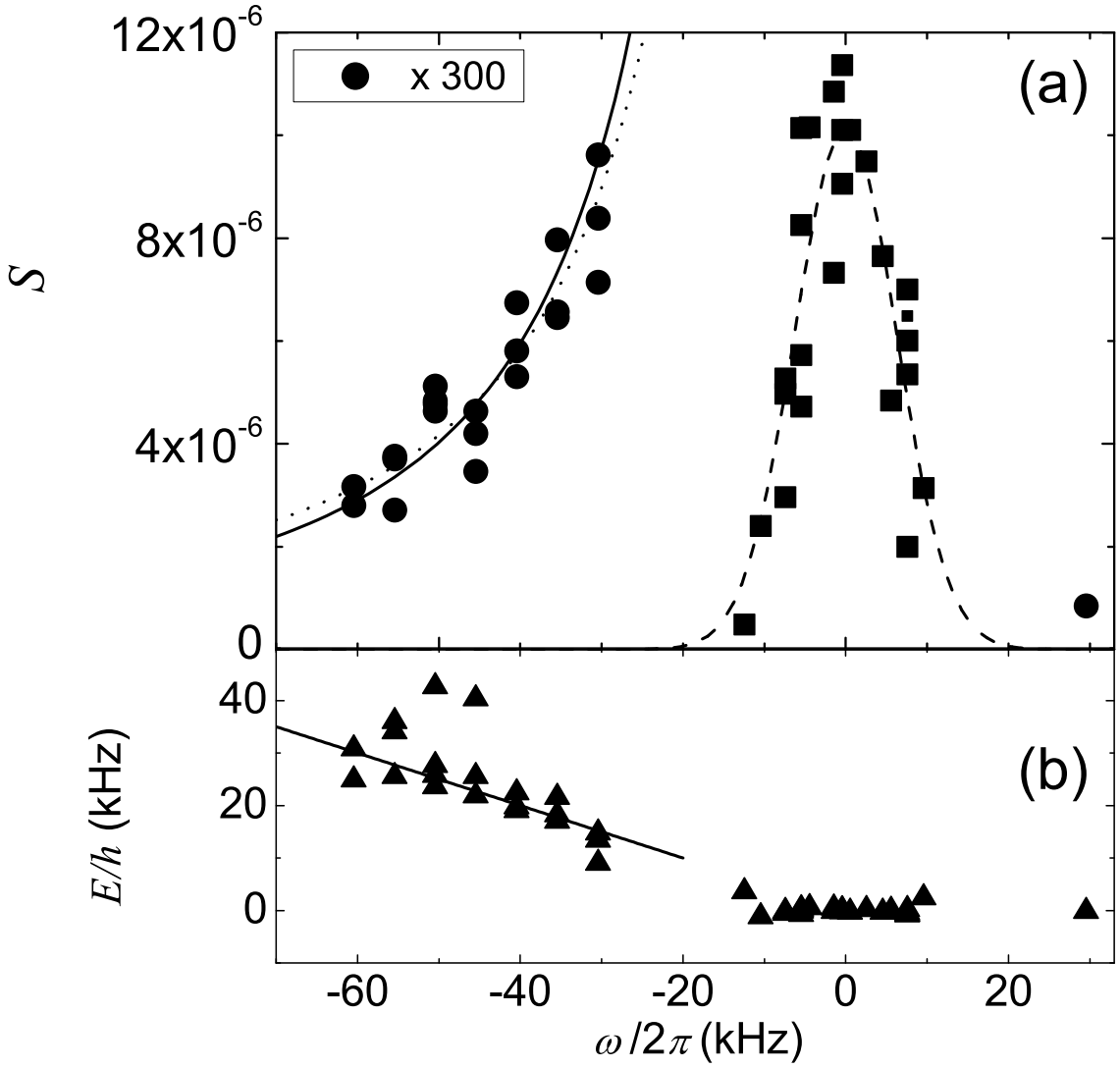

Figure 6.1: Example of RF contact spectroscopy. (a) RF lineshape, $S(\omega)$, normalized so that $\int_{-\infty}^{\infty} S(\omega)d\omega = 1$ s^{-1}. The data at large detunings (circles) are multiplied by a factor of 300 to make the tail visible. Here the mean BEC density is $\langle n \rangle = 4.9$ x10^{12} cm^{-3}. (b) Additional release energy of the outcoupled atom cloud. We calculate the energy from the width of the expanded cloud, σ, using $E = \frac{3}{2} m \frac{\sigma^2 - \sigma_0^2}{\Delta t^2}$, where Δt is the time between the middle of the RF pulse and the absorption image (4.5 ms) and σ_0 is the size of the expanded cloud measured at $\omega = 0$. The solid line is $\frac{1}{2}\frac{|\omega|}{2\pi}$.

power, Ω^2, such that we outcouple 1-2% of the gas. We normalize the signal for the different τ and Ω^2, making small (5%) corrections for measured nonlinearity in $\Omega^2\tau$.

For our experiment, the RF drives a transition to a lower energy spin state and one expects the $1/|\omega|^{3/2}$ interaction-induced tail on the low frequency side of the lineshape. Consistent with this expectation, we observe a tail for large negative detunings, while for similar detunings on the positive side, we find that the signal is consistent with zero. The solid line in figure 6.1a shows a fit to the expected frequency dependence from Eqn. 6.3, while the dotted line shows a fit to $1/|\omega|^{3/2}$. For our system, the final-state effects are characterized by $a' = -565\ a_0$ [94] and E'/h =133 kHz.

The $1/|\omega|^{3/2}$ tail, due to the contact, corresponds to an expected $1/k^4$ tail in the momentum distribution $n(k)$ [60, 84]. In figure 6.1b, we show the expansion energy of the outcoupled atoms, measured by releasing the gas from the trap and imaging the cloud after 3 ms of expansion. In the region of the observed tail our data show good agreement with the prediction (line in figure 6.1b) that the additional release energy should be $\frac{1}{2}\hbar|\omega|$, where the factor of $\frac{1}{2}$ comes from the assumption that the excess energy of the RF photon is shared between two pairwise interacting atoms [95].

The strength of the RF tail is shown as a function of a in figure 6.2. As expected, we see the strength of the RF tail increase as a increases. In comparison with theory, our contact measurements are larger than the mean-field prediction (solid line in figure 6.2), but not as large as the prediction including the next order LHY term given in Eqn. 6.2 (dashed line in figure 6.2). While beyond-mean-field physics is evident in the contact data shown here, we see evidence that the measured strength of the RF tail depends on the speed of the magnetic-field ramp to increase a, with C_2 increasing for slower ramps. We plan to carefully explore this intriguing dependence on ramp speed in order to probe experimentally local microscopic *dynamics* in the beyond mean-field regime.

We now turn our attention to C_3, which is connected to the derivative of E with respect to

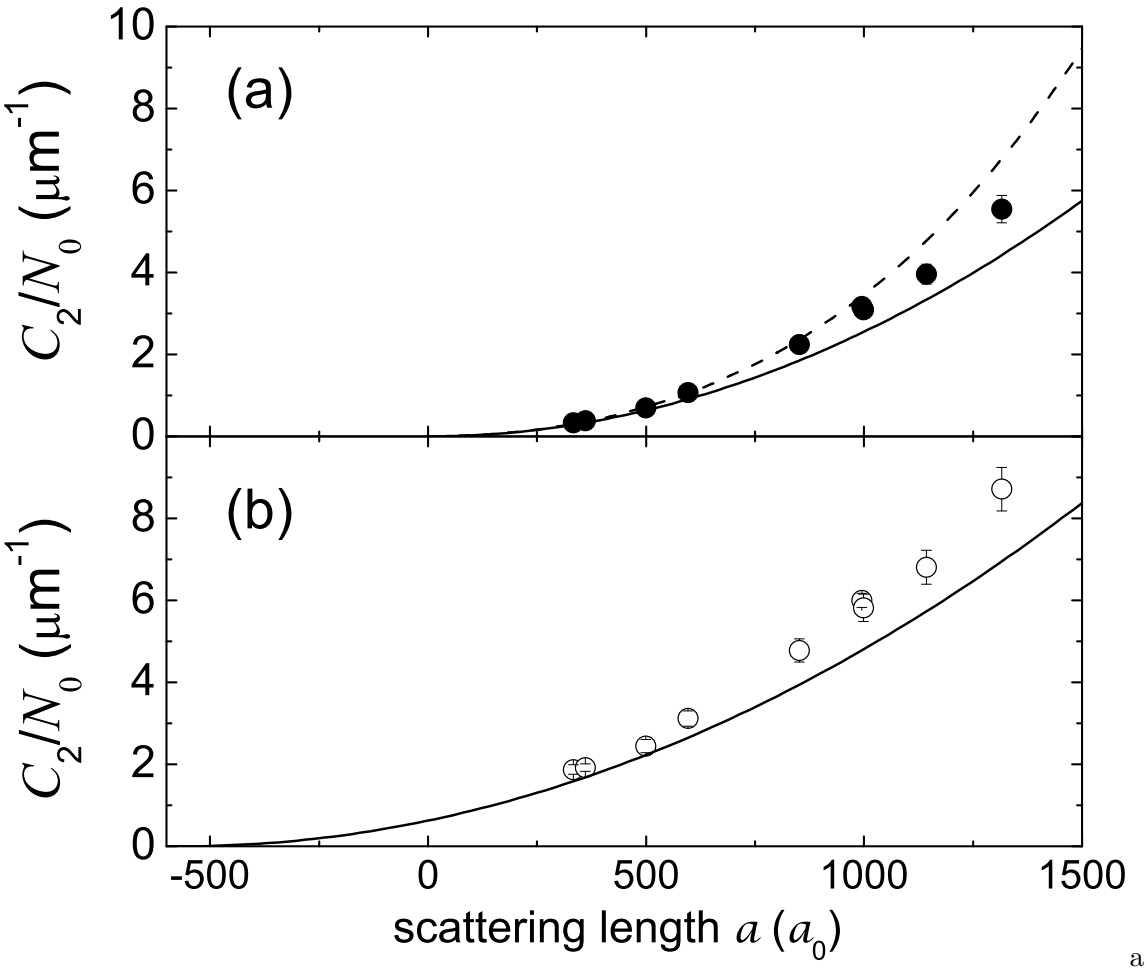

a

Figure 6.2: The contact vs a, measured at $|\omega| = 2\pi \times 40$ kHz. (a) The contact per BEC atom $\frac{C_2}{N_0}$. (b) The raw signal before final-state corrections. The solid lines in (a) and (b) show the mean-field predictions. The dashed line includes the next-order LHY correction. For this data, $\langle n \rangle$ is typically 5.8 x10^{12} cm^{-3}, with $(na^3)^{1/2}$ reaching a maximum of 0.043. We linearly scale the points to account for $\sim$10% variation in density. The final-state effects shift the solid line from a parabola centered about $a = 0$ in (a) to one centered about $a' = -565\ a_0$ in (b), which enhances the raw signal at small a.

a three-body interaction parameter κ_* [57, 92]

$$\frac{dE}{d\kappa_*} = -\frac{2\hbar^2}{m\kappa_*}C_3. \tag{6.4}$$

Three-body short-range correlations contribute a predicted additional term to the RF tail at large detunings that should be added to the right-hand side of Eqn. 6.3 [57]:

$$\frac{\hbar\Omega^2}{2m}\frac{G_{\mathrm{RF}}(\omega)}{\omega^2}C_3. \tag{6.5}$$

Here, $G_{\mathrm{RF}}(\omega)$ is a log-periodic function rooted in Efimov physics:

$$G_{\mathrm{RF}}(\omega) = 9.23 - 13.6\sin[s_0\ln(m|\omega|/\hbar\kappa_*^2) + 2.66]. \tag{6.6}$$

Efimov physics predicts an infinite series of successively more weakly bound trimers whose binding energies at unitarity ($a \to \infty$) are given by $\frac{\hbar^2\kappa_*^2}{m}(e^{-2\pi/s_0})^l$, where l is an integer and s_0 is 1.00624 for identical bosons [96]. We note that there is as yet no prediction for final-state effects on the C_3 contribution to the RF tail.

In order to determine κ_* for ^{85}Rb atoms, we performed measurements of loss rates as a function of a. With these measurements, we locate an Efimov resonance, which is shown in figure 6.3. For these measurements, we make non-condensed clouds of 1.5×10^5 atoms at a temperature $T = 80$ nK. After ramping the magnetic field to realize the desired a on the $a < 0$ side of the Feshbach resonance, we use absorption imaging to measure the number of atoms and cloud size as a function of hold time. We then extract the three-body event rate constant K_3, which is defined by $\frac{d}{dt}N = -3K_3\langle n^2\rangle N$ when all three atoms are lost per event. In extracting K_3, we assume that all of the measured loss is due to three-body processes and we account for the observed heating of the gas, which causes additional decrease in n in time. We fit the measured K_3 vs a to the expected form for an Efimov resonance for non-condensed atoms [96],

$$K_3 = \frac{4590\sinh(2\eta)}{\sin^2[s_0\ln(a/a_-)] + \sinh^2\eta}\frac{\hbar a^4}{m}, \tag{6.7}$$

where η parameterizes the decay rate into deeply bound molecules and the resonance location, a_-, is related to κ_* through $a_- = 1.56(5)\kappa_*^{-1}$ [96]. Because this expression comes from a $T = 0$

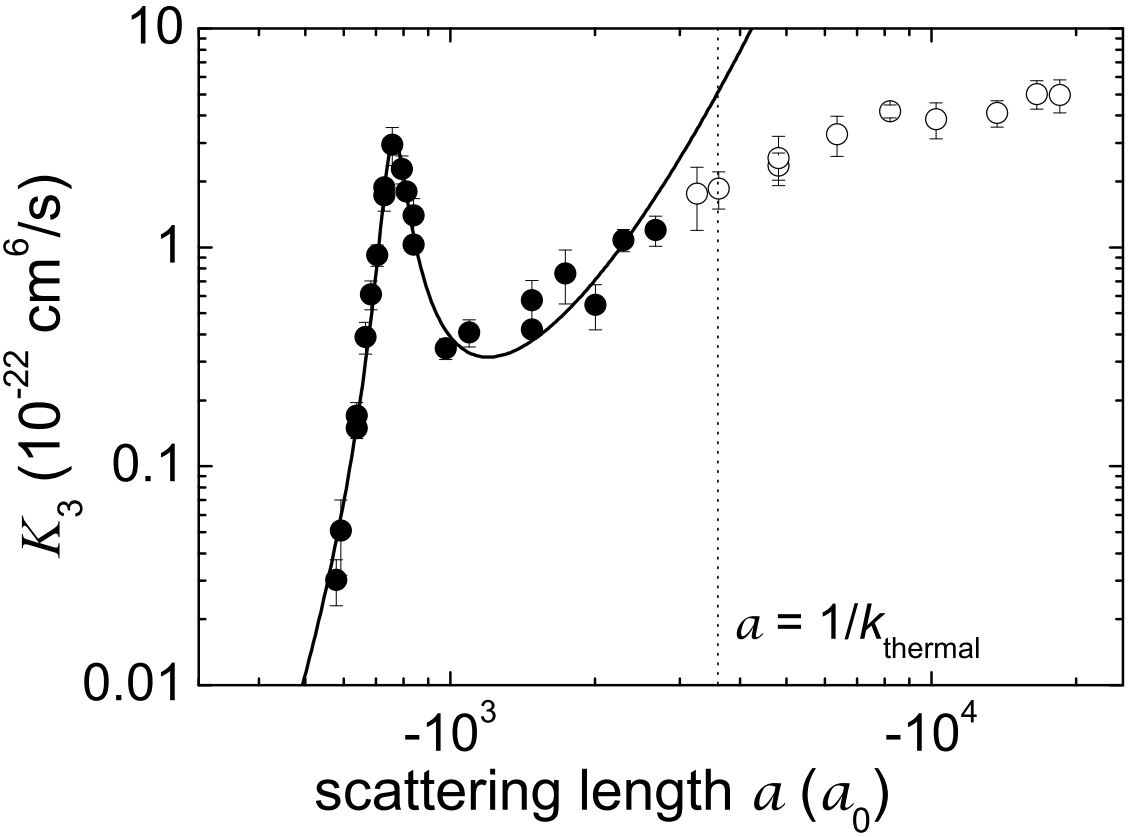

Figure 6.3: A three-body loss resonance for ^{85}Rb. We plot the three-body event constant K_3 vs a. From fitting Eqn. 6.7 to the solid points, for which $a < 1/k_{\text{thermal}}$, we extract $a_- = -759(6)a_0$ and $\eta = 0.057(2)$.

theory, we only fit the data for $a < 1/k_{\mathrm{thermal}}$, where $k_{\mathrm{thermal}} = \sqrt{2mk_BT}/\hbar$ and k_B is Boltzmann's constant. From the fit we find κ_*=39(1) μm^{-1}.

To see how the three-body parameter might impact the many-body physics, we plot the expected frequency dependence of $G_{\mathrm{RF}}(\omega)$ in figure 6.4a. Note that $G_{\mathrm{RF}}(\omega)$ has a node at $|\omega| \sim 2\pi \times 27$ kHz and a smaller magnitude at larger $|\omega|$. Eqn. 6.5 has a frequency dependence given by $G_{\mathrm{RF}}(\omega)/\omega^2$, which suggests that the largest contribution from C_3 will be for smaller $|\omega|$. The prediction for the C_3 term (Eqn. 6.5), like the C_2 term (Eqn. 6.3), is valid for $\omega \to \infty$. For the case of the C_2 term, the RF tail arises from two-body short-range correlations at distances that are small compared to the interparticle spacing, which requires $|\omega| \gg \hbar n^{2/3}/m$. For our typical experimental parameters, $\hbar n^{2/3}/m \sim 2\pi \times 1$ kHz and this requirement is always satisfied. However, for the case of C_3, the prediction for the C_3 tail contribution to the RF tail may only be applicable for $|\omega| > \frac{\hbar}{ma^2}$ [97], where the frequency dependence makes it more difficult to observe this contribution to the RF tail.

The results of our search for C_3 can be seen in figure 6.4b, where we examine the frequency dependence of the RF tail for a BEC at $a = 982 \pm 10\ a_0$. Residual magnetic-field gradients broaden the central feature in the RF spectrum, and this limits our data for the tail to $|\omega| \geq 2\pi \times 10$ kHz. We fit the data to the predicted frequency dependence of the C_2 contribution, shown by the solid line. We can see that our data fit very well to the expected frequency-dependence for the two-body contact with final-state effects, and we do not observe any deviation consistent with a three-body term. Fitting the data to both contributions gives an upper limit for C_3/N_0 of 0.07 μm^{-2}.

In the regime of perturbative interactions, such as assumed in the LHY calculation, one would expect that the short-range correlations in the BEC are dominated by two-body effects. This is consistent with our measurements, where no clear signature of three-body effects is seen in the frequency dependence of the interaction-induced tail in RF spectroscopy. In general, this paves the way for using RF spectroscopy to measure the two-body contact for BECs and thus measure beyond-mean-field physics.

A further result of our studies is the location of the ^{85}Rb Efimov resonance. When a_- is

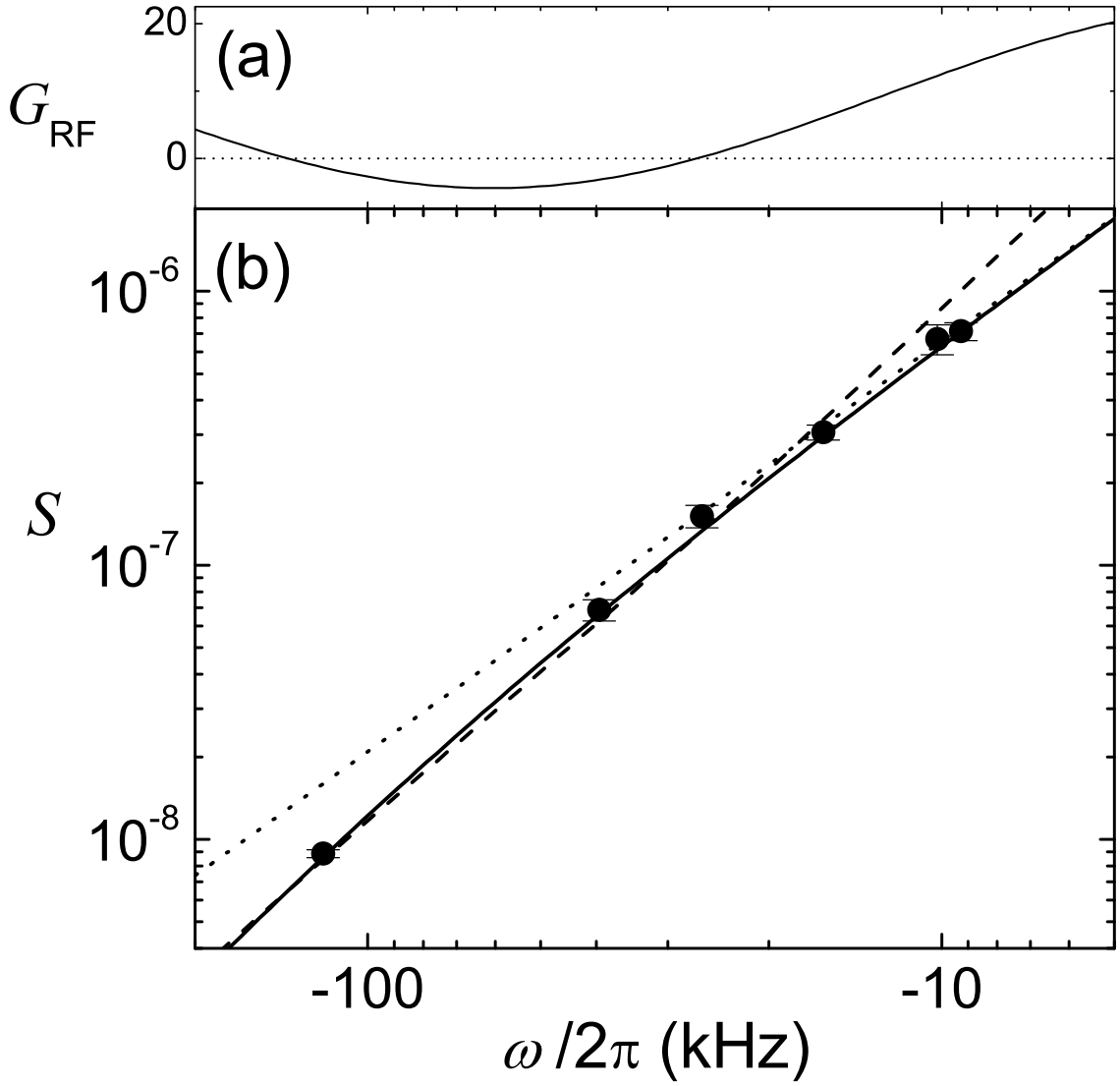

Figure 6.4: (a) The frequency dependence of $G_{\rm RF}(\omega)$, given our measured value for κ_*. (b) Frequency dependence of the tail of the RF spectrum for $a = 982 \pm 10\ a_0$. The solid line is a fit of the data (•) to the expected frequency dependence of the two-body contact C_2/N_0 including final-state effects. The dotted line corresponds to the same value of C_2/N_0, but ignores final-state effects. For comparison, the fit plus a trial C_3/N_0 term of 0.1 μm^{-2} is shown with the dashed line. Our measurements are consistent instead with a C_3/N_0 of zero. Here $\langle n \rangle = 1.0$ x10^{13} cm^{-3}.

expressed in units of the mean scattering length of the van der Waals potential [98] for ^{85}Rb (78.5 a_0), we find a value of -9.67(7) [99], which is very similar to reported results for ^{133}Cs (for multiple Feshbach resonances) [100] and for ^{7}Li [91]. This adds to the empirical evidence suggesting that the three-body parameter depends only on the coefficient of the $1/r^6$ part of the two-body potential and not on the details of a three-body potential at short range [100]. In the many-body physics of an interacting BEC, three-body correlations may yet play a significant role. For example, it will be interesting to look for three-body effects on BECs with strong interactions (at unitarity in the next section), or at $a = a_{-}$. We discuss in the next section measurements of the contact for a BEC at unitarity using the RF techniques developed here.

6.2 If at first you don't measure C_3 ...

In the previous section we presented measurements at finite na^3 of the value of the two-body contact, but only set an upper limit for the three-body contact. The idea then was to increase the interactions even further to look for a three-body contact. Rather than do so in incremental steps, we tuned the magnetic field to unitarity, where $a \to \infty$ [2] . This section describes our preliminary results in measuring the three-body contact for a BEC at unitarity. The contact can be thought of as a measure of the chance that either two or three particles are very close to each other. The two-body contact, C_2, is proportional to the probability that two atoms are near each other and C_3 is proportional to the probability of three atoms being close. Intuitively, the BEC must have a non-zero three-body contact. Since atoms in the BEC undergo inelastic losses, we know C_3 is non-zero, since three atoms must be close to each other during an inelastic loss process. Thus, one way to probe the contact is by measuring inelastic collisions [57]. Moreover, since three-body losses generally increase with increasing scattering length [23, 22], it stands to reason C_3 also increases with scattering length. One then might expect the largest C_3 at unitarity, which is presumably the location of maximum loss.

One caveat to the data presented here is that these measurements were taken before we

[2] These measurements inspired our later work characterizing the degenerate unitarity Bose gas.

characterized the unitarity Bose gas (chapter 7) and before we developed faster ramps to unitarity (chapter 3). The magnetic-field ramps to unitarity for this work were much slower (taking approximately 100 μs) than the ramps we used to investigate the unitarity Bose gas (which took 5 μs). For a BEC at unitarity, we observed dynamics of the unitarity Bose gas on a time scale of 10s of μs, which is shorter than the magnetic-field ramps used for the measurements in this chapter. Therefore, the results of this section may be dependent on the specifics of the magnetic-field ramps. Nevertheless, our preliminary measurement of the three-body contact is interesting and any perturbation to this result due to the specifics of the ramps to unitarity would be an interesting measurement of non-equilibrium many-body dynamics of a BEC.

Like for C_2, we first consider the adiabatic sweep theorem (shown previously as equation 6.4) to predict C_3, which is

$$\left.\frac{dE}{d\kappa_*}\right|_{s,a} = -\frac{2\hbar^2}{m\kappa_*}C_3, \tag{6.8}$$

where E is the total energy of the gas and κ_* is an Efimov three-body parameter [57]. Equation 6.8 relates C_3 to how much the total energy of the BEC changes when one adiabatically changes κ_*. However, unlike the scattering length, κ_* is not a tunable parameter in our system. Instead, the parameter κ_* is related to the binding energy of the Efimov trimer at $a = \infty$ through $E_t = \frac{\hbar^2\kappa_*^2}{m}$ [96]. Also, the dependence of the energy density of a BEC on κ_* has not been predicted and thus we are unable to use it to predict C_3 by applying the adiabatic sweep theorem. Thus, even if we could tune κ_* it is unclear how the energy of a BEC would change. Nonetheless, even without a prediction, we can measure C_3 using two different methods: RF spectroscopy (which we call contact spectroscopy) and by measurements of three-body rates.

Before discussing our measurements, we can apply the adiabatic sweep theorem to is a gas of dilute Efimov trimers at $a = \infty$ to provide context for values of the contact. We can use the adiabatic sweep theorem (equation 6.8 and equation 6.1) to calculate both the two-body and three-body contact, since the trimer energy is a function of both the scattering length and κ_*. The energy

of an Efimov trimer near unitarity is [96]

$$E_t \approx -\frac{\hbar^2\kappa_*^2}{m}\left(1+\frac{2.11}{\kappa_* a}\right) \tag{6.9}$$

Applying the adiabatic sweep theorem (equation 6.8 and 6.4) we calculate C_2/N and C_3/N to be

$$\frac{C_2}{N} = \kappa_*\left(\frac{2.11\times 8\pi}{3}\right) \tag{6.10}$$

$$\frac{C_3}{N} = \frac{\kappa_*^2}{3} \tag{6.11}$$

We can calculate the expected two- and three-body contact for a for a gas of ^{85}Rb Efimov trimers. For the lowest energy Efimov trimer $\kappa_* = 39\ \mu\text{m}^{-1}$, which then gives $C_2/N = 689\ \mu\text{m}^{-1}$ and $C_3/N = 507\ \mu\text{m}^{-2}$. Presumably, the three-body contact in a gas of Efimov trimers, where all the atoms are bound into triplets, close to each other, gives a sort of upper limit of the three-body contact in a Bose gas. The next higher energy trimer has a $\kappa_*^{(1)} = \kappa_*/22.7 = 1.7\ \mu\text{m}^{-1}$, which then gives $C_2/N = 30\ \mu\text{m}^{-1}$ and $C_3/N = 1\ \mu\text{m}^{-2}$.

6.3 RF contact spectroscopy

The technique for measuring the contact at unitarity using contact spectroscopy is essentially unchanged from that for the lower na^3 measurements: we take an RF lineshape, driving a transition between two atomic Zeeman levels, which in our case are split by approximately 80 MHz. In the absence of a contact, the lineshape should be symmetric. However, including the contact leads to an asymmetric lineshape, with a tail extending to large detunings on one side, as shown in figure 6.5. When we add at C_3 term to equation 6.3 it becomes [57]

$$\lim_{\omega\to\infty}\Gamma(\omega) = \Omega^2\left[\frac{1}{4\pi}\sqrt{\frac{\hbar}{m}}\frac{1}{\omega^{3/2}}\frac{\alpha(a)}{\beta(\omega)}C_2 + \frac{G_{RF}(\omega)\hbar}{2m\omega^2}C_3\right], \tag{6.12}$$

where, as before, ω is the detuning from the Zeeman transition frequency, Ω is Rabi frequency, and Γ is normalized by the sum rule $\int_{-\infty}^{\infty}\Gamma(\omega)d\omega = \pi\Omega^2 N$.

The three-body contact, C_3, then gives rise to a deviation from the $|\omega|^{-3/2}$ two-body contact tail. We use the $G(w)|\omega|^{-2}$ deviation to search for a three-body contact signal. In general, the

signal at smaller detunings of ω is where the C_3 signal will be the largest compared to C_2. Figure 6.5 illustrates this by showing the bare RF transition (as a delta function at $\omega = 0$), the broadened lineshape due to Fourier width of the RF pulse (green), and the difference between a C_2 signal (black) and a signal that includes C_2 and C_3 (dashed blue).

6.3.1 Experimental sequence

As was the case for measuring the contact at finite scatting length, we started with a weakly interacting BEC and ramped the magnetic field to change the scattering length. The magnetic field must be stable during the RF pulse since both the scattering length and the transition frequency are magnetic-field dependent. In addition, we needed to cancel any magnetic-field gradients (primarily the vertical gradient that supports the cloud against gravity) that would otherwise cause broadening of the RF lineshape. Also, any time variations of the magnetic field during the RF pulse broaden the lineshape. Minimizing these technical effects is important for looking for a C_3 contribution at relatively small ω. We plot the magnetic-field ramp used to measure C_3 in figure 6.6, which shows the transient magnetic-field contribution from the trap bias coils (blue line) and the measured magnetic field (green circles), following a sweep that started from an initial value of ~ 164 G. The set point for the bias coil is changed at -2.4 ms and the current through the magnetic-field coils settles in approximately 100 μs (this measurement was performed before we had implemented coils capable of driving 5 μs ramps). The discrepancy between the field contributed from the coils (line) and the measured field (points) is due to eddy currents that decay on a 100 μs timescale. We show the power envelope of the truncated gaussian RF pulse in red.

In addition to the magnetic-field stability, we also have to consider and account for density and number losses during the magnetic-field ramp and during the RF pulse. The time we have to probe the BEC at unitarity is much shorter than when we probed the BEC at weak interactions. Three-body losses and the global expansion of the cloud ("breathe") causes the number and density to decay on a timescale similar to our ramp time. The curve in figure 6.6 shows the fastest magnetic-field change our system allowed at the time; this ramp was chosen to avoid, as much as possible,

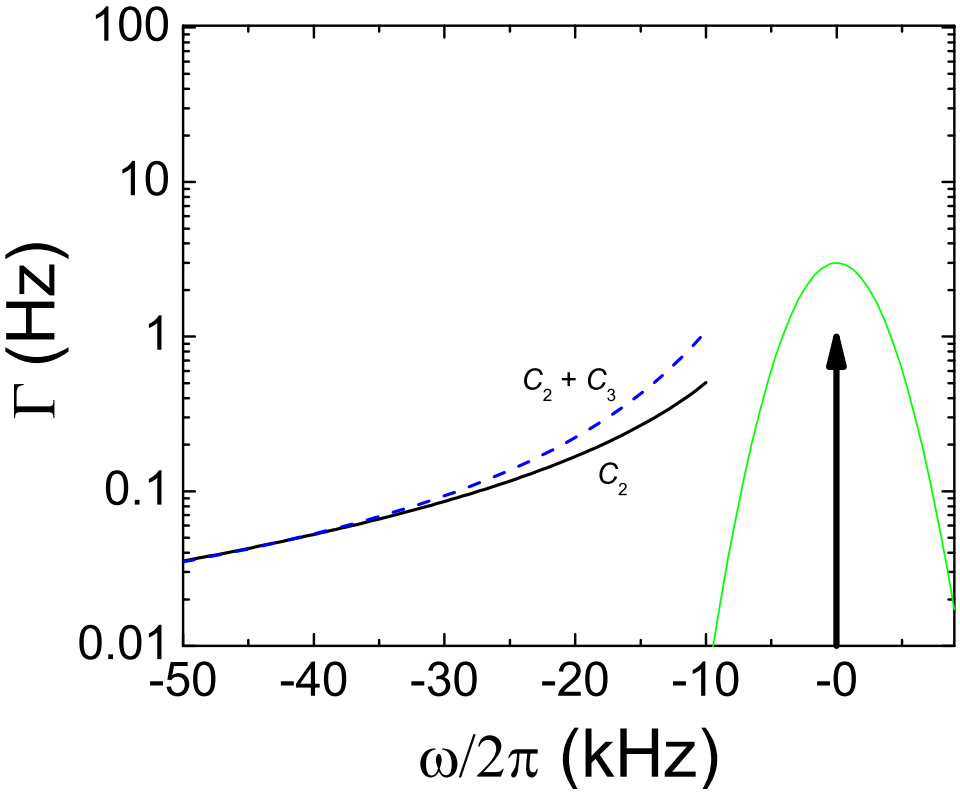

Figure 6.5: A schematic of the excitation rate, Γ, of the atoms as a function of frequency in contact spectroscopy. The black arrow indicates the location of the atomic transition. The green curve is the Fourier broadened lineshape for a 40 μs gaussian pulse. The black and blue curves show the tail at large detunings ω for $C_3 = 0$ and for finite C_3, respectively.

density and number loss.

Then, to measure the contact, we apply a $\pm 4\sigma$ truncated-gaussian RF pulse with an rms width of $\sigma = 40$ μs. We apply the pulse as soon as the field was somewhat stable. The magnetic field has for the most part stopped changing where the power envelope of the gaussian pulse is in figure 6.6. The RF pulse spin flips atoms from the F=2, m_f=-2 state to the F=2, m_f=-1 state. We selectively image the spin-flipped atoms after further transferring them to the F=3, m_f=-3 imaging spin state. For reference, the experimental timings are listed in table 6.1.

Table 6.1: Experimental timings for contact spectroscopy measuring the three-body contact at unitarity

experimental step	start time	end time
ramp to cancel vertical magnetic-field gradient	-6.7 ms	-4.8 ms
jump the magnetic field	-2.4 ms	$\approx$ -2.3 ms
gaussian RF pulse ($\pm 4\sigma$)	-2.31 ms	-1.99 ms
Adiabatic rapid passage to $\|3-2\rangle$ state	-1.95 ms	-1.85 ms
RF pulse to $\|3-3\rangle$ state	-1.8 ms	-1.72 ms
absorption imaging	-1.7 ms	-1.675 ms
trap off	0 ms	0 ms

6.3.2 Results of contact spectroscopy

Figure 6.7 shows the contact spectroscopy measurement at various detunings. We plot a curve with a C_2 contribution and a curve including both a C_2 and a C_3 contribution. Clearly, the data is not consistent with a single $C_2/|\omega|^{3/2}$ curve. The additional signal at smaller detunings could be due to a finite C_3 term. Fitting the data to only a C_2 curve we find $C_2 = 51(10)$ μm^{-1}. If we include a C_3 term we find $C_2 = 53(10)$ μm^{-1} and $C_3/N = 6(1)$ μm^{-2}.

However, there are a number of potential problems with our contact spectroscopy measurement. First, as shown in figure 6.6, the magnetic field is still changing when we start the RF pulse, which is 90 μs after the jump to unitarity. Before doing contact spectroscopy we first find the

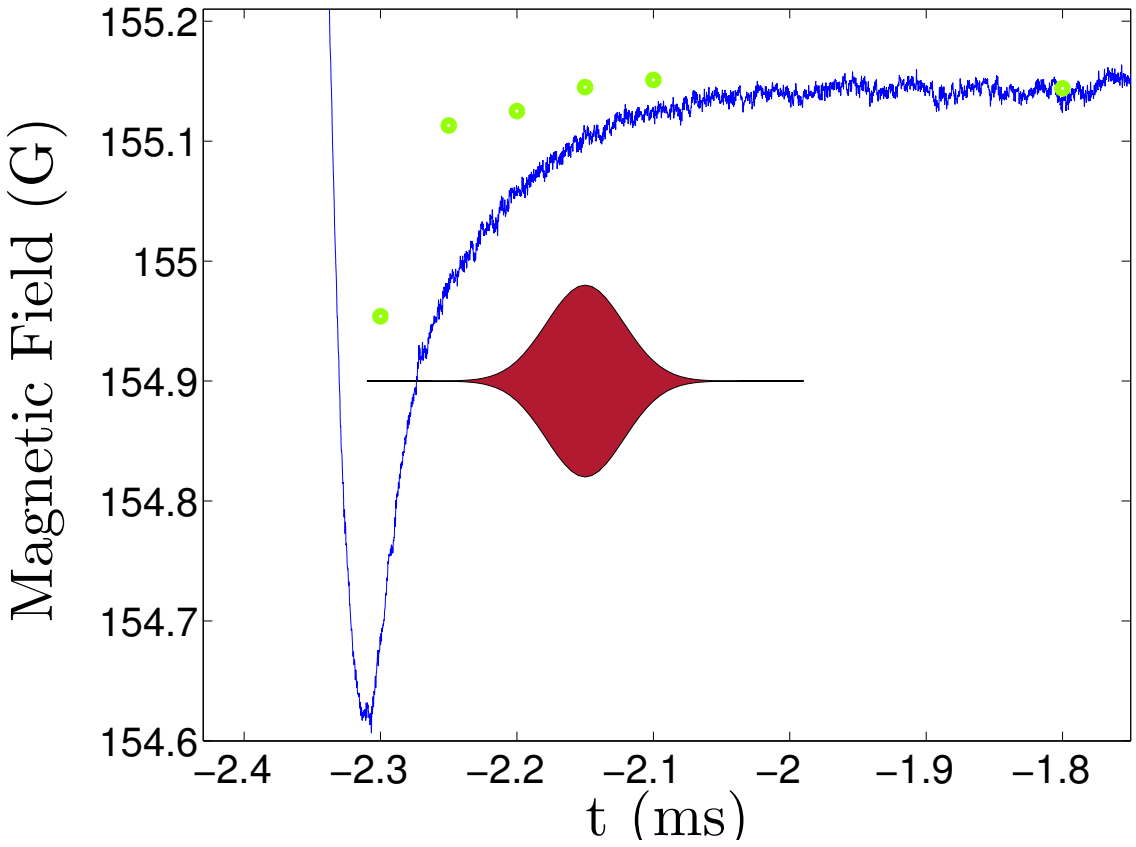

Figure 6.6: The magnetic-field ramp to unitarity. The field set point is changed at -2.4 ms with respect to the trap turning off at 0 ms. The solid blue line is the calculated magnetic field from the measured current in coils. The green points are measurements of the magnetic field using RF spectroscopy of Zeeman levels. The red filled guassian is the power envelope of the RF pulse, which is proportional to the Rabi frequency squared, $\Omega(t)^2$. The $\pm 4\,\sigma$ gaussian envelope of the electric field starts at -2.31 ms and ends at -1.99 ms. This magnetic-field ramp was done before the fast-B coils were added to the experiment.

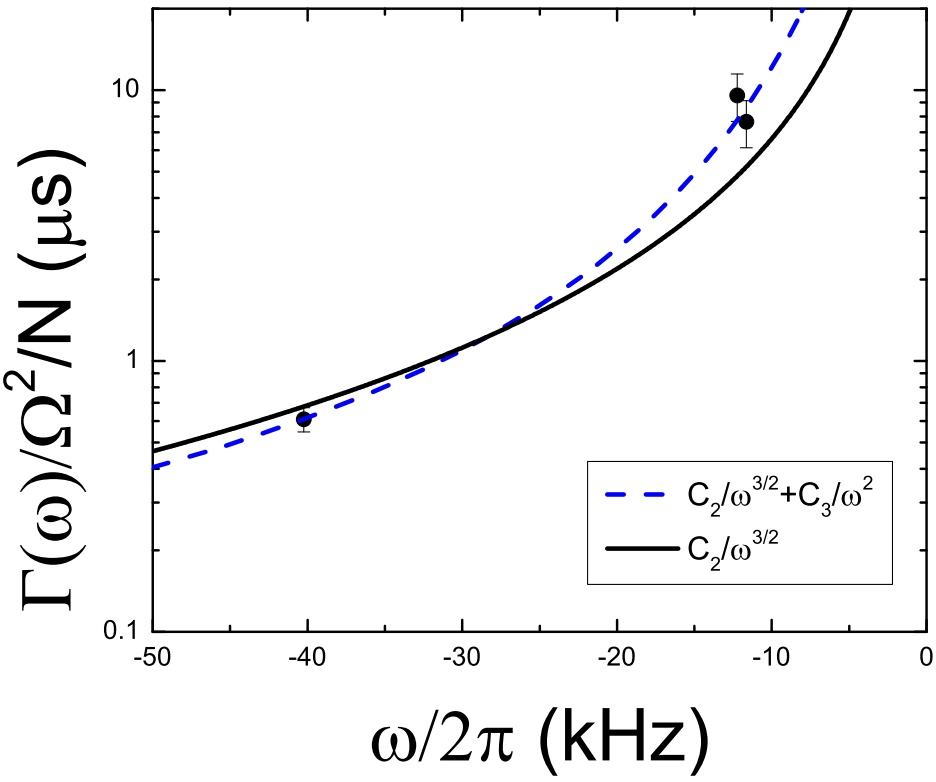

Figure 6.7: The large detuning portion of a RF spectroscopy lineshape for unitarity interactions. The x-axis corresponds to the detuning from the atomic transition. The y-axis is proportional to the signal, which is the coupling rate to the new spin state. The deviation from the C_2 line (black) may be due to a C_3 signal.

transition frequency by taking an RF lineshape. We use a $\pm 4\sigma$ truncated-gaussian RF pulse with $\sigma = 40$ μs to find the center frequency. We don't observe any broadening of this initial RF lineshape. However a shifting magnetic field, that may not necessarily broaden the gaussian lineshape, could cause an asymmetries in the wings of the lineshape, which could appear as a C_3 signal. Second, the detuning from the transition frequency is much smaller for measuring C_3 compared to the C_2 measurement. At these closer detunings the contact signal may be significantly contaminated by the broadened atomic lineshape. We can measure approximately how much the contact signal is contaminated by measuring the excitation rate on the opposite side of the contact tail. For the contact spectroscopy data with detuning $\omega = 40$ kHz the amount of signal due to contamination from the Zeeman lineshape is 10^{-2} times the contact signal. For the data detuned by $\omega \approx 10$ kHz, the additional signal from Zeeman transition is 0.3 times the measured signal. Further careful investigation needs to be done to rule these systematics out of the C_3 signal we measure.

6.4 C_3 from loss measurement

A complementary method to using RF spectroscopy to measure C_3 is using the three-body inelastic loss rate. As we stated before, three-body loss is evidence that C_3 must have a finite value. The relationship between C_3 and $\dot{N}$ is [101]

$$\dot{N} = \frac{-12\eta\hbar}{s_0 m} C_3, \tag{6.13}$$

where η is the same unitless inelastic three-body Efimov parameter from before.

To measure the loss rate, we take *in situ* images of the cloud after a certain hold time at unitarity. Like for contact spectroscopy, we ramped the magnetic field to unitarity in approximately 100 μs when measuring the loss rate. Figure 6.8 shows the number of BEC atoms as a function of time at unitarity. Fitting the loss to a line we extract $C_3/N = 1.0(2)$ μm^{-2}. Described in the next chapter, after implementing our faster ramps, we measured the exponential decay timescale of a BEC (figure 7.2), which for a $\langle n \rangle = 5.5 \times 10^{12}$ cm^{-3} BEC was 630 μs. This corresponds to $C_3/N = 3.1(6)$ μm^{-2}

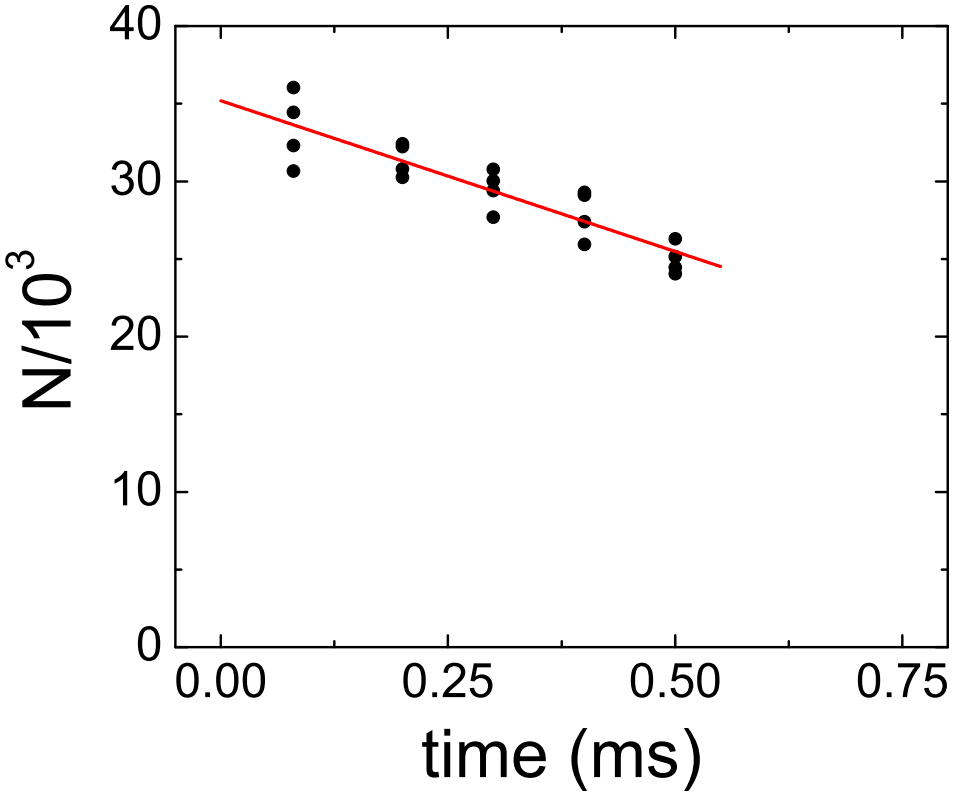

Figure 6.8: An in-situ measurement of loss from a BEC at unitarity. The x-axis is the time after ramping to unitarity and the y-axis is the number of ^{85}Rb atoms in the BEC. The magnetic-field ramp started at approximately -0.1 ms and took 0.1 ms. The black points are measurement of the number and the red line is linear fit to the data, which has a slope of -19(2) μs^{-1}. Using this initial slope, we extract C_3=1.0(2) μm^{-2}. For this data, the average density of the BEC is $\langle n \rangle = 4.7 \times 10^{12}$ cm^{-3}

6.5 Discussion and Outlook

We attempted to measure C_3 using two different methods. The measured three-body contact, $C_3/N = 6(1)$ μm^{-2}, using contact spectroscopy is larger than the contact measured using three-body loss, $C_3/N = 1.0(2)$ μm^{-2} and $C_3/N = 3.2(6)$ μm^{-2}. These values are close to the expected three-body contact for a gas of the Efimov trimers in the second energy branch, $C_3/N = 1$ μm^{-2}. The value of C_2/N derived from RF spectroscopy, 52 μm^{-1}, may be compared to the prediction for the shallow Efimov trimer of 30 μm^{-1} These preliminary results suggests that further measurements

of the three-body contact would be fruitful and perhaps connect the unitarity Bose gas to Efimov physics.[3]

Perhaps most interestingly, since the duration of the magnetic-field ramps was approximately the same timescale as the dynamics of the unitarity Bose (chapter 7) it is unclear how the measured contact is affected by ramp speed. Measuring the contact as a function of magnetic-field ramp speed would shed light on this question. In addition, our ability to now change the magnetic field much faster could allows us to measure the contact at various times. Observing a time-varying C_2 and C_3 would illuminate how two-body and three-body correlations evolve in the BEC at unitarity. Future experimental investigations of C_2 and C_3 seem very promising for the capable hands of future ^{85}Rb experimenters.

[3] It's low hanging fruit!

Chapter 7

What happens to a BEC at unitarity? [1]

This chapter describes our recent results of projecting a BEC onto unitarity and observing the ensuing dynamics of the gas. As chapter 4 discussed, our work with ^{85}Rb has pushed towards larger and larger interaction strengths. However we've been foiled in the pursuit by the metastability of a strongly interacting Bose gas. Overcoming these challenges, this work is the first study of a degenerate Bose gas with $na^3 >> 1$, where n is the atom number density and a is the two-body scattering length. Our experiment was technically possible after implementing the fast-B magnetic field control system that I describe in chapter 3. I will describe the context of the unitarity Bose gas, our experimental sequence, and our results.

7.1 Introduction

7.1.1 Background

Understanding the rich behavior that emerges from systems of interacting quantum particles, such as electrons in materials, nucleons in nuclei or neutron stars, the quark-gluon plasma, and superfluid liquid helium, requires investigation of systems that are clean, accessible, and have tunable parameters. Ultracold quantum gases offer tremendous promise for this application largely due to an unprecedented control over interactions [5]. Specifically, a, the two-body scattering length that characterizes the interaction strength, can be tuned to any value. This offers prospects for experimental access to regimes where the behavior is not well understood because interactions are

[1] Much of this chapter has been submitted for publication[102]

strong, atom-atom correlations are important, mean-field theory is inadequate, and equilibrium may not be reached or perhaps does not even exist. Of particular interest is the unitary gas, where a is infinite, and where many aspects of the system are universal in that they depend only on the particle density and quantum statistics. While the unitary Fermi gas has been the subject of intense experimental and theoretical investigation [103, 104, 105, 106, 107, 108, 109], the degenerate unitary Bose gas [110, 111, 112, 113, 20, 21, 114, 115] has generally been deemed experimentally inaccessible because of three-body loss rates that increase dramatically with increasing a. Here, we investigate dynamics of a unitary Bose gas for timescales that are short compared to the loss. We find that the momentum distribution of the unitary Bose gas evolves on timescales fast compared to losses, and that both the timescale for this evolution and the limiting shape of the momentum distribution are consistent with universal scaling with density. This work demonstrates that a unitary Bose gas can be created and probed dynamically, and thus opens the door for further exploration of this novel strongly interacting quantum liquid.

As I showed in chapter 2, a powerful feature of atom gas experiments that provides access to these new regimes is the ability to change the interaction strength using a magnetic-field Feshbach resonance. In particular, at the resonance location, a is infinite. For atomic Fermi gases, accessing this regime by adiabatically changing a led to the achievement of superfluids of paired fermions and enabled investigation of the crossover from superfluidity of weakly bound pairs, analogous to the Bardeen-Cooper-Schrieffer (BCS) theory of superconductors, to Bose-Einstein condensation (BEC) of tightly bound molecules [105, 106]. For bosonic atoms, however, this route to strong interactions is stymied by the fact that three-body inelastic collisions increase as a^4 [23, 22]. This circumstance has limited experimental investigation of Bose gases with increasing interaction strength to studying either non-quantum degenerate-thermal gases [62, 63] or BECs with modest interaction strengths ($na^3 < 0.008$) [15, 17, 19, 61].

The problem is that the loss rate scales as n^2a^4 while the equilibration rate scales as na^2v, where v is the average velocity. Thus, it would seem that the losses will always dominate as $|a|$ is increased to ∞. Even if we were to forsake equilibrium and suddenly change a in order to

project a weakly interacting BEC onto strong interactions [116, 117, 61, 118], one might expect that three-body losses would still dominate the ensuing dynamics for large a. In this work, however, we use this approach to project a BEC "instantaneously" onto the unitary gas regime. We observe dynamics that in fact saturate on a timescale shorter than that set by three-body losses and that exhibit universal scaling with density.

7.1.2 Universality

One of the intriguing aspects of the unitary gas is that since a diverges, it can no longer be a physically relevant scale for describing the system and its behavior. For a gas near zero temperature, such as a BEC, the only physical scale that remains at unitarity is the interparticle spacing. (In principle, the size of the cloud, or, equivalently the trap parameters, can provide a length scale, although one that is not intrinsic to the system. In addition, we are ignoring here any explicit three-body interactions, which could provide an additional length scale.) The gas behavior should then be universal in the sense that it is characterized only by the density n. This means that energies scale as $n^{2/3}$, momenta as $n^{1/3}$, and times as $n^{-2/3}$, which we parameterize respectively by $E_n \equiv \hbar^2(6\pi^2 n)^{2/3}/2m$, $k_n \equiv (6\pi^2 n)^{1/3}$, and $t_n \equiv \hbar/E_n$.

The universality that makes the unitary gas so remarkable also provides a reason to hope that rapid three-body loss will not necessarily be an insurmountable barrier to experimental exploration of bulk (as opposed to lattice-confined) degenerate Bose gases with unitarity-limited interactions. For the degenerate unitary Bose gas, both the loss rate and the equilibration rate must scale as $n^{2/3}$. The comparison of the two rates then hinges on unknown numerical prefactors, and it becomes an experimental question whether losses dominate or a *local* equilibrium can be reached. In addition, we note that on resonance, the shallow bound state that exists for finite positive a disappears, shown in figure 2.2, so that loss requires atoms to decay to deeply bound molecular states [119]. For ^{85}Rb atoms, the previous experimental observation (figure 6.3) of a relatively narrow, and therefore long-lived, Efimov resonance (characterized by a dimensionless width, $\eta \sim .06 \ll 1$) [19] is indicative that atoms close together do not decay instantaneously to deeply bound molecular

states.

7.2 Experimental sequence

Our experiments begin with a ^{85}Rb BEC with 6×10^4 atoms confined in a 10 Hz spherical magnetic trap. The magnetic field, B, is set 8 G above the ^{85}Rb Feshbach resonance at $B_0 = 155.04$ G [10]. This sets the initial a to 150 a_0, which gives the BEC a Thomas-Fermi density distribution with an average density $\langle n \rangle = 5.5 \times 10^{12}$ cm^{-3}. With a typical initial temperature < 10 nK, the thermal deBroglie wavelength is large compared to $\langle n \rangle^{-1/3}$ and is not a relevant length scale in the physics of the ensuing experiment. Starting with this BEC in the extremely dilute limit, with $\langle n \rangle a^3 < 10^{-5}$, we then decrease B to B_0 in 5 μs. During the final 3 μs of the ramp of B, $\langle n \rangle a^3$ goes from an essentially dilute value of 10^{-4} to $\langle n \rangle a^3 \gg 1$.

After allowing the cloud to evolve at unitarity for a time t, we measure the momentum distribution of atoms by ramping, equally rapidly, back to small a and allowing the gas to expand ballistically before imaging the cloud using resonant, high-intensity absorption imaging [36]. We show the experimental sequence in figure 7.1 From an azimuthal average of the image, we extract a momentum-space column density $\tilde{n}$ as a function of the component of momentum perpendicular to the line of sight, $\tilde{k}$. By imaging at various times of flight (7, 13, 25 ms), we increase the dynamic range of our data and reduce the region of $\tilde{k}$ that is obscured by initial-size effects. We repeat this experimental procedure for various t to explore the evolution of the momentum distribution as a function of time at unitarity.

7.2.1 Methods

Magnetic-field control: To rapidly change the magnetic field, we use an additional pair of coils, each with 10 turns and a diameter of 1.0 cm, 2.8 cm apart. The step response of the system has a 10–90% rise time of 2.1 μs; thus, the 5 μs magnetic-field sweep used in the measurements is below the maximum bandwidth of the system. We characterize and pre-correct for induced currents from mutual inductances between these coils and the magnetic trap coils as well as eddy currents

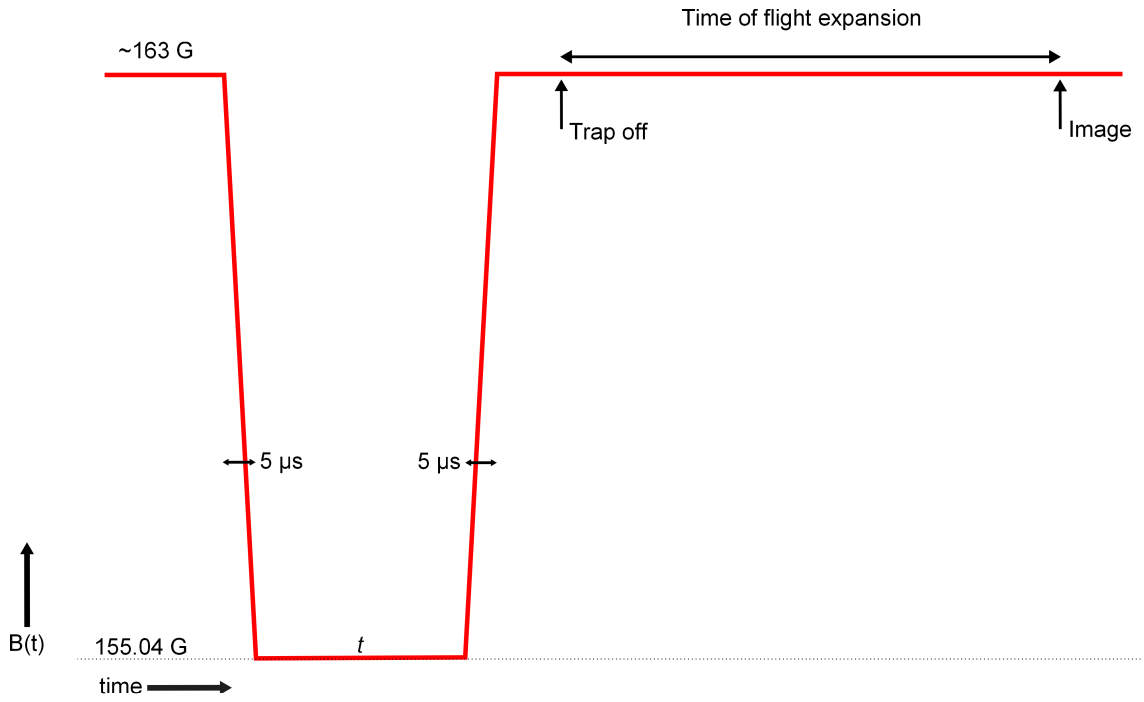

Figure 7.1: The experimental sequence of projecting a gas onto unitarity interactions. The magnetic field is ramped to and from unitarity in 5 μs. We turn the trap off and image the atoms after a time-of-flight expansion.

in surrounding conductors. Taking into account roughly equal contributions from uncertainty in our magnetic field and the uncertainty in the Feshbach resonance location B_0 [10], we estimate that our experiments are within $\pm$ 50 mG of the Feshbach resonance, which corresponds to $|a| > 95,000$ a_0.

Loss rate at unitarity: Using the initial loss rate implied by the exponential fit to the data shown in figure 1, and using $\mathrm{d}N/\mathrm{d}t = -L_3 \int n(\mathbf{r})^3 \mathrm{d}^3\mathbf{r}$, we extract $L_3 = 5(1) \times 10^{-23}$ cm^6/s. Unitarity-limited three-body loss rates for a non-degenerate Bose gas have been recently investigated by Rem *et al.* [62]. Using Eqn. 5 from Rem *et al.* [62] and the Efimov resonance width, η, from Wild *et al.* [19] , the predicted L_3 for ^{85}Rb atoms at a temperature of 10 nK is 3×10^{-20} cm^6/s, which is two and a half orders of magnitude larger than what we measure. On the other hand, after the jump to unitarity, universality suggests that we should use an effective temperature determined by the interparticle spacing. Using $E_n/k_B = 135$ nK, where k_B is Boltzmann's constant, gives an

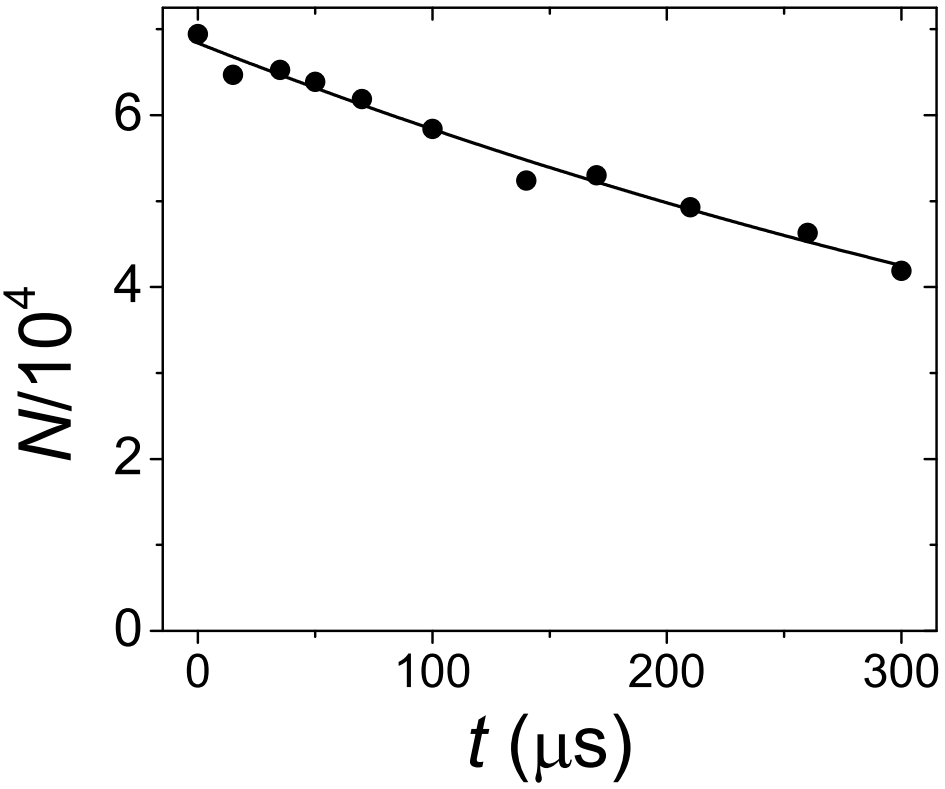

Figure 7.2: Number of atoms measured using absorption imaging as a function of the time at unitarity. The number measured without ramping to unitarity is shown at $t = 0$. The solid line shows an exponential fit to the data (points), which gives a time constant of 630 ± 30 μs.

estimate for L_3 of 1.7×10^{-22} cm^6/s, which is within a factor of 4 of our measurement. For the low $\langle n \rangle$ data, L_3 is a factor of 6.2(5) larger than for the high $\langle n \rangle$ data. Using the unitarity limit for T_n, we would expect this ratio to be 5.2(6).

Momentum distributions: For the time-of-flight expansion, the 10 Hz spherical magnetic trap is turned off over 2 ms, while keeping the magnitude of the total magnetic field constant. Because the trap turns off in a time that is much shorter than the trap period, it has a negligible effect on the momenta of the atoms. We image the atoms using a 5 μs imaging pulse. The direction of the imaging beam and the magnetic-field direction are shown in figure 5. For each hold time at unitarity, we repeat the experiment four times for each of three different times of flight, $t_{\rm exp}$: 25 ms, 13 ms, and 7 ms. Each image is azimuthally averaged, and the curves for the same TOF

are averaged together. We then combine the averaged curves into a single momentum distribution, $\tilde{n}(\tilde{k})$, using the largest $t_{\rm exp}$ data at the smallest $\tilde{k}$ and the smallest $t_{\rm exp}$ data at the largest $\tilde{k}$. This minimizes the initial-size effects at small $\tilde{k}$, while improving the signal-to-noise ratio at larger $\tilde{k}$. In combining the curves, we enforce agreement in the overlap regions by applying a multiplicative factor to the data for shorter $t_{\rm exp}$. This additional scaling factor, which ranges from 1.07 to 1.26 for the $t_{\rm exp}$=13 ms data and from 1.5 to 2.1 for the $t_{\rm exp}$=7 ms data, reflects systematic uncertainties that become increasingly important as $\tilde{n}(\tilde{k})$ decreases by orders of magnitudes.

At small $\tilde{k}$, the measured $\tilde{n}(\tilde{k})$ is distorted by the initial size of the BEC (the Thomas-Fermi radius is 16 μm for the higher $\langle n\rangle$ data and 22 μm for the lower $\langle n\rangle$ data) and by our imaging resolution (characterized by a gaussian width of approximately 6 μm). The gray regions in figure 2, and the corresponding regions where the data are shown as dashed lines in figure 3, are bounded by a radius of 58 μm in the expanded cloud image. In the absence of the jump to unitarity, the BEC with $\langle n\rangle = 5.5(3)\times 10^{12}$ cm^{-3} has 97% of the atoms within this radius after an expansion time of 25 ms. We note that all the effects discussed here cause low-momentum atoms to appear at larger radii than one would expect from the product of velocity and $t_{\rm exp}$. Therefore, integrating the signal up to a particular momentum gives a lower limit to the number of atoms that have momenta below that value. We use this fact in extracting a lower bound for the density in phase space.

7.3 Conclusions and arising questions from the results

From images of the expanded cloud, we also obtain the number of atoms, N, which we show in figure 7.2 as a function of t. Fitting an exponential decay to this early time data yields a time constant of 630 ± 30 μs. A fact that is immediately clear from this data is that the number loss at unitarity occurs on a timescale that is much longer than the few μs duration of our ramps onto and away from the Feshbach resonance.

For understanding the dynamics at unitarity, it is also important to know the timescale for changes in the spatial extent of the condensate. Specifically, exploring the possibility of local equilibration only makes sense while the density of the gas remains largely unchanged. The spherical

aspect ratio of the trap was chosen to optimize the duration of inertial confinement. *A priori*, it is not obvious whether the BEC will expand or collapse after the jump to unitarity. With in-situ images of the gas at unitarity, we find the cloud size remains unchanged to within our measurement precision for ∼500 μs and then slowly increases. The measured change in the spatial volume of the condensate is $(6 \pm 9)\%$ during the first 500 μs at unitarity.

Equipped with this information regarding the timescales for number loss and for expansion of the trapped gas at unitarity, we now consider the measured momentum distributions. These are shown in figure 7.3 for various t, with the inset showing the same data on a log-linear plot. Given the finite times of flight before imaging, the data at small $\tilde{k}$ are strongly affected by the initial size of the BEC and do not accurately reflect $\tilde{n}(\tilde{k})$; the gray regions in figure 7.3 indicate where initial-size effects are non-negligible, and we see that a significant fraction of the signal lies within this region. Nevertheless, the data clearly show the emergence of signal at high $\tilde{k}$, outside the gray regions. The signal at high $\tilde{k}$ grows as a function of t before saturating in approximately 100 μs. In this time, the gas has not yet lost a significant number of atoms or significantly reduced its density. The fact that the timescale for the shape of $\tilde{n}(\tilde{k})$ to stop evolving is very different than the loss timescale clearly points to a mechanism for this dynamics that is distinct from three-body loss. Furthermore, the much shorter timescale for saturation of $\tilde{n}(\tilde{k})$ suggests the existence of a "quasi-equilibrium" metastable state of a degenerate Bose gas at unitarity.

To look for evidence of universality, we repeated the measurements for a lower initial density of the BEC. Here, we begin the experimental cycle by increasing a to 400 a_0 for 20 ms, increasing the cloud radius and reducing $\langle n \rangle$ to 1.6×10^{12} cm^{-3}. We measure a loss timescale for the lower density data shown in figure 7.6. Following the jump to unitarity, the measured $\tilde{n}(\tilde{k})$ for lower initial $\langle n \rangle$ also shows the emergence of signal at high $\tilde{k}$ at unitarity, see figure 7.5. The distributions are similar to those measured for the higher $\langle n \rangle$ (figure 7.3), except that the dynamics occur over a longer time scale, with $\tilde{n}(\tilde{k})$ saturating in approximately 200 μs. We extract the three-dimensional $n(k)$ using an inverse Abel transform. To compare the two saturated curves, in figure 7.4, we show the saturated momentum distributions as a function of the scaled momentum, $\kappa = k/k_n$, where k_n

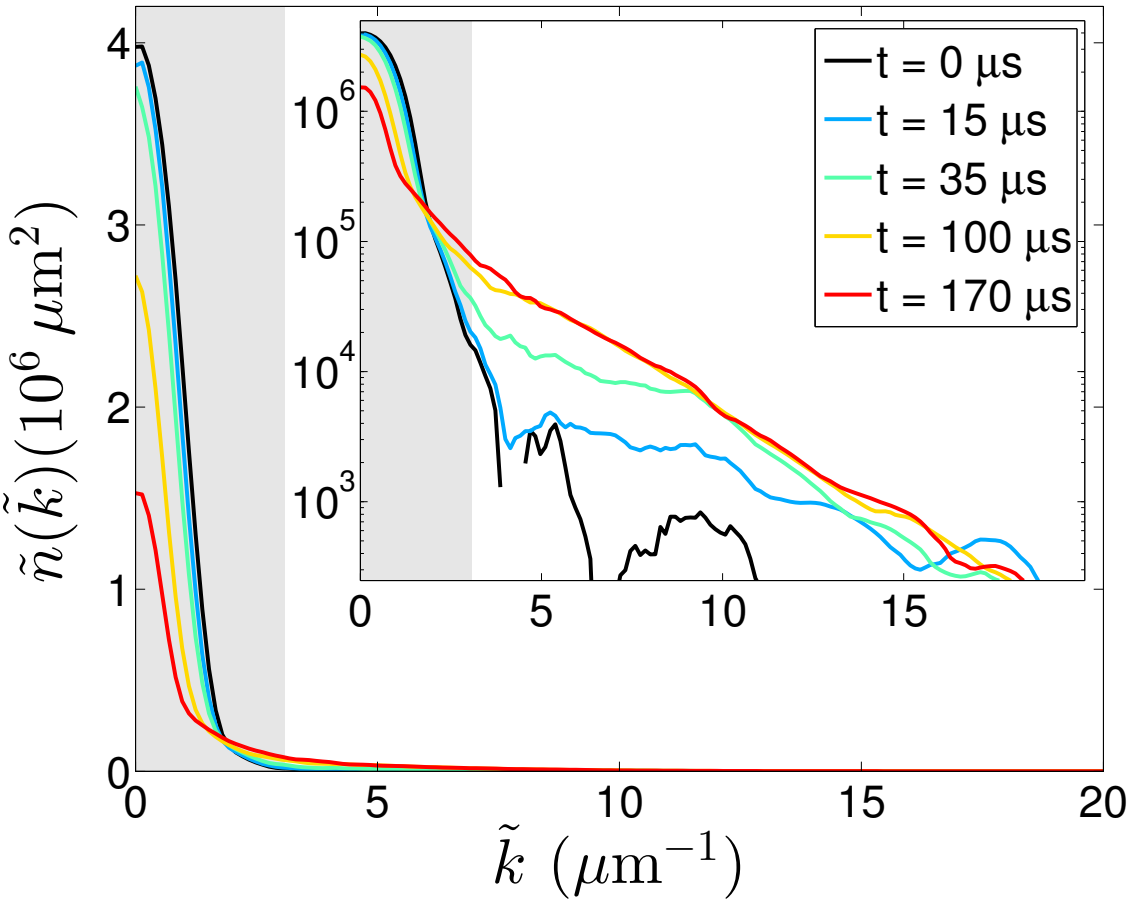

Figure 7.3: The column-integrated momentum distribution $\tilde{n}(\tilde{k})$ versus the transverse momentum $\tilde{k}$ after evolving at unitarity for time t. The distribution measured without ramping to unitarity is shown at $t = 0$. For each t, the integral $\int \tilde{n}(\tilde{k}) 2\pi\tilde{k}\mathrm{d}\tilde{k} = 8\pi^3 N(t)$. For this data $\langle n \rangle = 5.5(3) \times 10^{12}$ cm^{-3}, which corresponds to $k_n = 6.9\ \mu\mathrm{m}^{-1}$. Each momentum distribution is obtained from several images for each of three expansion times (7, 13, and 25 ms). The inset shows the same data plotted on log-linear axes. The gray regions indicate the part of data that is contaminated by initial-size effects and, therefore, does not accurately reflect the momentum distribution. We observe the emergence of signal outside this region, and a saturation of $\tilde{n}(\tilde{k})$ for $t >$100 μs.

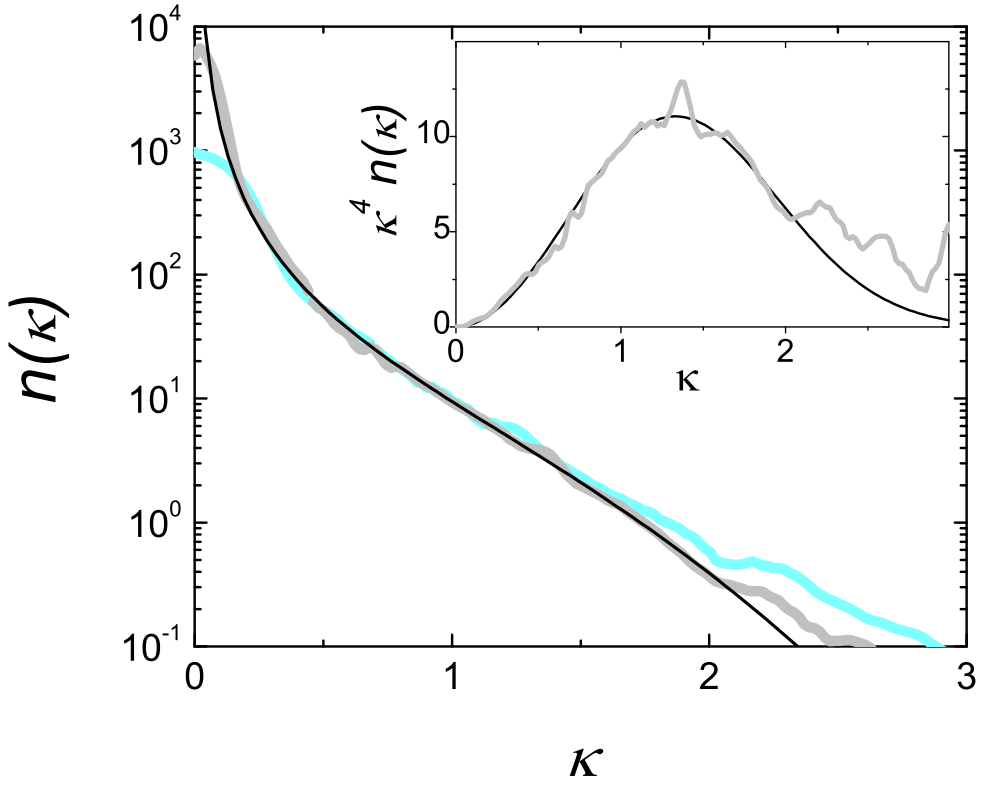

Figure 7.4: The momentum distribution, $n(\kappa)$, plotted versus the scaled momentum, κ. Data for $\langle n \rangle = 5.5 \times 10^{12}$ cm^{-3} and $\langle n \rangle = 1.6 \times 10^{12}$ cm^{-3} are shown as the gray and cyan lines, respectively. The higher $\langle n \rangle$ data is the average of measurements for 6 hold times t between 100 μs and 300 μs, while the lower $\langle n \rangle$ data is the average of 4 measurements for t between 200 μs and 700 μs. The distributions are normalized so that $\int n(\kappa) 4\pi\kappa^2 \mathrm{d}\kappa = 8\pi^3$. The data for two different densities are consistent with a single curve when plotted in scaled units. Inset: Plotting $\kappa^4 n(\kappa)$ for high $\langle n \rangle$, we do not find clear evidence for a $1/\kappa^4$ tail at high κ.

is calculated at the average density $\langle n \rangle$. We find that the shape of the distributions for the two $\langle n \rangle$ are very similar.

Given that our data are consistent with a universal shape for the saturated $n(\kappa)$ at high κ, we now discuss aspects of this distribution. First, we note that although much of the signal remains at small κ where our data are affected by initial-size effects, the population with $\kappa > 0.5$ for the saturated $n(\kappa)$ is nearly 50% of the initial N. Particularly, it is suggestive that saturated density distribution appears to have a low momentum peak, much like a BEC. Second, for short-range interactions, such as those that give rise to the s-wave scattering length for atoms, one expects a $1/\kappa^4$ tail at high momentum for an equilibrium gas, where the amplitude of this tail is the thermodynamic parameter known as the contact [55]. We do not find evidence for a $1/\kappa^4$ tail at high momentum, which would appear as a flat line for large κ in figure 7.3(inset); however, a $1/\kappa^4$ tail may exist below our detection limit at large κ where the signal-to-noise ratio is poor.

Finally, we consider the low-κ part of the momentum distribution and the question of whether or not the gas remains degenerate after the rapid sweep to unitarity. At low κ, initial-size effects can play a non-negligible role. However, this effect is such that we can obtain a *lower limit* on the fraction of atoms that have $\kappa < \kappa_{\max}$ by integrating our $n(\kappa)$ data up to $\kappa_{\max}$. This allows us to extract a lower limit for the density of atoms in phase space. Specifically, we calculate the average occupancy per state at low κ, which is given by the number of atoms divided by the number of states in phase space:

$$\langle \rho_{occ} \rangle = \left(\frac{N}{8\pi^3} \int_0^{\kappa_{\max}} n(\kappa) 4\pi\kappa^2 \mathrm{d}\kappa \right) / \left(\frac{V}{h^3} \frac{4\pi}{3} (\hbar k_n)^3 \kappa_{\max}^3 \right), \tag{7.1}$$

where we conservatively use for the effective coordinate-space volume, $V = \frac{4\pi}{3} R_{\mathrm{TF}}^3$, where R_{TF} is the Thomas-Fermi radius of the initial weakly interacting BEC. For the higher $\langle n \rangle$ data, where the effects of the initial size are smaller, choosing for example $\kappa_{\max} = 0.26$ gives 23% of the atoms and $\langle \rho_{occ} \rangle = 7.1$ for $t = 170\ \mu\mathrm{s} = 3\ t_n$. The fact that this lower limit for the density in phase space is much larger than 1 for a significant fraction of the atoms indicates that the gas is degenerate.

In addition to considering the saturated $n(\kappa)$, we present the observed timescale for the

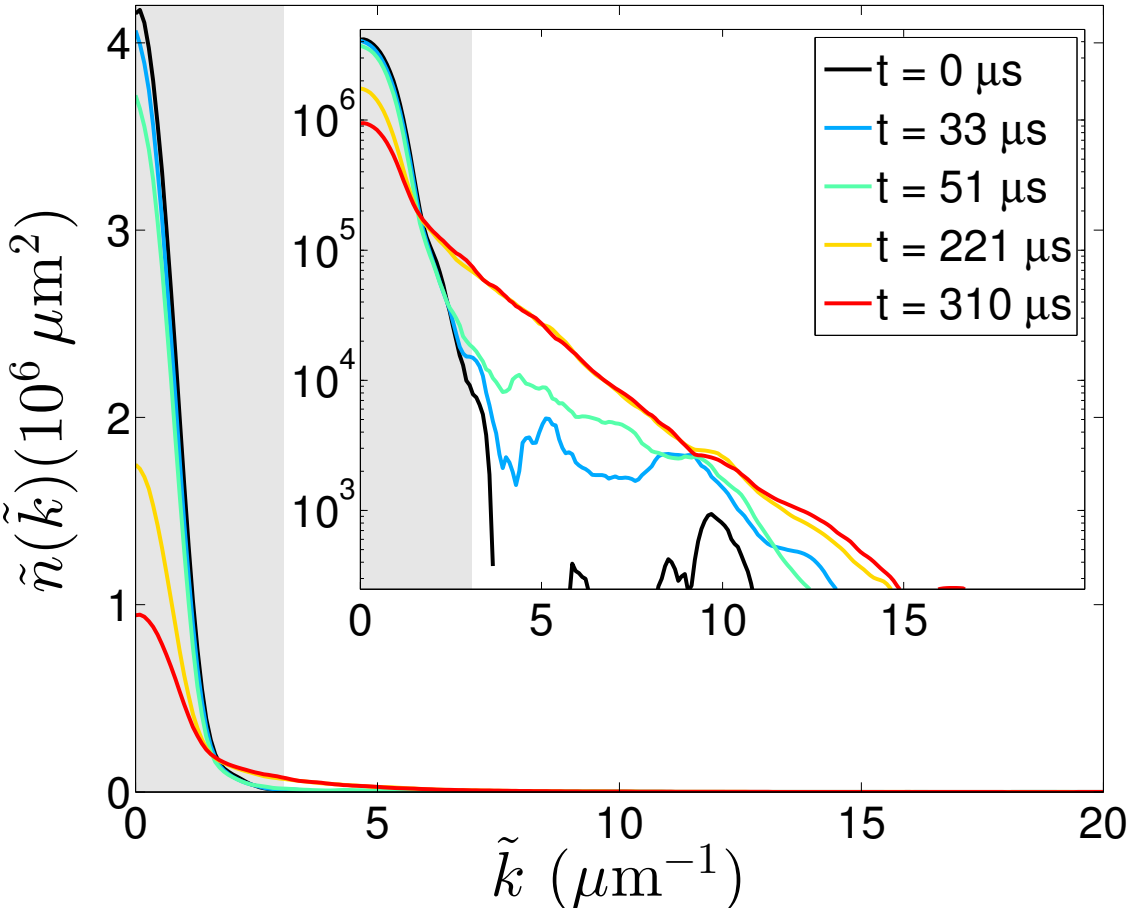

Figure 7.5: The column-integrated momentum distribution $\tilde{n}(\tilde{k})$ versus the transverse momentum $\tilde{k}$ after evolving at unitarity for time t. The distribution measured without ramping to unitarity is shown at $t = 0$. For each t, the integral $\int \tilde{n}(\tilde{k}) 2\pi\tilde{k}\mathrm{d}\tilde{k} = 8\pi^3 N(t)$. For this data $\langle n \rangle = 1.6(1) \times 10^{12}$ cm^{-3}, which corresponds to $k_n = 4.5\ \mu\mathrm{m}^{-1}$. Each momentum distribution is obtained from several images for each of three expansion times (7, 13, and 25 ms). The inset shows the same data plotted on log-linear axes. The gray regions indicate the part of data that is contaminated by initial-size effects and, therefore, does not accurately reflect the momentum distribution. We observe the emergence of signal outside this region, and a saturation of $\tilde{n}(\tilde{k})$ for $t >$200 μs.

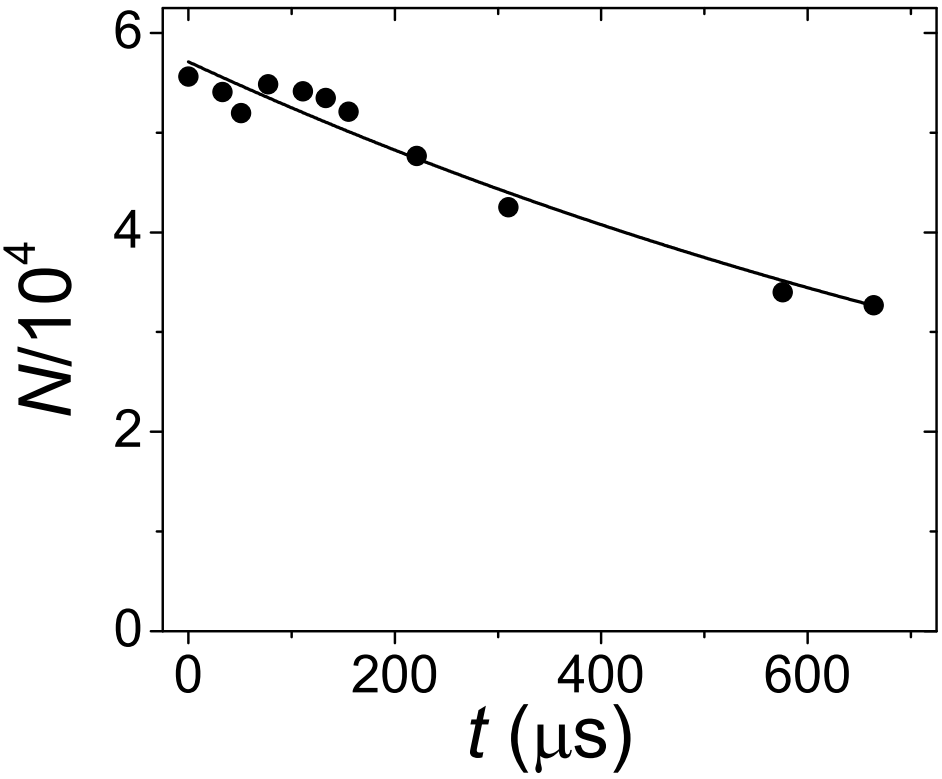

Figure 7.6: Number of atoms measured using absorption imaging as a function of the time at unitarity for our low density data. For this data $\langle n \rangle = 1.6(1) \times 10^{12}$ cm^{-3}. The number measured without ramping to unitarity is shown at $t = 0$. The solid line shows an exponential fit to the data (points), which gives a time constant of 1200 $\pm$ 100 μs.

dynamics in figures 7.7, 7.8 and 7.9, we examine the timescales for the dynamics that give rise to the saturated $n(\kappa)$. As can be seen in figure 7.3, the evolution of the momentum distribution is not uniform, with the higher momentum population saturating earlier. In figure 7.7, we plot the number of atoms, ΔN, within a specific momentum range as a function of t, for two different ranges of momentum κ. We also plot the timescales for the same κ and different $\langle n \rangle$ in figure 7.8. In each case, we find that the number of atoms within the specific momentum range grows and then saturates. We find that the timescale for this saturation increases for smaller κ, and for smaller $\langle n \rangle$. We fit the data for each different κ range to an exponential and extract a time constant τ.

To look for universality in the timescales, we normalize τ by the characteristic time set

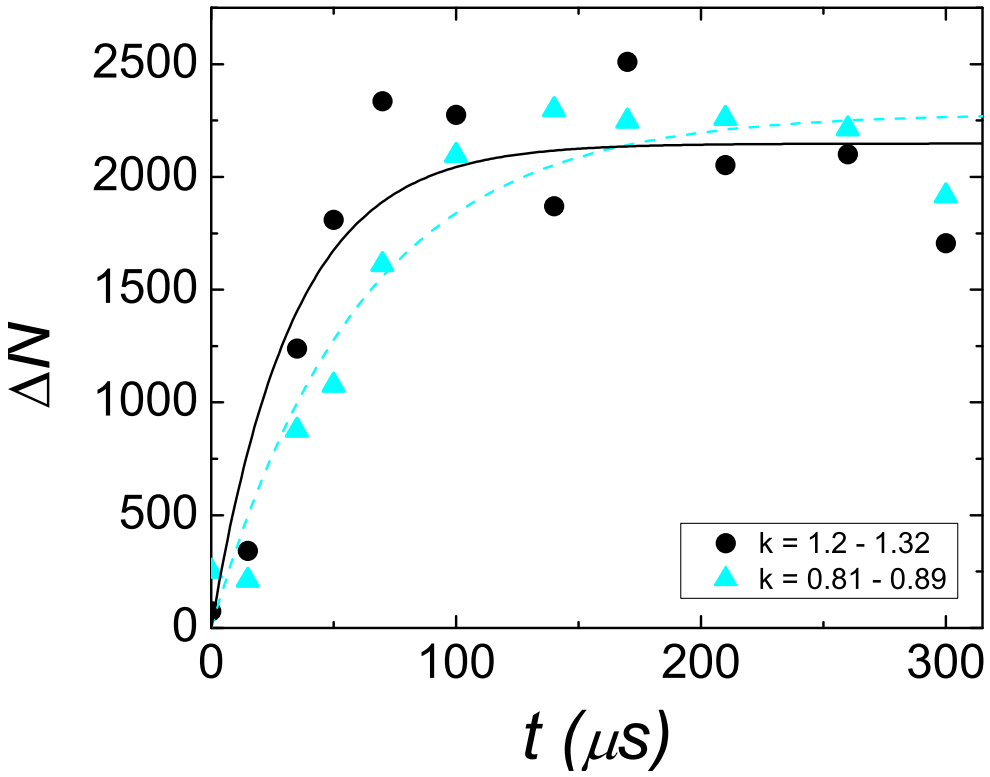

Figure 7.7: The number of atoms in two momentum ranges vs. t. Data is for $\langle n \rangle = 5.5 \times 10^{12}$ cm^{-3}. The black circles are the fraction of atoms with κ between 1.20 and 1.32. The cyan trianges are the fraction of atoms with κ between 0.81 and 0.89. The lines show fits of the data to $\Delta N_0(1-\exp^{-t/\tau})$, from which we extract the timescale for saturation, τ.

by the interparticle spacing, t_n, where t_n is 57 μs and 130 μs for the data at higher and lower $\langle n \rangle$, respectively. Plotting the normalized τ/t_n vs. κ, we find that the momentum-dependent dynamics at our two different densities are consistent (figure 7.9). We conclude that the timescale for $n(\kappa)$ dynamics is universal in that it depends only on the density, or interparticle spacing. The momentum dependence of the timescales remains to be understood, although it is perhaps not unexpected that higher momenta saturate faster.

In conclusion, we have projected initially weakly interacting BECs onto unitarity-limited interactions and measured the resulting momentum-space dynamics. Key findings of this work are as follows: (1) The momentum distribution of the unitary gas evolves and then saturates on a

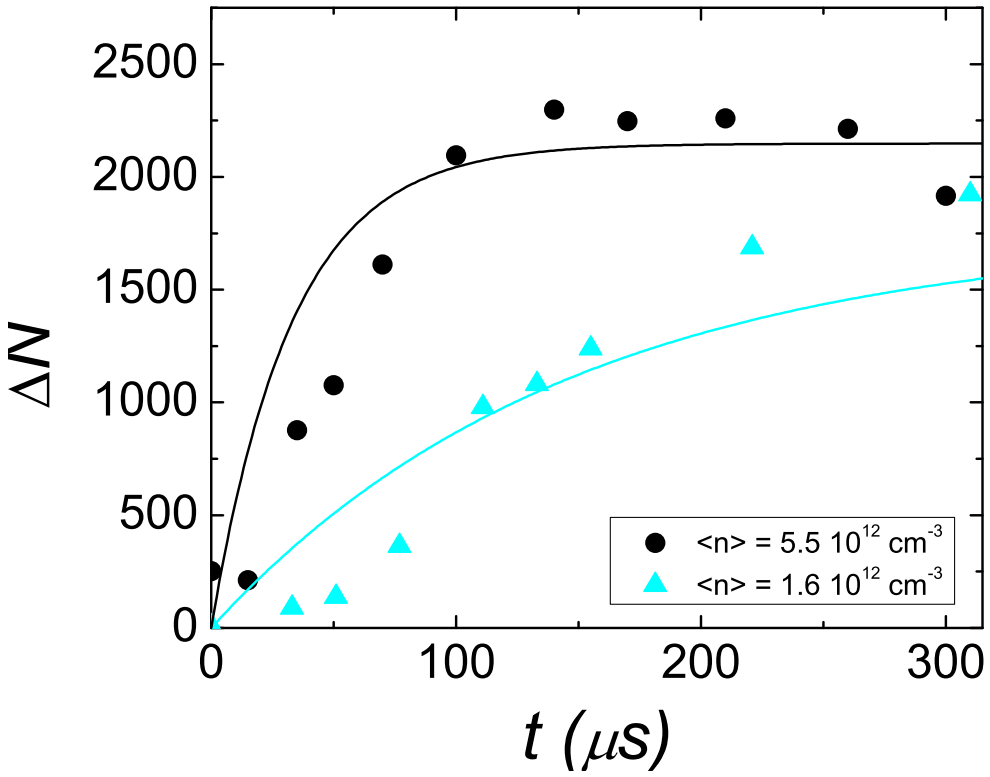

Figure 7.8: The number of atoms in two momentum ranges vs. t. Data is for κ between 0.81 and 0.89. The black circles are the fraction of atoms with $\langle n \rangle = 5.5 \times 10^{12}$ cm^{-3}. The cyan triangles are the fraction of atoms with $\langle n \rangle = 1.6 \times 10^{12}$ cm^{-3}. The lines show fits of the data to $\Delta N_0(1 - \exp^{-t/\tau})$, from which we extract the timescale for saturation, τ.

timescale that is significantly shorter that the timescale for three-body loss. (2) Both the shape of the saturated momentum distribution and the timescale for the dynamics appear to be universal. (3) Intriguingly, the saturated momentum distribution fits well to the distribution expected for an ideal degenerate Bose-Einstein gas with fugacity $z = 1$. (4) The low-momentum part of the momentum distribution indicates that the density of atoms in phase space exceeds 1, and, hence, the gas is degenerate. These findings support the conclusion that the gas reaches a locally equilibrated, metastable state and open the door for experimental investigation of a degenerate unitary Bose gas – something that was previously considered inaccessible.

This work raises some interesting questions: To what extent can the gas locally be described

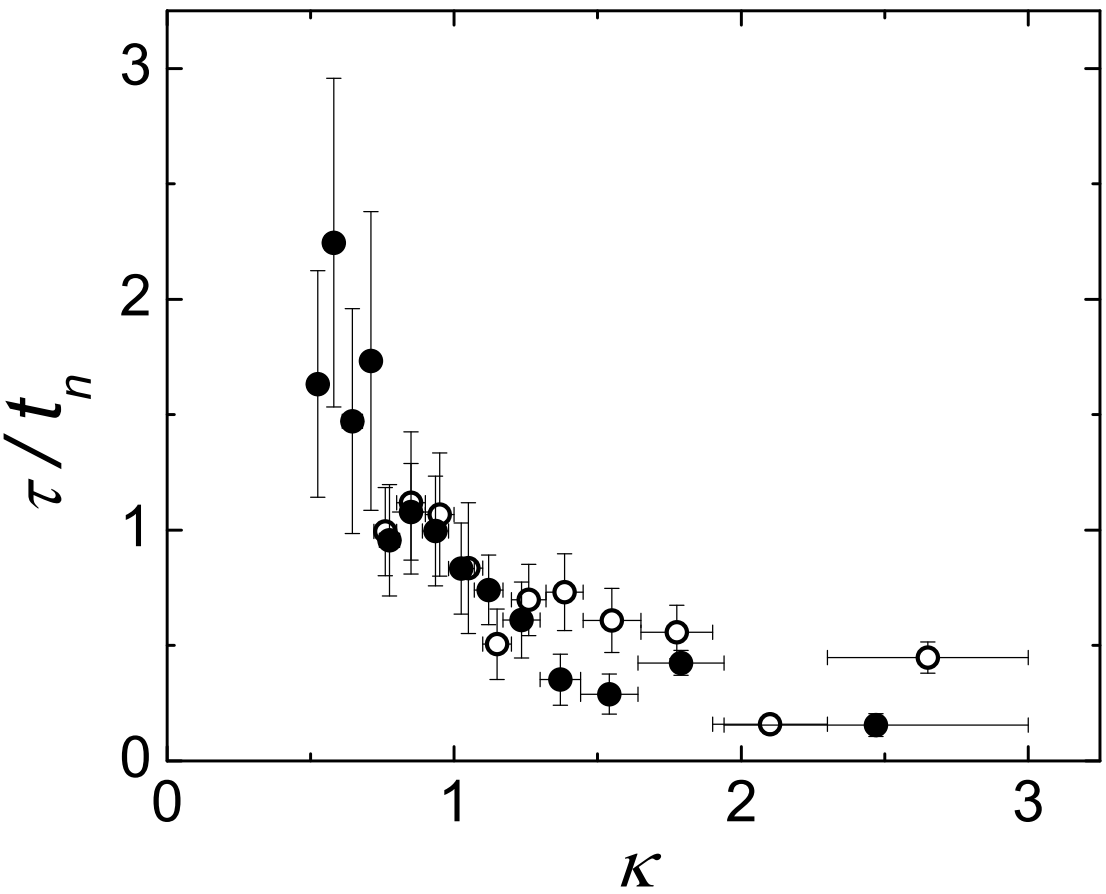

Figure 7.9: The time constant associated with the emergence of signal at high momentum plotted as a function of scaled momentum, κ. Data for $\langle n \rangle = 5.5 \times 10^{12}$ cm^{-3} are shown with solid circles, while data for $\langle n \rangle = 1.6 \times 10^{12}$ cm^{-3} are shown with open circles.

by a temperature, and is this temperature below the critical temperature for a Bose gas with unitarity-limited short-range interactions? What is this critical temperature in units of the critical temperature for an ideal Bose gas? At high momentum, what is expected for the contact, and does a high-momentum tail whose amplitude corresponds to the contact exist beyond the range of our data, or below our detection limit? Finally, what does the observed momentum dependence of the dynamics tell us about the evolution of the system at unitarity?

Chapter 8

Future Directions

8.1 Looking back

This thesis is my story of how our experimental studies of a ^{85}Rb BEC progressed from studying the mean-field regime $na^3 \approx 10^{-6}$, to measuring first-order beyond-mean-field physics ($na^3 \approx 0.002$), to the first studies of a BEC in a truly non-perturbative strongly interacting regime ($na^3 > 1$). Our studies of mean-field and beyond-mean-field effects used Bragg spectroscopy and contact spectroscopy to probe the gas. At unitarity, we tried to answer a few basic questions: What is the lifetime of the gas? Does an equilibrium exists? Is the gas degenerate? In addition to tackling these basic questions, we measured the contact to probe the gas. The results of this work have proven to be very interesting.

Our studies of a BEC at unitarity have produced a number of surprising results. Most surprising is that a degenerate gas at unitarity exists at all. Prior to these studies, an equilibrium degenerate Bose gas was thought to be impossible due to three-body loss. Instead, the gas appears to come to an equilibrium, or steady state, faster than atoms are lost. This surprising fact has inspired a number of theoretical works describing a degenerate unitarity Bose gas [120, 121, 122].

8.2 One more thing: How we project onto unitarity

Studying a gas at unitarity has opened up a number of interesting questions for our lab to pursue. The fast-B coils (described in chapter 3) allow us to control the interactions in a BEC faster and more precisely than we could before. We used the coils to project the BEC onto unitarity and

back to small a, but slower ramps are also possible. I will present "one more thing" regarding our studies of a BEC and few open experimental results that don't fit well into the previous chapters. These studies shed light onto future directions.

8.2.1 The ramp onto unitarity

As discussed in chapter 4, when we project the BEC onto unitarity the 5 μs ramp time is much shorter compared to any BEC evolution timescale. However, the 5 μs change in magnetic field is not faster than the 16 ns timescale associated with molecule binding energy at the start of the ramp. The change in interactions is diabatic at the end of the ramp since the molecule binding energy vanishes (in a two-body zero-density picture). Thus, at some point, the change in interactions changes from adiabatic to diabatic with respect to the two-body energy scale set by the Feshbach molecule binding energy. To find this transition point, we consider an adiabaticity parameter $\frac{\dot{a}}{a}/\frac{E_{mol}}{\hbar}$. This adiabaticity parameter for a 5 μs ramp in shown in figure 8.1.

For various ramp speeds, the point at which the change in interactions becomes diabatic is different. Faster ramps become diabatic at smaller scattering lengths than slower ramps. If this transition point affects how the BEC at unitarity projects onto unitarity interactions, then the saturated momentum distributions could be a function of ramp's speed. The question is: does the speed of the ramp to unitarity affect the momentum distribution? Figure 8.2 shows the saturated momentum distribution for ramps of 5 μs, 10 μs, and 20 μs. We observe little if any effect of the different ramp speeds. This suggests that the saturated momentum distributions are universal as we concluded in chapter 7. Additional studies of the effect of varying the ramp speeds to and from unitarity is an exciting future direction of the experiment.

8.2.2 Loss of atoms, but no molecules.

While exploring the ramps to and from unitarity, we observed another interesting phenomena: a loss of atoms with slower ramps away from unitarity after the momentum distribution has saturated. This is not a total surprise, as many experiments observe losses when they slowly ramp

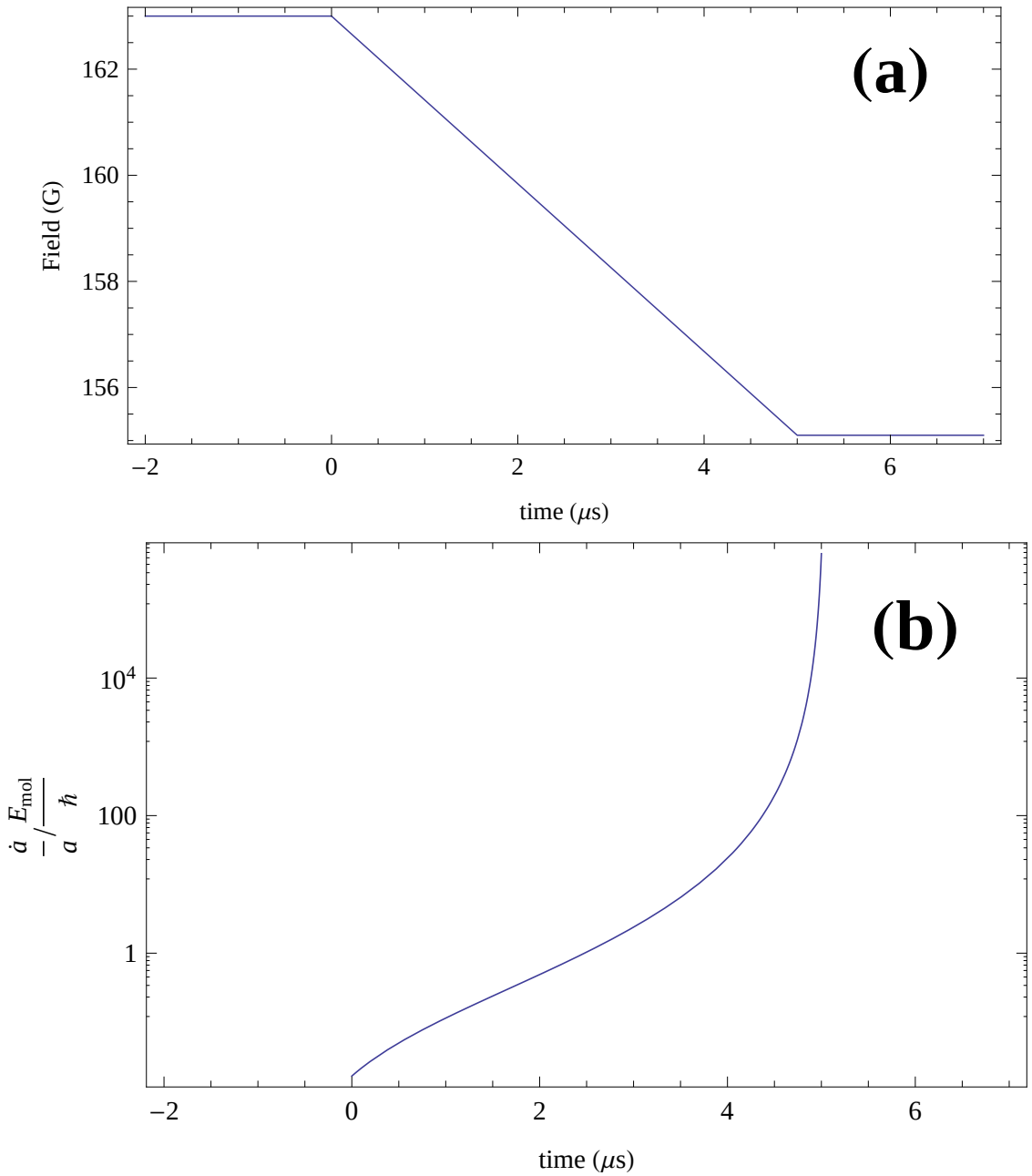

Figure 8.1: (a) The magnetic-field magnitude. The ramp is a linear ramp from 163 G to 155.04 G in 5 μs. (b) The adiabaticity parameter for ramp in (a). We plot time on the x-axis and $\frac{\dot{a}}{a}/\frac{E_{mol}}{\hbar}$ on the y-axis. When $\frac{\dot{a}}{a}/\frac{E_{mol}}{\hbar}$, the change in a is adiabatic. When $\frac{\dot{a}}{a}/\frac{E_{mol}}{\hbar} \gg 1$ the change in a is diabatic.

across the Feshbach resonance [5]. Sweeping the magnetic field slowly across the resonance tracks free atoms into Feshbach dimers, which why this is a common technique used to make dimers. Therefore, the lost atoms should appear as Feshbach molecules. We measured the population of

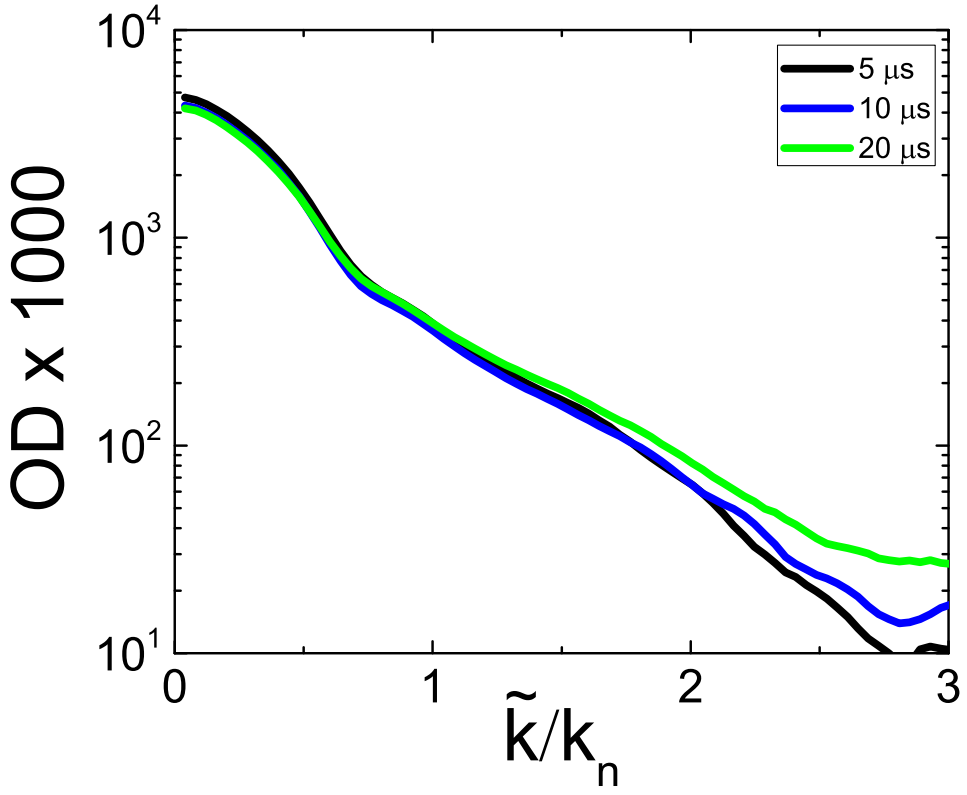

Figure 8.2: The column-integrated momentum distribution $\tilde{n}(\kappa)$ versus the transverse momentum $k/\tilde{k}$. We ramp to unitarity in either 5 μs, 10 μs, or 20 μs. The cloud is held for 100 μs and then ramped back to $\sim$ 163 G in 5 μs. The azimuthal averaged optical depth is after a time-of-flight expansion of 7 ms. We start with 6×10^4 atoms in the BEC and an average density of, $\langle n \rangle = 5.2 \times 10^{12}$ cm^{-3}.

Feshbach dimers using RF spectroscopy. Figure 8.3 shows the magnetic-field ramps to and from unitarity, which we ramp to unitarity from 163 G in 5 μs, hold for 150 μs, and ramp to 160.35 G in either 5 or 150 μs. We ramp back to 160.35 G so any Feshbach molecules that exist in our sample have 1 ms lifetime [123], much longer than time taken to image the sample. We apply an RF pulse to selectively spin flip either the atoms or Feshbach molecules into imaging state. Figure 8.4 shows an RF spectroscopy measurement for the 5 μs ramp to unitarity and a 150 μs return ramp from unitarity. The large peak in the lineshape is the signal from unbound atoms; the broader signal with a larger frequency is due to Feshbach molecules. While the number of free atoms decreases

after a slow ramp from unitarity, curiously, the signal in the molecule tail doesn't grow with this loss of atoms. One possible explanation is that the lost atoms are converted into Efimov trimers. A macroscopic population of Efimov trimers in the unitarity BEC would suggest that three-body interactions are very important at unitarity. However, further studies are needed to verify this potential explanation.

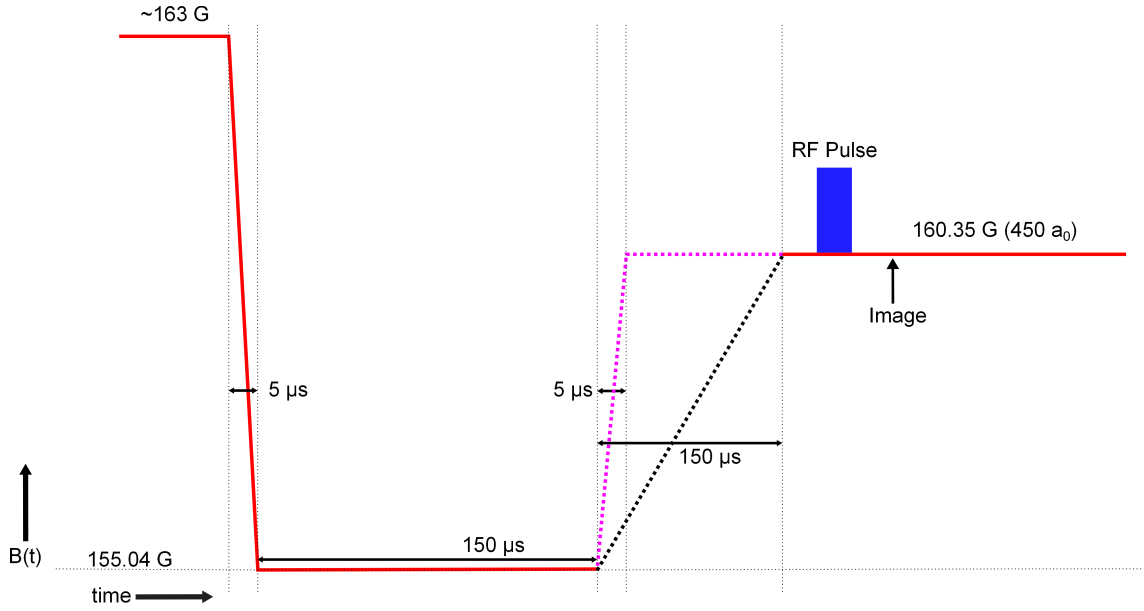

Figure 8.3: The experimental sequence of projecting a BEC onto unitarity interactions and searching for molecules. We ramp the magnetic field onto unitarity in 5 μs, hold for 150 μs, ramp to a scattering length of 450 a_0 in either 5 μs or 150 μs, and then use absorption imaging to measure the number of atoms.

8.3 Low hanging fruit

The previous ideas are two out of many different possibilities for the experiment to explore. The quasi-equilibrium of the $na^3 > 1$ degenerate Bose gas has opened a new regime to probe strongly interacting many-body physics. Further probes of the unitarity degenerate Bose gas would shed light on the system. In addition to this new regime, the fast-B system allows us to control the interactions with unprecedented speed and precision. Thus, we are excellently poised to study the time dynamics of interactions in BECs. Measuring the time-resolved contact is one possibility of

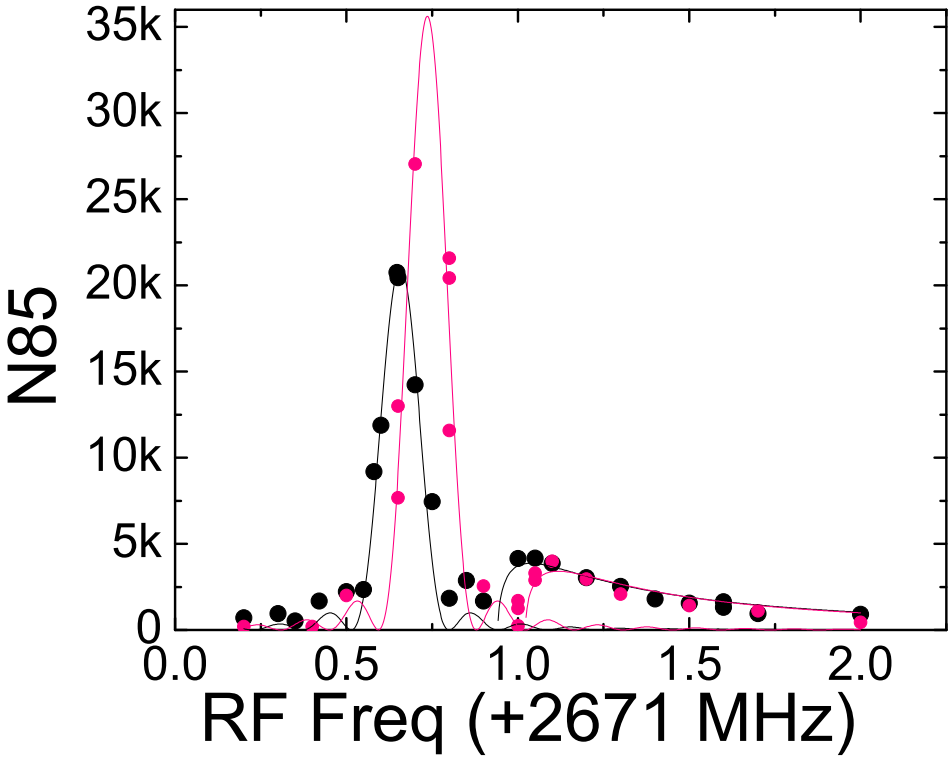

Figure 8.4: An RF spectrum of the cloud after ramps to unitarity and back. We use a 7 μs square enveloped RF pulse on the F=2 m_F=-2 to F=3 m_F=-3 Zeeman transition, which is the cycling transition. We perform absorption imaging directly after the RF pulse. The magenta line is for a 5 μs ramp back while the black line is for a 150 μs ramp back. The solid line is the expected transition probability for free atoms exposed to a pulse with a square envelope. The dotted lines are predicted response for a population of Feshbach molecules. Only the strength of the molecule response is fit since the position of the curve is fixed relative to the single atom peak by theory.

time dynamics in a BEC.

Bibliography

[1] T. Aoyama, M. Hayakawa, T. Kinoshita, and M. Nio. Tenth-order QED contribution to the electron $g-2$ and an improved value of the fine structure constant. Phys. Rev. Lett., 109:111807, 2012.

[2] M. H. Anderson, J. R. Ensher, M. R. Matthews, C. E. Wieman, and E. A. Cornell. Observation of Bose-Einstein condensation in a dilute atomic vapor. Science, 269(5221):198–201, 1995.

[3] I. Bloch, J. Dalibard, and W. Zwerger. Many-body physics with ultracold gases. Rev. Mod. Phys., 80:885–964, 2008.

[4] F. Dalfovo, S. Giorgini, L. P. Pitaevskii, and S. Stringari. Theory of Bose-Einstein condensation in trapped gases. Rev. Mod. Phys., 71(3):463, 1999.

[5] C. Chin, R. Grimm, P. Julienne, and E. Tiesinga. Feshbach resonances in ultracold gases. Rev. Mod. Phys., 82:1225–1286, 2010.

[6] S. L. Cornish, N. R. Claussen, J. L. Roberts, E. A. Cornell, and C. E. Wieman. Stable ^{85}Rb Bose-Einstein condensates with widely tunable interactions. Phys. Rev. Lett., 85(9):1795, 2000.

[7] G. F. Gribakin and V. V. Flambaum. Calculation of the scattering length in atomic collisions using the semiclassical approximation. Phys. Rev. A, 48:546–553, 1993.

[8] E. Fermi. Nuovo cim. 11, 1 (1934). Z. Phys, 88:161, 1934.

[9] J. L. Roberts, N. R. Claussen, James P. Burke, Chris H. Greene, E. A. Cornell, and C. E. Wieman. Resonant magnetic field control of elastic scattering in cold ^{85}Rb. Phys. Rev. Lett., 81:5109–5112, 1998.

[10] N. R. Claussen, S. J. J. M. F. Kokkelmans, S. T. Thompson, E. A. Donley, E. Hodby, and C. E. Wieman. Very-high-precision bound-state spectroscopy near a ^{85}Rb feshbach resonance. Phys. Rev. A, 67:060701, 2003.

[11] F. Dalfovo, S. Giorgini, L. P. Pitaevskii, and S. Stringari. Theory of Bose-Einstein condensation in trapped gases. Rev. Mod. Phys., 71:463–512, Apr 1999.

[12] E. P. Gross. Nuovo cimento 20 454 pitaevskii lp 1961. Zh. Eksp. Teor. Fiz, 40(646):1961, 1961.

[13] L. P. Pitaevskii. Vortex lines in an imperfect Bose gas. Sov. Phys. JETP, 13(2):451–454, 1961.

[14] T. D. Lee, K. Huang, and C. N. Yang. Eigenvalues and eigenfunctions of a Bose system of hard spheres and its low-temperature properties. Phys. Rev., 106:1135–1145, 1957.

[15] S. B. Papp, J. M. Pino, R. J. Wild, S. Ronen, C. E. Wieman, D. S. Jin, and E. A. Cornell. Bragg spectroscopy of a strongly interacting ^{85}Rb Bose-Einstein condensate. Phys. Rev. Lett., 101(13):135301, 2008.

[16] S. E. Pollack, D. Dries, M. Junker, Y. P. Chen, T. A. Corcovilos, and R. G. Hulet. Extreme tunability of interactions in a ^{7}Li Bose-Einstein condensate. Phys. Rev. Lett., 102:090402, 2009.

[17] N. Navon, S. Piatecki, K. Günter, B. Rem, T. C. Nguyen, F. Chevy, W. Krauth, and C. Salomon. Dynamics and thermodynamics of the low-temperature strongly interacting Bose gas. Phys. Rev. Lett., 107:135301, 2011.

[18] R. P. Smith, R. L. D. Campbell, N. Tammuz, and Zoran H. Effects of interactions on the critical temperature of a trapped Bose gas. Phys. Rev. Lett., 106:250403, 2011.

[19] R. J. Wild, P. Makotyn, J. M. Pino, E. A. Cornell, and D. S. Jin. Measurements of Tan's contact in an atomic Bose-Einstein condensate. Phys. Rev. Lett., 108:145305, 2012.

[20] W. Li and T.-L. Ho. Bose gases near unitarity. Phys. Rev. Lett., 108:195301, 2012.

[21] D. Borzov, M. S. Mashayekhi, S. Zhang, J.-L. Song, and F. Zhou. Three-dimensional Bose gas near a Feshbach resonance. Phys. Rev. A, 85:023620, 2012.

[22] B. D. Esry, Chris H. Greene, and James P. Burke. Recombination of three atoms in the ultracold limit. Phys. Rev. Lett., 83:1751–1754, 1999.

[23] P. O. Fedichev, M. W. Reynolds, and G. V. Shlyapnikov. Three-body recombination of ultracold atoms to a weakly bound s level. Phys. Rev. Lett., 77(14):2921, 1996.

[24] S. Inouye, M. R. Andrews, J. Stenger, H.-J. Miesner, D. M. Stamper-Kurn, and W. Ketterle. Observation of Feshbach resonances in a Bose-Einstein condensate. Nature, 392(6672):151–154, 1998.

[25] J. Stenger, S. Inouye, M. R. Andrews, H.-J. Miesner, D. M. Stamper-Kurn, and W. Ketterle. Strongly enhanced inelastic collisions in a Bose-Einstein condensate near Feshbach resonances. Phys. Rev. Lett., 82(12):2422, 1999.

[26] V. N. Efimov. Weakly-bound states of three resonantly-interacting particles. Sov. J. Nucl. Phys., 12:589, 1971.

[27] E. Braaten and H.-W. Hammer. Efimov physics in cold atoms. Annals of Physics, 322(1):120–163, 2007.

[28] S. B. Papp. Experiments with a two-species Bose-Einstein condensate utilizing widely tunable interparticle interactions. PhD thesis, Univerisity of Colorado - Boulder, 2007.

[29] J. M. Pino. Strongly interacting Bose-Einstein condensates: probes and techniques. PhD thesis, Univerisity of Colorado - Boulder, 2012.

[30] R. J. Wild. Contact measurements on a strongly interacting Bose gas. PhD thesis, Univerisity of Colorado - Boulder, 2012.

[31] C Regal. Experimental realization of BCS-BEC crossover physics with a Fermi gas of atoms. PhD thesis, Univerisity of Colorado - Boulder, 2006.

[32] JL Roberts. Bose-Einstein condensates with tunable atom-atom interactions: The first experiments with ^{85}Rb BECs. PhD thesis, Univerisity of Colorado - Boulder, 2001.

[33] D.M. Stamper-Kurn and J.H. Thywissen. Experimental methods of ultracold atomic physics. arXiv:1111.6196, 2011.

[34] D. E. Pritchard. Cooling neutral atoms in a magnetic trap for precision spectroscopy. Phys. Rev. Lett., 51:1336–1339, 1983.

[35] W. Ketterle, D. S. Durfee, and D. M. Stamper-Kurn. Making, probing and understanding Bose-Einstein condensates. arXiv:9904034, 1999.

[36] G. Reinaudi, T. Lahaye, Z. Wang, and D. Guéry-Odelin. Strong saturation absorption imaging of dense clouds of ultracold atoms. Opt. Lett., 32(21):3143–3145, 2007.

[37] N. R. Claussen. Dynamics of Bose-Einstein condensates near a Feshbach resonance in ^{85}Rb. PhD thesis, Univerisity of Colorado - Boulder, 2003.

[38] TD Cumby. Exploring few-body scattering resonances in a Bose-Fermi mixture: from Feshbach cimers to Efmov trimers. PhD thesis, Univerisity of Colorado - Boulder, 2012.

[39] G. F. Franklin, J. D. Powell, and A. Emami-Naeini. Feedback control of dynamic systems. Addison-Wesley Longman Publishing Co., Inc., 1997.

[40] E. J. Davison. A method for simplifying linear dynamic systems. Automatic Control, IEEE Transactions on, 11(1):93–101, 1966.

[41] F. Serwane, G. Zrn, T. Lompe, T. B. Ottenstein, A. N. Wenz, and S. Jochim. Deterministic preparation of a tunable few-fermion system. Science, 332(6027):336–338, 2011.

[42] A. N. Wenz, G. Zrn, S. Murmann, I. Brouzos, T. Lompe, and S. Jochim. From few to many: Observing the formation of a Fermi sea one atom at a time. Science, 342(6157):457–460, 2013.

[43] A. M. Kaufman, B. J. Lester, and C. A. Regal. Cooling a single atom in an optical tweezer to its quantum ground state. Phys. Rev. X, 2:041014, 2012.

[44] T. Grünzweig, A. Hilliard, M. McGovern, and M. F. Andersen. Near-deterministic preparation of a single atom in an optical microtrap. Nature Physics, 6(12):951–954, 2010.

[45] C. A. Sackett, D. Kielpinski, B. E. King, C. Langer, V. Meyer, C. J. Myatt, M. Rowe, Q. A. Turchette, W. M. Itano, D. J. Wineland, et al. Experimental entanglement of four particles. Nature, 404(6775):256–259, 2000.

[46] C. Monroe, D. M. Meekhof, B. E. King, W. M. Itano, and D. J. Wineland. Demonstration of a fundamental quantum logic gate. Phys. Rev. Lett., 75(25):4714, 1995.

[47] C. Monroe, D. M. Meekhof, B. E. King, and D. J. Wineland. A schrödinger cat superposition state of an atom. Science, 272(5265):1131–1136, 1996.

[48] M. Greiner, O. Mandel, T. Esslinger, T. W. Hänsch, and I. Bloch. Quantum phase transition from a superfluid to a Mott insulator in a gas of ultracold atoms. Nature, 415(6867):39–44, 2002.

[49] P. Kapitza. Viscosity of liquid helium below the l-point. Nature, 141(3558):74, 1938.

[50] J. F. Allen and A. D. Misener. Flow of liquid helium ii. Nature, 141(3558):75, 1938.

[51] D. M. Stamper-Kurn, A. P. Chikkatur, A. Görlitz, S. Inouye, S. Gupta, D. E. Pritchard, and W. Ketterle. Excitation of phonons in a Bose-Einstein condensate by light scattering. Phys. Rev. Lett., 83(15):2876, 1999.

[52] J. Stenger, S. Inouye, A. P. Chikkatur, D. M. Stamper-Kurn, D. E. Pritchard, and W. Ketterle. Bragg spectroscopy of a Bose-Einstein condensate. Phys. Rev. Lett., 82(23):4569, 1999.

[53] J. Steinhauer, R. Ozeri, N. Katz, and N. Davidson. Excitation spectrum of a Bose-Einstein condensate. Phys. Rev. Lett., 88:120407, 2002.

[54] S. Tan. Energetics of a strongly correlated Fermi gas. Ann. Phys., 323:2952–2970, 2008.

[55] S. Tan. Large momentum part of a strongly correlated Fermi gas. Ann. Phys., 323:2971–2986, 2008.

[56] S. Tan. Generalized virial theorem and pressure relation for a strongly correlated Fermi gas. Ann. Phys., 323:2987–2990, 2008.

[57] E. Braaten, D. Kang, and L. Platter. Universal relations for identical bosons from three-body physics. Phys. Rev. Lett., 106(15):153005–, 2011.

[58] W. Schneider, V. B. Shenoy, and M. Randeria. Theory of radio frequency spectroscopy of polarized Fermi gases. arXiv:0903.3006, 2009.

[59] A. Perali, P. Pieri, and G. C. Strinati. Competition between final-state and pairing gap effects in the radio-frequency spectra of ultracold Fermi atoms. Phys. Rev. Lett., 100:010402, 2008.

[60] E. Braaten, D. Kang, and L. Platter. Short-time operator product expansion for RF spectroscopy of a strongly interacting Fermi gas. Phys. Rev. Lett., 104:223004, 2010.

[61] R. P. Smith, S. Beattie, S. Moulder, R. L. D. Campbell, and Z. Hadzibabic. Condensation dynamics in a quantum-quenched Bose gas. Phys. Rev. Lett., 109:105301, 2012.

[62] B. S. Rem, A. T. Grier, I. Ferrier-Barbut, U. Eismann, T. Langen, N. Navon, L. Khaykovich, F. Werner, D. S. Petrov, F. Chevy, and C. Salomon. Lifetime of the Bose gas with resonant interactions. Phys. Rev. Lett., 110:163202, 2013.

[63] R. J. Fletcher, A. L. Gaunt, N. Navon, R. P. Smith, and Z. Hadzibabic. Stability of a unitary Bose gas. Phys. Rev. Lett., 111:125303, 2013.

[64] J. M. Pino, R. J. Wild, P. Makotyn, D. S. Jin, and E. A. Cornell. Photon counting for Bragg spectroscopy of quantum gases. Phys. Rev. A, 83:033615, 2011.

[65] B. M. Peden, D. Meiser, M. L. Chiofalo, and M. J. Holland. Nondestructive cavity QED probe of Bloch oscillations in a gas of ultracold atoms. Phys. Rev. A, 80(4):043803, 2009.

[66] M. Kozuma, L. Deng, E. W. Hagley, J. Wen, R. Lutwak, K. Helmersonand, S. L. Rolston, and W. D. Phillips. Coherent splitting of Bose-Einstein condensed atoms with optically induced Bragg diffraction. Phys. Rev. Lett., 82(5):871, 1999.

[67] J. Stenger, S. Inouye, A. P. Chikkatur, D. M. Stamper-Kurn, D. E. Pritchard, and W. Ketterle. Bragg spectroscopy of a Bose-Einstein condensate. Phys. Rev. Lett., 82(23):4569, 1999.

[68] J. Steinhauer, R. Ozeri, N. Katz, and N. Davidson. Excitation spectrum of a Bose-Einstein condensate. Phys. Rev. Lett., 88(12):120407, 2002.

[69] G. Veeravalli, E. Kuhnle, P. Dyke, and C. J. Vale. Bragg spectroscopy of a strongly interacting Fermi gas. Phys. Rev. Lett., 101:250403, 2008.

[70] A. Brunello, F. Dalfovo, L. Pitaevskii, S. Stringari, and F. Zambelli. Momentum transferred to a trapped Bose-Einstein condensate by stimulatedlight scattering. Phys. Rev. A, 64:063614, 2001.

[71] W Ketterle and S. Inouye. Does matter wave amplification work for fermions? Phys. Rev. Lett., 86(19):4203, 2001.

[72] B. E. A. Saleh and M. C. Teich. Fundamentals of photonics. Wiley, New York, 1991.

[73] A. Yariv. Optical electronics in modern communications. Oxford University Press, New York, 1997.

[74] I. Andonovic and D. Uttamchandani. Principles of modern optical systems. Artech House, Norwood, MA, 1989.

[75] For our photodetector, we use a Philips SA5211 Transimpedance amplifier.

[76] D. M. Stamper-Kurn, A. P. Chikkatur, A. Görlitz, S. Inouye, S. Gupta, D. E. Pritchard, and W. Ketterle. Excitation of phonons in a Bose-Einstein condensate by light scattering. Phys. Rev. Lett., 83(15):2876, 1999.

[77] E. Braaten and L. Platter. Exact relations for a strongly-interacting Fermi gas from the operator product expansion. Phys. Rev. Lett., 100:205301, 2008.

[78] E. Braaten, D. Kang, and L. Platter. Universal relations for a strongly interacting Fermi gas near a Feshbach resonance. Phys. Rev. A, 78(5):053606, 2008.

[79] S. Zhang and A. J. Leggett. Universal properties of the ultracold Fermi gas. Phys. Rev. A, 79(2):023601, 2009.

[80] R. Haussmann, M. Punk, and W. Zwerger. Spectral functions and RF response of ultracold fermionic atoms. Phys. Rev. A, 80(6):063612, 2009.

[81] D. Blume and K. M. Daily. Universal relations for a trapped four-fermion system with arbitrary s-wave scattering length. Phys. Rev. A, 80:053626, 2009.

[82] F. Werner, L. Tarruel, and Y. Castin. Number of closed-channel molecules in the BEC-BCS crossover. Eur. Phys. J. B, 68:401, 2009.

[83] E. D. Kuhnle, H. Hu, X.-J. Liu, P. Dyke, M. Mark, P. D. Drummond, P. Hannaford, and C. J. Vale. Universal behavior of pair correlations in a strongly interacting Fermi gas. Phys. Rev. Lett., 105:070402, 2010.

[84] J. T. Stewart, J. P. Gaebler, T. E. Drake, and D. S. Jin. Verification of universal relations in a strongly interacting Fermi gas. Phys. Rev. Lett., 104(23):235301, 2010.

[85] R. Combescot, F. Alzetto, and X. Leyronas. Particle distribution tail and related energy formula. Phys. Rev. A, 79(5):053640, 2009.

[86] A. M. J. Schakel. Tan relations in dilute Bose gasses. arXiv:1007.3452.

[87] F. Werner and Y. Castin. Exact relations for quantum-mechanical few-body and many-body problems with short-range interactions in two and three dimensions. arXiv:1001.0774, 2010.

[88] T. Kraemer, M. Mark, P. Waldburger, J. G. Danzl, C. Chin, B. Engeser, A. D. Lange, K. Pilch, A. Jaakkola, H.-C. Ngerl, and R. Grimm. Evidence for Efimov quantum states in an ultracold gas of caesium atoms. Nature, 440(7082):315–318, 2006.

[89] S. Knoop, F. Ferlaino, M. Mark, M. Berninger, H. Schobel, H.-C. Nagerl, and R. Grimm. Observation of an Efimov-like trimer resonance in ultracold atom-dimer scattering. Nat. Phys., 5(3):227–230, 2009.

[90] M. Zaccanti, B. Deissler, C. D/'Errico, M. Fattori, M. Jona-Lasinio, S. Muller, G. Roati, M. Inguscio, and G. Modugno. Observation of an Efimov spectrum in an atomic system. Nat. Phys., 5(8):586–591, 2009.

[91] N. Gross, Z. Shotan, S. Kokkelmans, and L. Khaykovich. Observation of universality in ultracold ^{7}Li three-body recombination. Phys. Rev. Lett., 103:163202, 2009.

[92] Y. Castin and F. Werner. Single-particle momentum distribution of an Efimov trimer. Phys. Rev. A, 83:063614, 2011.

[93] Simultaneous with this ramp, we quickly shift the vertical position of the harmonic trap to minimize the magnetic-field variation across the cloud by overlapping the center of the magnetic-field curvature with the vertical position of the cloud (this was previously not the case because of gravitational sag). In this configuration, non-uniformity of the magnetic field contributes a 3-5 kHz spread in the single-particle RF resonance frequency.

[94] J. L. Bohn. (private communication).

[95] M. Greiner, C. A. Regal, C. Ticknor, J. L. Bohn, and D. S. Jin. Detection of spatial correlations in an ultracold gas of fermions. Phys. Rev. Lett., 92:150405, 2004.

[96] E. Braaten and H. W. Hammer. Universality in few-body systems with large scattering length. Phys. Rep., 428(5-6):259–390, 2006.

[97] E. Braaten. private communication.

[98] G. F. Gribakin and V. V. Flambaum. Calculation of the scattering length in atomic collisions using the semiclassical approximation. Phys. Rev. A, 48(1):546, 1993.

[99] R. J. Wild. If instead we express a_- in terms of the van der Waals length $R_{\rm vdW} = \frac{1}{2}\left(\frac{2\mu C_6}{\hbar^2}\right)^{1/4}$ [5], which for ^{85}Rb equals 82.1 a_0, then we find a value of -9.24(7).

[100] M. Berninger, A. Zenesini, B. Huang, W. Harm, H.-C. Nägerl, F. Ferlaino, R. Grimm, P. S. Julienne, and J. M. Hutson. Universality of the three-body parameter for Efimov states in ultracold cesium. Phys. Rev. Lett., 107:120401, 2011.

[101] D. H. Smith, E. Braaten, D. Kang, and L. Platter. Two-body and three-body contacts for identical bosons near unitarity. arXiv:1309.6922, 2013.

[102] P. Makotyn, C. E. Klauss, D. L. Goldberger, E. A. Cornell, and D. S. Jin. Universal dynamics of a degenerate unitary Bose gas. arXiv:1308.3696, 2013.

[103] K. M. O'Hara, S. L. Hemmer, M. E. Gehm, S. R. Granade, and J. E. Thomas. Observation of a strongly interacting degenerate Fermi gas of atoms. Science, 298(5601):2179–2182, 2002.

[104] M. Bartenstein, A. Altmeyer, S. Riedl, S. Jochim, C. Chin, J. Hecker Denschlag, and R. Grimm. Crossover from a molecular Bose-Einstein condensate to a degenerate Fermi gas. Phys. Rev. Lett., 92:120401, 2004.

[105] C. A. Regal, M. Greiner, and D. S. Jin. Observation of resonance condensation of fermionic atom pairs. Phys. Rev. Lett., 92:040403, 2004.

[106] M. W. Zwierlein, J. R. Abo-Shaeer, A. Schirotzek, C. H. Schunck, and W. Ketterle. Vortices and superfluidity in a strongly interacting Fermi gas. Nature, 435(7045):1047–1051, 2005.

[107] G. B. Partridge, W. Li, R. I. Kamar, Y.-A. Liao, and R. G. Hulet. Pairing and phase separation in a polarized Fermi gas. Science, 311(5760):503–505, 2006.

[108] J. T. Stewart, J. P. Gaebler, C. A. Regal, and D. S. Jin. Potential energy of a ^{40}K Fermi gas in the BCS-BEC crossover. Phys. Rev. Lett., 97:220406, 2006.

[109] S. Giorgini, L. P. Pitaevskii, and S. Stringari. Theory of ultracold atomic Fermi gases. Rev. Mod. Phys., 80:1215–1274, 2008.

[110] S. Cowell, H. Heiselberg, I. E. Mazets, J. Morales, V. R. Pandharipande, and C. J. Pethick. Cold Bose gases with large scattering lengths. Phys. Rev. Lett., 88:210403, 2002.

[111] Tin-Lun Ho. Universal thermodynamics of degenerate quantum gases in the unitarity limit. Phys. Rev. Lett., 92:090402, 2004.

[112] Y.-L. Lee and Y.-W. Lee. Universality and stability for a dilute Bose gas with a Feshbach resonance. Phys. Rev. A, 81:063613, 2010.

[113] J. M. Diederix, T. C. F. van Heijst, and H. T. C. Stoof. Ground state of a resonantly interacting Bose gas. Phys. Rev. A, 84:033618, 2011.

[114] S.-J. Jiang, W.-M. Liu, G. W. Semenoff, and F. Zhou. Universal Bose gases near resonance: A rigorous solution. arXiv:1307.4263, 2013.

[115] S. Piatecki and W. Krauth. Efimov-driven phase transitions of the unitary Bose gas. arXiv:1307.4671, 2013.

[116] N. R. Claussen, E. A. Donley, S. T. Thompson, and C. E. Wieman. Microscopic dynamics in a strongly interacting Bose-Einstein condensate. Phys. Rev. Lett., 89:010401, 2002.

[117] A. Polkovnikov, K. Sengupta, A. Silva, and M. Vengalattore. *Colloquium* : Nonequilibrium dynamics of closed interacting quantum systems. Rev. Mod. Phys., 83:863–883, 2011.

[118] C. Sanner, E. J. Su, W. Huang, A. Keshet, J. Gillen, and W. Ketterle. Correlations and pair formation in a repulsively interacting Fermi gas. Phys. Rev. Lett., 108:240404, 2012.

[119] A. Härter, A. Krükow, M. Deiß, B. Drews, E. Tiemann, and J. H. Denschlag. Population distribution of product states following three-body recombination in an ultracold atomic gas. Nature Physics, 2013.

[120] A. G. Sykes, J. P. Corson, J. P. D'Incao, A. P. Koller, C. H. Greene, A. M. Rey, K. R. A. Hazzard, and J. L. Bohn. Quenching to unitarity: Quantum dynamics in a 3D Bose gas. arXiv:1309.0828, 2013.

[121] X. Yin and L. Radzihovsky. Quench dynamics of a strongly interacting resonant Bose gas. arXiv:1308.6376, 2013.

[122] D. H. Smith, E. Braaten, D. Kang, and L. Platter. Two-body and three-body contacts for identical bosons near unitarity. arXiv:1309.6922, 2013.

[123] S. T. Thompson, E. Hodby, and C. E. Wieman. Spontaneous dissociation of ^{85}Rb Feshbach molecules. Phys. Rev. Lett., 94:020401, 2005.

Appendix A

DIY guide to measuring the contact

A.1 Steps to measure the contact

During the experiment we measure the number of atoms after an RF pulse. However, the contact is defined as

$$\lim_{\omega\to\infty}\Gamma(\omega) = \Omega^2\frac{\sqrt{\hbar^{1/2}}}{4\pi\sqrt{m}\omega^{3/2}}C_2 + \Omega^2\frac{G_{RF}(\omega)\hbar}{2m\omega^2}C_3 \tag{A.1}$$

To calculate the contact from the number of atoms we measure using a specific RF power, detuning ω, and pulse duration. From equation A.1 it's clear to calculate the C_2 and C_3 we need $\Gamma(\omega)/\Omega^2$. We measure the contact in a number of steps, shown below.

Step 1) - Find the center frequency

We take an RF lineshape to find the center transition frequency, which corresponds to a detuning $\omega = 0$. Additionally, we check that the lineshape is narrow in frequency space so it doesn't contaminate the contact signal, where specifically for our experiment the lineshapes would have a gaussian width less than 10 kHz.

Step 2) - Take data on the peak

We lower the RF power and measure the number on the peak of the lineshape. The data points on the peak of the lineshape, where $\omega = 0$, is a measure of the Rabi frequency. We historically used a truncated $\pm 4\sigma$ (in electric field) with a $\tau_{peak} = 5$ μs long Gaussian pulse, which gives a Fourier

limited 22.5 kHz wide gaussian lineshape. The RF pulse should outcouple 1-2 % of the total number in the gas, which we denote as N_{peak}, since we observe non-linearities if we transfer more atoms.

Step 3) - Take data on the tail

We then measure the number of atoms outcoupled on the tail of the lineshape. The data points on the tail of the lineshape, detuned by a frequency ω, is a measure of the excitation rate for the contact, Γ. We measure N_{tail} by outcoupling 1-2% of the gas. Historically we used a gaussian pulse with τ_{tail} is 100 μs and 40 μs pulse for contact at finite na^3 and contact at unitarity, respectively.

Step 4)

Lastly, we calculate the contact using the formula below.

$$\frac{\Gamma(\omega)}{\Omega_{tail}^2} = \frac{\frac{N_{tail}}{\tau_{tail}\sqrt{\pi}}\frac{1}{10^{dB_{tail}/10}}}{\frac{N_{peak}}{N_{total}}\frac{1}{2\pi^2\tau_{peak}^2}\frac{1}{10^{dB_{tail}/10}}} \tag{A.2}$$

$$\Gamma(\omega) = \frac{N_{tail}}{\tau_{tail}\sqrt{\pi}} \tag{A.3}$$

$$\Omega_{peak}^2 = \frac{N_{peak}}{N_{total}}\frac{1}{2\pi^2\tau_{peak}^2} \tag{A.4}$$

$$\Omega_{tail}^2 = \Omega_{peak}^2 \times 10^{(dB_{tail}-dB_{peak})/10} \tag{A.5}$$

A.2 Calculate the contact

To calculate the contact we start with two formulas given by Braaten[57]

$$\lim_{\omega\to\infty}\Gamma(\omega) = \Omega^2\left[\frac{1}{4\pi}\sqrt{\frac{\hbar}{m}}\frac{1}{\omega^{3/2}}\frac{\alpha(a)}{\beta(\omega)}C_2 + \frac{G_{RF}(\omega)\hbar}{2m\omega^2}C_3\right] \tag{A.6}$$

$$\int_{-\infty}^{\infty}\Gamma(\omega)d\omega = \pi\Omega^2 N \tag{A.7}$$

We calculate C_2 and C_3 from $\Gamma(\omega)/\Omega^2$

Note that the number of outcoupled atoms for a square pulse is

$$N_{out} = \Gamma(\omega) \times \Delta t \tag{A.8}$$

When we use a gaussian pulses the outcoupled number of atoms is

$$N_{out} = \int_{-\infty}^{\infty} e^{\frac{-t^2}{\tau^2}} \Gamma(\omega) \tag{A.9}$$

$$= \tau\sqrt{\pi}\Gamma(\omega) \tag{A.10}$$

Then the number on the tail is then

$$N_{tail} = \Gamma(\omega)\tau_{tail}\sqrt{\pi} \tag{A.11}$$

Now, to calculate the contact all need is Ω_{tail}^2 is. We use the sum rule

$$\int_{-\infty}^{\infty} \Gamma(\omega) d\omega = \pi\Omega^2 N_{total} \tag{A.12}$$

Since we're Fourier limited we know the functional form of $\Gamma(\omega)$, which is

$$\Gamma(\omega) = \Gamma_0 e^{-} \frac{-\omega^2}{2\sigma_\omega^2} \tag{A.13}$$

$$\sigma_\omega = \frac{2\pi}{2\sqrt{2}\pi\tau_{tail}} \tag{A.14}$$

and like before

$$\Gamma_0 = \frac{N_{peak}}{\tau\sqrt{pi}} \tag{A.15}$$

when we take the integral of equation A.12 we find

$$\frac{N_{peak}}{\tau\sqrt{\pi}}\sqrt{2\pi}\sigma_\omega = \pi N_{total}\Omega_{peak}^2 \tag{A.16}$$

Then, the Rabi frequency is

$$\Omega_{peak}^2 = \frac{N_{tail}}{N_{total}} \frac{1}{2\pi^2\tau_{peak}^2} \tag{A.17}$$

No we have all the pieces to calculate Γ/Ω^2 and can calculate the contact.